



Universiteit  
Leiden  
The Netherlands

## **BASS. XXX. Distribution functions of DR2 Eddington ratios, black hole masses, and X-ray luminosities**

Ananna, T.T.; Weigel, A.K.; Trakhtenbrot, B.; Koss, M.J.; Urry, C.M.; Ricci, C.; ... ; Schawinski, K.

### **Citation**

Ananna, T. T., Weigel, A. K., Trakhtenbrot, B., Koss, M. J., Urry, C. M., Ricci, C., ... Schawinski, K. (2022). BASS. XXX. Distribution functions of DR2 Eddington ratios, black hole masses, and X-ray luminosities. *The Astrophysical Journal Supplement Series*, 261(1). doi:10.3847/1538-4365/ac5b64

Version: Publisher's Version  
License: [Creative Commons CC BY 4.0 license](https://creativecommons.org/licenses/by/4.0/)  
Downloaded from: <https://hdl.handle.net/1887/3515329>

**Note:** To cite this publication please use the final published version (if applicable).



# BASS. XXX. Distribution Functions of DR2 Eddington Ratios, Black Hole Masses, and X-Ray Luminosities

Tonima Tasnim Ananna<sup>1</sup> , Anna K. Weigel<sup>2</sup> , Benny Trakhtenbrot<sup>3</sup> , Michael J. Koss<sup>4,5</sup> , C. Megan Urry<sup>6</sup> ,  
Claudio Ricci<sup>7,8</sup> , Ryan C. Hickox<sup>1</sup> , Ezequiel Treister<sup>9</sup> , Franz E. Bauer<sup>10,11,5</sup> , Yoshihiro Ueda<sup>12</sup> ,  
Richard Mushotzky<sup>13</sup> , Federica Ricci<sup>14,15</sup> , Kyuseok Oh<sup>12,16,26</sup> , Julian E. Mejía-Restrepo<sup>17</sup> , Jakob Den Brok<sup>18</sup> ,  
Daniel Stern<sup>19</sup> , Meredith C. Powell<sup>20</sup> , Turgay Caglar<sup>21</sup> , Kohei Ichikawa<sup>22</sup> , O. Ivy Wong<sup>23,24</sup> , Fiona A. Harrison<sup>25</sup> , and  
Kevin Schawinski<sup>2</sup>

<sup>1</sup> Department of Physics and Astronomy, Dartmouth College, 6127 Wilder Laboratory, Hanover, NH 03755, USA; [Tonima.Ananna@dartmouth.edu](mailto:Tonima.Ananna@dartmouth.edu)

<sup>2</sup> Modulus AG, Technoparkstrasse 1, CH-8005 Zurich, Switzerland

<sup>3</sup> School of Physics and Astronomy, Tel Aviv University, Tel Aviv 69978, Israel

<sup>4</sup> Eureka Scientific, 2452 Delmer Street, Suite 100, Oakland, CA 94602-3017, USA

<sup>5</sup> Space Science Institute, 4750 Walnut Street, Suite 205, Boulder, CO 80301, USA

<sup>6</sup> Department of Physics and Yale Center for Astronomy & Astrophysics, Yale University, PO Box 201820, New Haven, CT 06520, USA

<sup>7</sup> Núcleo de Astronomía de la Facultad de Ingeniería, Universidad Diego Portales, Av. Ejército Libertador 441, Santiago 22, Chile

<sup>8</sup> Kavli Institute for Astronomy and Astrophysics, Peking University, Beijing 100871, People's Republic of China

<sup>9</sup> Instituto de Astrofísica, Facultad de Física, Pontificia Universidad Católica de Chile, Casilla 306, Santiago 22, Chile

<sup>10</sup> Instituto de Astrofísica and Centro de Astroingeniería, Facultad de Física, Pontificia Universidad Católica de Chile, Casilla 306, Santiago 22, Chile

<sup>11</sup> Millennium Institute of Astrophysics, Nuncio Monseñor Sótero Sanz 100, Of 104, Providencia, Santiago, Chile

<sup>12</sup> Department of Astronomy, Kyoto University, Kitashirakawa-Oiwake-cho, Sakyo-ku, Kyoto 606-8502, Japan

<sup>13</sup> Department of Astronomy, University of Maryland, College Park, MD 20742, USA

<sup>14</sup> Dipartimento di Fisica e Astronomia, Università di Bologna, via Piero Gobetti 93/2, I-40129 Bologna, Italy

<sup>15</sup> INAF—Osservatorio di Astrofisica e Scienza dello Spazio di Bologna, Via Gobetti, 93/3, I-40129 Bologna, Italy

<sup>16</sup> Korea Astronomy & Space Science Institute, 776, Daedeokdae-ro, Yuseong-gu, Daejeon 34055, Republic of Korea

<sup>17</sup> European Southern Observatory, Casilla 19001, Santiago 19, Chile

<sup>18</sup> Argelander-Institut für Astronomie, Universität Bonn, Auf dem Hügel 71, D-53121 Bonn, Germany

<sup>19</sup> Jet Propulsion Laboratory, California Institute of Technology, 4800 Oak Grove Drive, MS 169-224, Pasadena, CA 91109, USA

<sup>20</sup> Kavli Institute of Particle Astrophysics and Cosmology, Stanford University, 452 Lomita Mall, Stanford, CA 94305, USA

<sup>21</sup> Leiden Observatory, PO Box 9513, 2300 RA, Leiden, The Netherlands

<sup>22</sup> Frontier Research Institute for Interdisciplinary Sciences, Tohoku University, Sendai 980-8578, Japan

<sup>23</sup> CSIRO Astronomy & Space Science, PO Box 1130, Bentley, WA 6102, Australia

<sup>24</sup> ICRAR-M468, University of Western Australia, Crawley, WA 6009, Australia

<sup>25</sup> Cahill Center for Astronomy and Astrophysics, California Institute of Technology, Pasadena, CA 91125, USA

Received 2021 July 4; revised 2022 January 20; accepted 2022 February 5; published 2022 July 15

## Abstract

We determine the low-redshift X-ray luminosity function, active black hole mass function (BHMF), and Eddington ratio distribution function (ERDF) for both unobscured (Type 1) and obscured (Type 2) active galactic nuclei (AGNs), using the unprecedented spectroscopic completeness of the BAT AGN Spectroscopic Survey (BASS) data release 2. In addition to a straightforward  $1/V_{\max}$  approach, we also compute the intrinsic distributions, accounting for sample truncation by employing a forward-modeling approach to recover the observed BHMF and ERDF. As previous BHMFs and ERDFs have been robustly determined only for samples of bright, broad-line (Type 1) AGNs and/or quasars, ours are the first directly observationally constrained BHMF and ERDF of Type 2 AGNs. We find that after accounting for all observational biases, the intrinsic ERDF of Type 2 AGNs is significantly more skewed toward lower Eddington ratios than the intrinsic ERDF of Type 1 AGNs. This result supports the radiation-regulated unification scenario, in which radiation pressure dictates the geometry of the dusty obscuring structure around an AGN. Calculating the ERDFs in two separate mass bins, we verify that the derived shape is consistent, validating the assumption that the ERDF (shape) is mass-independent. We report the local AGN duty cycle as a function of mass and Eddington ratio, by comparing the BASS active BHMF with the local mass function for all supermassive black holes. We also present the  $\log N - \log S$  of the Swift/BAT 70 month sources.

*Unified Astronomy Thesaurus concepts:* Supermassive black holes (1663); Quasars (1319); Active galactic nuclei (16); High energy astrophysics (739); Active galaxies (17); X-ray active galactic nuclei (2035); X-ray surveys (1824); Luminosity function (942); Accretion (14)

## 1. Introduction

Supermassive black holes (SMBHs) are found at the centers of nearly all massive galaxies, and are understood to coevolve with their host galaxies (see Kormendy & Ho 2013 for a review). Actively accreting SMBHs, identified by their high luminosities or rates of accretion, are known as active galactic nuclei (AGNs). The space density of an AGN as a function of

<sup>26</sup> JSPS Fellow.

luminosity—i.e., the AGN luminosity function (LF)—represents a key statistical measure for the AGN population that allows us to constrain the abundance and growth history of SMBHs (e.g., Soltan 1982).

The redshift-resolved AGN LF and space density have had major impacts on our understanding of the evolving SMBH population. For example, they are used to determine the epoch of peak SMBH growth at around  $z \sim 2$  (e.g., Barger et al. 2001; Ueda et al. 2003, 2014; Hasinger et al. 2005; Croom et al. 2009; Ananna et al. 2020b), quite similar to the peak in cosmic star formation activity (e.g., Lilly et al. 1996; Madau et al. 1998; Zheng et al. 2009; Madau & Dickinson 2014; Aird et al. 2015; Caplar et al. 2015). It is also clear that the space densities of low-luminosity AGNs peak at lower redshifts compared to higher-luminosity systems (so-called “downsizing”; see, e.g., Barger et al. 2001; Ueda et al. 2003, 2014; Miyaji et al. 2015; Brandt & Alexander 2015; Ananna et al. 2020b). At yet higher redshifts, the AGN LF can help constrain the contribution of accreting SMBHs to cosmic reionization (e.g., Willott et al. 2010a; Kashikawa et al. 2015; Giallongo et al. 2015; Ricci et al. 2017d; Parsa et al. 2018; Matsuoka et al. 2018; Ananna et al. 2020b). Indeed, when used as a key ingredient in phenomenological population models, the evolving AGN LF is used to trace the growth of SMBHs throughout cosmic history, ultimately accounting for the local population of (relic) SMBHs, and even SMBH–host relations (e.g., Soltan 1982; Marconi et al. 2004; Shankar et al. 2009; Ueda et al. 2014; Aird et al. 2015; Buchner et al. 2015; Caplar et al. 2018; Ananna et al. 2019). The AGN LF is therefore a very useful statistical tool for understanding the AGN population and its evolution (see, e.g., Brandt & Alexander 2015 for a review).

The AGN LF alone, however, cannot constrain the crucial characteristics of the underlying SMBH population. This is because the AGN (bolometric) luminosity is essentially the product of two more fundamental properties of a black hole (BH)—its mass ( $M_{\text{BH}}$ ) and relative accretion rate, the latter of which we parameterize as the dimensionless Eddington ratio ( $\lambda_{\text{E}} \equiv L_{\text{bol}}/L_{\text{Edd}}$ ), that is:

$$L_{\text{bol}} \propto M_{\text{BH}} \times (L_{\text{bol}}/L_{\text{Edd}}) = M_{\text{BH}} \times \lambda_{\text{E}}. \quad (1)$$

Therefore, only after measuring the underlying BH mass and Eddington ratio for sizable, representative AGN samples can we decisively answer questions such as when was the epoch during which the most massive BHs ( $M_{\text{BH}} \gtrsim 10^9 M_{\odot}$ ) grew most of their mass. Several studies show that such high-mass BHs accreted at maximal Eddington rates, reaching the Eddington limit at  $z \gtrsim 5$  (e.g., Willott et al. 2010b; Trakhtenbrot et al. 2011; De Rosa et al. 2014). In the local universe, on the other hand, it seems that lower-mass ( $\sim 10^6 - 10^8 M_{\odot}$ ) AGNs with lower  $\lambda_{\text{E}}$  dominate space density distributions, even among the most luminous AGNs (i.e., quasars; e.g., McLure & Dunlop 2004; Netzer & Trakhtenbrot 2007; Schulze & Wisotzki 2010; Schulze et al. 2015). To obtain a complete census of the AGN population, we thus have to consider three key distribution functions: the AGN (bolometric) LF, the active black hole mass function (BHMF),<sup>27</sup> and the Eddington ratio distribution function (ERDF), after correcting for obscuration,

uncertainties on the observationally derived key quantities ( $M_{\text{BH}}$ ,  $L_{\text{bol}}$ , and  $\lambda_{\text{E}}$ ), and selection effects. These distributions are fundamentally interlinked through the ensemble version of Equation (1); that is, the bolometric LF can be expressed as the convolution of the BHMF and the ERDF.

Compared to the AGN LF, determining the BHMF and the ERDF is much more challenging. First, it requires reliable  $M_{\text{BH}}$  and  $\lambda_{\text{E}}$  measurements for large, unbiased AGN samples. In practice, beyond the local universe, this is only possible for unobscured, broad-line AGNs, thanks to “virial” mass prescriptions calibrated against reverberation mapping experiments (e.g., Shen 2013; Peterson 2014). Furthermore, certain selection effects have to be taken into account, which go beyond the more common biases affecting the LF (i.e., the Eddington bias; Eddington 1913). For flux-limited surveys, the dominant effect is a bias against low-mass and low-Eddington ratio AGNs. To address this bias, and others, the selection function of the sample at hand has to be well understood, and both the BHMF and ERDF have to be constructed (and/or fitted) simultaneously.

With these challenges in mind, the BHMF (both active and total) and the ERDF have previously been constrained from large surveys, both indirectly and directly. First, by assuming a universal relation between total stellar mass and BH mass (see, e.g., Marconi et al. 2004; Sani et al. 2011; Kormendy & Ho 2013), the shape of the *total* BHMF can be associated with the galaxy stellar mass function and determined empirically. Since the AGN LF can be expressed as a convolution of the BHMF and the ERDF, once the shape of the BHMF is known (or assumed), then the LF can be used to constrain the ERDF indirectly (e.g., Caplar et al. 2015; Weigel et al. 2017). Other studies have used the ratio between bolometric AGN luminosity and *stellar* mass as an indirect proxy for  $\lambda_{\text{E}}$  and thus the ERDF (e.g., Georgakakis et al. 2017; Aird et al. 2018).

In contrast to such indirect approaches, the *active* BHMF and the ERDF can also be determined directly from observations of AGNs for which it is possible to get reliable SMBH mass measurements. Greene & Ho (2007, 2009) constrained a low-redshift active BHMF for broad-line AGNs drawn from the Sloan Digital Sky Survey (SDSS), focusing on relatively low-mass systems, and using the  $1/V_{\text{max}}$  method to estimate the space densities (Schmidt 1968). On the other hand, Schulze & Wisotzki (2010) determined the active BHMF and the ERDF of highly luminous low-redshift quasars, drawn from the Hamburg-ESO survey (HES). The  $1/V_{\text{max}}$  method was used to determine the BHMF of  $0.3 \lesssim z \lesssim 5$  quasars drawn from the SDSS/DR3 (Vestergaard et al. 2008) and Large Bright Quasar Survey (LBQS; Vestergaard & Osmer 2009). The BHMF of quasars of comparably high luminosities and redshifts from LBQS and SDSS was also determined by Kelly et al. (2009) and Kelly & Shen (2013), respectively, with the latter also constraining the ERDF. Nobuta et al. (2012) reported the BHMF and the ERDF of broad-line AGNs at  $z = 1.4$ , selected from the Subaru XMM-Newton Deep Survey field. Schulze et al. (2015) constrained the BHMF and the ERDF for AGNs in the  $1 < z < 2$  range, combining data from the SDSS, zCOSMOS, and VVDS optical surveys. Assuming a luminosity-dependent fraction of obscured AGNs, Schulze et al. (2015) also indirectly deduced the BHMF and the ERDF of obscured (Type 2) AGNs.

Several of these studies addressed some limitations of the  $1/V_{\text{max}}$  method, and generally showed that the BHMF can be

<sup>27</sup> Note that in this work we use BHMF to denote the mass function of the active SMBH population alone, unless stated otherwise, whereas the total BHMF is the sum of active and inactive BHMFs.

described by a (modified) Schechter-like functional form (Aller & Richstone 2002), resembling the shape of the galaxy stellar mass function. The ERDF, on the other hand, is often described using a broken power-law shape (Caplar et al. 2015; Weigel et al. 2017), sharply decreasing toward high  $\lambda_E$ , and rarely exceeding the nominal Eddington limit.

High-energy X-rays are understood to be more suited for probing large samples of obscured, narrow-line (Type 2) AGNs than the optical and UV bands, due to the penetrating power of X-ray photons through high column densities of gas and dust. X-rays are also considered to be higher-purity tracers of AGNs than the infrared (IR) band, as X-rays arising from SMBH accretion are less contaminated by stellar and gas emission originating from the host galaxy. Surveys such as SDSS are highly complete in optical bands, but they (as well as soft X-ray surveys) are naturally biased toward unobscured AGNs [i.e.,  $\log(N_H/\text{cm}^{-2}) < 22$ ]. This, combined with the inability to measure  $M_{\text{BH}}$  and/or  $\lambda_E$  in narrow-line (mostly obscured) AGNs, means that essentially all existing literature presents BHMFs and ERDFs for only broad-line, unobscured (Type 1) AGNs. Nobuta et al. (2012) reported BHMF/ERDF for an X-ray-selected sample, but only for broad-line AGNs. Aird et al. (2018) constrained the distribution of  $\lambda_E$ , as probed indirectly by the X-ray luminosity, to *host* mass ratio, out to  $z \simeq 4$ , using a large (Chandra) X-ray-selected sample, also concluding that the AGN population tends toward higher  $\lambda_E$  with increasing redshift, but does not exceed the Eddington limit. However, that study did not correct for obscuration, as it was assumed that obscuration does not significantly affect a hard X-ray-selected (2–7 keV) sample. Probing the key distributions of the AGN population using a large sample selected in the ultra-hard X-ray regime thus offers a crucial addition to our understanding of SMBH accretion and triggering, even in the local universe.

The Swift/BAT AGN Spectroscopic Survey (BASS; originally presented in Koss et al. 2017) provides a large, highly complete sample of AGNs selected in the ultra-hard X-ray band (14–195 keV), along with reliable measurements of key properties. This includes X-ray fluxes and column densities derived from detailed X-ray spectral analysis (Ricci et al. 2017a), and—crucially—optical counterpart matching, redshift measurements, and  $M_{\text{BH}}$  and  $\lambda_E$  measurements, obtained through extensive optical spectroscopic observations and analysis. As shown in Figure 2 of Koss et al. (2016a), in terms of obscuration, BASS is the least biased of all X-ray surveys to date, and largely unaffected by obscuring column densities below  $\log(N_H/\text{cm}^{-2}) \simeq 23$ . The second data release of BASS (BASS/DR2; Koss et al. 2022a) provides an essentially complete census of luminosity, BH mass, Eddington ratio, and obscuration toward all AGNs in the 70 month catalog of the Swift/BAT all-sky survey, with over 800 unbeamed AGNs, mostly at  $z \lesssim 0.3$ . BASS/DR2 therefore allows us to determine the X-ray luminosity function (XLF), BHMF, and ERDF of low-redshift AGNs in an unprecedented way. It also presents the first sample of ultra-hard X-ray-selected AGNs large enough to allow for direct measurements of the BHMF and the ERDF for both Type 1 and Type 2 AGNs. Importantly, the BH masses for Type 1 and Type 2 AGNs are derived through different, though consistent and intercalibrated, methods: broad Balmer-line measurements and “virial” prescriptions are used for the former, while stellar velocity dispersion ( $\sigma_*$ ) measurements and the  $M_{\text{BH}} - \sigma_*$  relation is

used for the latter. Highly complete (95% mass measurement completeness at  $z < 0.3$ ), and with a well-understood selection function, BASS thus allows us to gain a new understanding of the local AGN population, while accounting for potential biases and statistical inference limitations (e.g., see Schulze & Wisotzki 2010; Kelly & Shen 2013; Schulze et al. 2015). With the intrinsic, bias-corrected XLF, BHMF, and ERDF at hand for both Type 1 and Type 2 AGNs, we can also investigate trends with column density, AGN duty cycle,  $M_{\text{BH}}$ , and  $\lambda_E$ , as well as whether the AGN BHMF is consistent with galaxy–SMBH scaling relations.

We present our work as follows: in Section 2, we describe the data and selection criteria; in Section 3, we discuss the details of our method of calculating the BHMF, the ERDF, and the XLF; in Section 4, we present the results of our analysis; and in Section 5, we discuss the physical implications of our results. Further details of our methods, such as the estimating of errors and the testing of our code with mock catalogs, are described in the Appendices. A flat  $\Lambda$ CDM cosmology with  $H_0 = 70 \text{ km s}^{-1} \text{ Mpc}^{-1}$ ,  $\Omega_M = 0.3$ , and  $\Omega_\Lambda = 0.7$  is assumed throughout the paper. All uncertainties reported in this paper are  $\pm 1\sigma$  from the best-fit values.

## 2. Sample, Data, and Basic Measurements

### 2.1. Sample Selection

#### 2.1.1. Input Catalog and Sample

We base our analysis on BASS/DR2, which is described in detail in Koss et al. (2022a). BASS/DR2 combines extensive optical spectroscopic measurements, X-ray spectral analysis, and derived quantities for essentially all 838 X-ray-detected sources that are part of the 70 month Swift/BAT catalog (Baumgartner et al. 2013; Ricci et al. 2017a). We further discuss aspects of this catalog and the BASS/DR2 parent sample that are crucial for our analysis, such as the flux limit (or rather, the flux–area curve), in subsequent sections.

For the X-ray-related properties of the vast majority of these AGNs, we rely on the detailed spectral measurements described in Ricci et al. (2017a). BASS/DR2 also includes 14 AGNs that were robustly detected as ultra-hard X-ray sources in the 70 month Swift/BAT catalog, but not identified as AGNs in the Ricci et al. (2017a) compilation. The X-ray spectra of these sources are analyzed as part of BASS/DR2, following the same procedures as in Ricci et al. (2017a). A detailed account of these newly identified AGNs, as well as a few more minor changes to counterpart matches, can be found in Koss et al. (2022b).

#### 2.1.2. Excluded Sources

First, we exclude all sources with Galactic latitudes  $|b| < 5^\circ$ , as the reliability of cross-matching BAT sources with optical counterparts, as well as the completeness of the BASS optical spectroscopy efforts, drop significantly for sources in the Galactic plane. All our survey area and/or volume coverage calculations are adjusted to reflect the exclusion of this region of the sky.

We also exclude from our analysis 105 beamed sources (i.e., blazars—BL Lacertae-like or flat-spectrum radio quasar sources). More details of these sources are provided in Koss et al. (2022a). Here, we briefly mention that this set constitutes sources identified through the `BZ_flg` in Ricci et al. (2017a),

sources identified in a dedicated BAT-Fermi analysis (Paliya et al. 2019), and a few additional sources for which extensive multiwavelength data suggests that they are most likely beamed (Paiano et al. 2020; L. Marcotulli 2022, in preparation). After making these two adjustments, 713 nonbeamed, non-Galactic-plane AGNs remains in our sample.

We further exclude several dual AGN systems. These dual ultra-hard X-ray-emitting systems are identified in the Swift/BAT 70 month catalog thanks to the *combined* emission of the dual sources, but are too faint to *individually* fall above the flux limit (see, e.g., the earlier Swift/BAT study by Koss et al. 2012). Such sources should be removed from our analysis, as it is fundamentally based on a well-defined, flux-limited sample. The details of each of these dual AGN systems are provided in Koss et al. (2022a). Of the 10 sources in dual systems in BASS/DR2, only NGC 6240S (BAT ID 841; Puccetti et al. 2016) and MCG+04-48-002 (BAT ID 1077; Koss et al. 2016b) fall above our nominal flux cut.

An additional 26 sources that are detectable due to their flux being enhanced through blending with a nearby brighter BAT source are also excluded. These unassociated faint X-ray sources are described in detail in Ricci et al. (2017a) and Koss et al. (2022a). Together, the exclusion of faint/weak associations and dual sources removes 37 objects from the sample, and leaves us with 678 AGNs.

### 2.1.3. Final, Redshift-restricted AGN Sample

After applying all the cuts mentioned so far, our base sample of nonbeamed, non-Galactic-plane AGNs includes 678 sources, and is used for (parts of) our XLF analysis. We next introduce a number of additional criteria to retain only those AGNs that lie in regions of parameter space in which the BAT and BASS selection functions are well understood, highly complete, and highly reproducible.

We first restrict our analysis to sources in the  $0.01 \leq z \leq 0.3$  range. This excludes the 53 nearest BASS/DR2 AGNs, for which redshift-based distance determinations may be affected by peculiar velocities, and/or which may be outliers in terms of their location in the  $L$ - $z$  plane. Altogether, the  $0.01 \leq z \leq 0.3$  sample contains 619 objects (after excluding six more AGNs at  $z > 0.3$ ).

We next limit our sample to have reliable measurements of  $L_{\text{bol}}$ ,  $M_{\text{BH}}$ , and  $\lambda_{\text{E}}$ , within ranges that are reasonable for persistent, radiatively efficient accretion onto SMBHs, and that can be probed within BASS/DR2 with a high degree of completeness. These basic measurements are described in Section 2.2 below, while the chosen ranges are listed in Table 1. Specifically, we include only those AGNs with BH masses in the range  $6.5 \leq \log(M_{\text{BH}}/M_{\odot}) \leq 10.5$  and with Eddington ratios in the range  $-3 \leq \log \lambda_{\text{E}} \leq 1$ .

Throughout our analysis, we further classify sources as being either broad-line (“Type 1,” hereafter) or narrow-line (“Type 2,” hereafter) AGNs, based on the presence of *any* broad Balmer lines (as described in Koss et al. 2022a, 2022b), and on how their most reliable measures of  $M_{\text{BH}}$  and  $\lambda_{\text{E}}$  were derived (see Section 2.2 below), which in turn has consequences for uncertainty and incompleteness estimations. Thus, our sample of Type 1 AGNs (366 sources)—sources that have at least one broad Balmer emission line—also includes so-called “Seyfert 1.9” AGNs, with broad  $H\alpha$  but no broad  $H\beta$ . Our Type 2 AGNs (220 sources) have only narrow Balmer emission lines. Type 1 AGNs are relatively unobscured

**Table 1**  
Overview of Sample Selection and Analysis Parameters<sup>a</sup>

Quantity/Variable	Symbol/Value
Minimum redshift considered	$z_{\text{min},s} = 0.01$
Maximum redshift considered	$z_{\text{max},s} = 0.3$
Minimum BH mass considered	$\log(M_{\text{BH},\text{min},s}/M_{\odot}) = 6.5$
Maximum BH mass considered	$\log(M_{\text{BH},\text{max},s}/M_{\odot}) = 10.5$
Minimum Eddington ratio considered	$\log \lambda_{\text{E},\text{min},s} = -3$
Maximum Eddington ratio considered	$\log \lambda_{\text{E},\text{max},s} = 1$
Luminosity bin size for $V_{\text{max}}$ method	$d \log L_X = 0.3$
BH mass bin size for $V_{\text{max}}$ method	$d \log(M_{\text{BH}}/M_{\odot}) = 0.3$
Edd. ratio bin size for $V_{\text{max}}$ method	$d \log \lambda_{\text{E}} = 0.3$
Assumed uncertainty on $\log M_{\text{BH}}$	$\sigma_{M_{\text{BH}}} = 0.3, 0.5$ dex
Assumed uncertainty on $\log \lambda_{\text{E}}$	$\sigma_{\log \lambda_{\text{E}}} = 0.3, 0.5$ dex
Galactic plane exclusion <sup>c</sup>	$ b  \geq 5^{\circ}$
Other cuts	Beamed AGNs are excluded

#### Notes.

<sup>a</sup> No explicit flux limits were imposed during our XLF/BHMF/ERDF analysis; instead, we used the full flux–area curve of the 70 month Swift/BAT survey (Baumgartner et al. 2013; see the main text).

<sup>b</sup> We also investigate the effect of an uncertainty of 0.2 dex in luminosity, due to measurement uncertainty and the X-ray bolometric correction (Equation (2)). Variable bolometric corrections are explored in Appendix E.

<sup>c</sup> Meant to guarantee a high completeness of optical counterpart identification and spectroscopic coverage.

[e.g.,  $\log(N_{\text{H}}/\text{cm}^{-2}) \leq 22$ ], whereas Type 2 AGNs tend to be more heavily obscured [ $\log(N_{\text{H}}/\text{cm}^{-2}) > 22$ ]; although, as shown in Section 3, these  $\log(N_{\text{H}}/\text{cm}^{-2})$  limits do not apply strictly (see also Oh et al. 2022).

For our BHMF and ERDF analysis, we exclude the four Seyfert 1.9 sources that have mass estimates only from broad  $H\alpha$  lines, as such mass estimates were shown to be highly uncertain for heavily obscured Seyfert 1.9s in the companion BASS/DR2 paper by Mejía-Restrepo et al. (2022). One of these four sources (ID 476) is the only AGN in our sample that has an estimated Eddington ratio formally greater than 10 ( $\log \lambda_{\text{E}} \simeq 1.4$ ). Therefore, the  $\lambda_{\text{E}}$  ratio upper limit we impose does not exclude objects that would otherwise have been included in the analysis. Similarly, there are no sources in the BASS/DR2 sample with BH masses greater than the upper limit on  $M_{\text{BH}}$ . These two upper limits are important for computational reasons, and are discussed in Section 3.4.

The Venn diagrams in Figure 1 show the number of nonbeamed BASS/DR2 AGNs that meet each of our selection criteria (in  $z$ ,  $M_{\text{BH}}$ , and/or  $\lambda_{\text{E}}$ ), as specified in Table 1, for both Type 1 and Type 2 AGNs. We also show the number of sources that fall *outside* all these criteria. Our main BHMF and ERDF analysis is done using the 586 AGNs that meet all criteria (366 Type 1 and 220 Type 2 AGNs), as shown in the central regions of the Venn diagrams.

## 2.2. Data and Basic Measurements

The present analysis is based on four basic, interlinked measurements that are available for the BASS/DR2 AGNs thanks to the extensive X-ray and optical spectroscopy that is at the heart of the BASS project: bolometric luminosities ( $L_{\text{bol}}$ ), BH masses ( $M_{\text{BH}}$ ), Eddington ratios ( $\lambda_{\text{E}}$ ), and line-of-sight hydrogen column densities ( $N_{\text{H}}$ ). The determination of these quantities from basic observables is described in detail in other

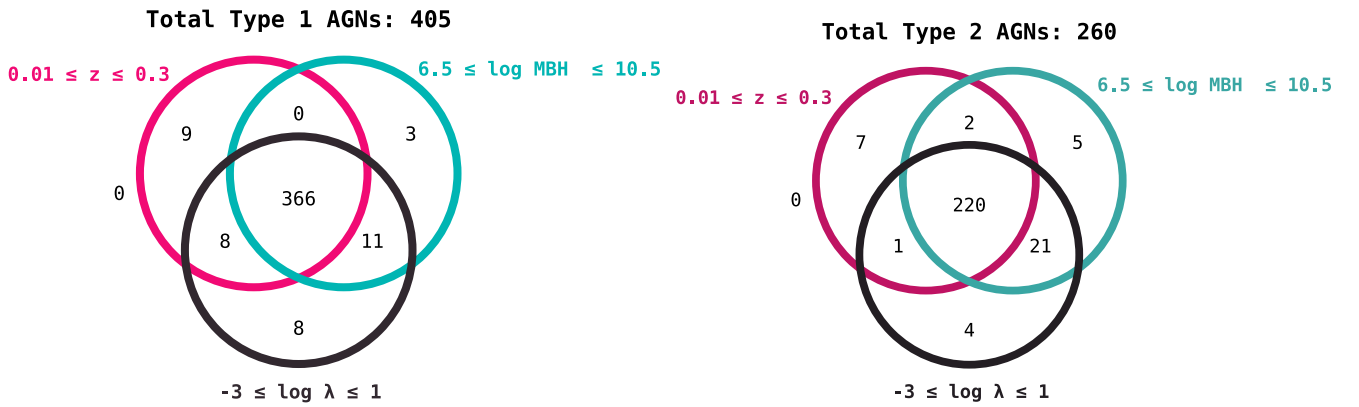


**Figure 1.** Venn diagrams of all Swift/BAT 70 month sources below  $z = 0.3$ , after removing all beamed sources and Galactic-plane sources ( $|b| < 5^\circ$ ), as well as making more subtle cuts that exclude a total of 181 sources (see the text for details). The diagrams show how the final samples of 366 Type 1 objects and 220 Type 2 objects were selected. All cuts applied to the parent sample are explicitly listed in Table 1. For each of the AGN subsamples, the red circle denotes the set of objects that fall within  $0.01 \leq z \leq 0.3$ , the green circle denotes the set that falls within  $6.5 \leq \log(M_{\text{BH}}/M_\odot) \leq 10.5$ , and the black circle denotes the set that falls within  $-3 \leq \log \lambda_E \leq 1$ . The numbers of sources in all sets and intersections of sets are also noted.

BASS publications (see below). Here, we provide only a brief summary of the aspects most relevant for the present analysis. Two key considerations for deriving these quantities are to adopt a uniform approach for all BASS AGNs, whenever possible (e.g., for  $L_{\text{bol}}$ ), and to revert to differential methodologies only when absolutely needed (e.g., for  $M_{\text{BH}}$  determination).

First, as a primary probe of AGN luminosity, we use the integrated, intrinsic luminosity between 14–195 keV ( $L_{14-195 \text{ keV}}$  or  $L_X$ , hereafter), as determined through an elaborate spectral fitting of all the available X-ray data for each BASS source, as described in detail in Ricci et al. (2017a). This X-ray spectral decomposition also yields the  $N_{\text{H}}$  measurements we use here, and we stress that the intrinsic  $L_{14-195 \text{ keV}}$  already accounts for the line-of-sight obscuration (as probed by  $N_{\text{H}}$ ). The measurement uncertainties on the X-ray luminosities we use are rather small, not exceeding  $\sim 0.05$ – $0.1$  dex for unobscured sources. Thus, whenever uncertainties on luminosities are invoked throughout our analysis, these relate to *bolometric* luminosities (unless otherwise noted), and are dominated by the systematics on the X-ray to bolometric luminosity conversion (see below).

Bolometric luminosities,  $L_{\text{bol}}$ , are then derived directly from  $L_{14-195 \text{ keV}}$ , by using a simple, universal scaling of

$$L_{\text{bol}} = \kappa_{14-195 \text{ keV}} \times L_{14-195 \text{ keV}}. \quad (2)$$

As explained in other key BASS publications (e.g., Koss et al. 2022b), this bolometric correction of  $\kappa_{14-195 \text{ keV}} = 7.4$  corresponds to a lower-energy bolometric correction of  $\kappa_{2-10 \text{ keV}} = 20$ , which is the average correction found for the BASS sample following the  $L_{2-10 \text{ keV}}$ -dependent prescription of Marconi et al. (2004), and further assumes the median X-ray power-law index found for the BASS sample,  $\Gamma = 1.8$  (e.g., Lanzuisi et al. 2013). This bolometric correction is also in agreement with Vasudevan et al. (2009). Our choice to use  $L_{14-195 \text{ keV}}$ , and not other (X-ray) luminosity probes, is motivated by (1) the need to work as closely as possible with the Swift/BAT selection functions, (2) our desire to have the most reliable determinations of  $L_{\text{bol}}$  for even the most obscured AGNs [i.e., Compton-thick sources with  $\log(N_{\text{H}}/\text{cm}^{-2}) \gtrsim 24$ ], and (3) our desire to be consistent with previous studies of the XLF of Swift/BAT-selected AGNs (e.g., Sazonov et al. 2007;

Tueller et al. 2008; Ajello et al. 2012). We acknowledge that several other, higher-order bolometric correction prescriptions have been suggested and used in the literature, including corrections that depend on luminosity,  $\lambda_E$ , and/or other AGN properties (e.g., Marconi et al. 2004; Vasudevan & Fabian 2007, 2009; Jin et al. 2012; Lusso et al. 2012; Brightman et al. 2017; Netzer 2019; Duras et al. 2020, and references therein). In the main part of the text, we prefer to use a constant bolometric correction to simplify our already complicated decomposition of the XLF, BHMF, and ERDF, and to be consistent with the rest of the BASS (DR2) analyses. However, we report how our conclusions change with a luminosity-dependent bolometric correction in Appendix E.

BH masses,  $M_{\text{BH}}$ , are determined using two different approaches for AGNs specifically with broad  $\text{H}\alpha$  line emission, and with or without broad Balmer-line emission, which allows for a certain  $M_{\text{BH}}$  estimation procedure (see immediately below). As noted above, for simplicity we refer to such sources as Type 1 and Type 2 sources, respectively, but we note that their detailed classification may be more nuanced (see Koss et al. 2022a; Mejía-Restrepo et al. 2022).

For broad-line (Type 1) AGNs, we rely on detailed spectral decomposition of the  $\text{H}\alpha$  spectral complex and “virial” BH mass prescriptions that are calibrated against reverberation mapping experiments, as described in detail in Mejía-Restrepo et al. (2022). Specifically, Mejía-Restrepo et al. followed the prescription provided by Greene & Ho (2005, Equation (6)), but adjust the virial factor to  $f = 1$ , yielding:

$$M_{\text{BH}} = 2.67 \times 10^6 \left( \frac{L[\text{bH}\alpha]}{10^{42} \text{ erg s}^{-1}} \right)^{0.55} \left( \frac{\text{FWHM}[\text{bH}\alpha]}{1000 \text{ km s}^{-1}} \right)^{2.06} M_\odot \quad (3)$$

where  $L[\text{bH}\alpha]$  and  $\text{FWHM}[\text{bH}\alpha]$  are the luminosity and width of the broad part of the  $\text{H}\alpha$  emission line, respectively. For narrow-line (Type 2) AGNs, Koss et al. (2017) and Koss et al. (2022a) rely on measurements of the stellar velocity dispersion ( $\sigma_*$ ) in the AGN host galaxies and the well-known  $M_{\text{BH}} - \sigma_*$  relation. Specifically,  $\sigma_*$  was measured from the Ca H + K, Mg I, and/or the Ca II triplet spectral complexes, as described in detail in Koss et al. (2022c). We then used the relation

determined by Kormendy & Ho (2013, Equation (3)):

$$M_{\text{BH}} = 3.09 \times 10^8 \left( \frac{\sigma_*}{200 \text{ km s}^{-1}} \right)^{4.38} M_{\odot}. \quad (4)$$

We stress that these two types of  $M_{\text{BH}}$  prescriptions are consistently calibrated. Specifically, the broad-line  $M_{\text{BH}}$  prescription in Equation (3) is derived by assuming that low-redshift, broad-line AGNs (particularly those with reverberation mapping measurements) lie on the same  $M_{\text{BH}} - \sigma_*$  relation as do narrow-line AGNs and inactive galaxies (that is, Equation (4); see, e.g., Onken et al. 2004 and Woo et al. 2013 for detailed discussions).

The uncertainties in both types of  $M_{\text{BH}}$  estimates are completely dominated by systematics and are of the order 0.3–0.5 dex (Gültekin et al. 2009; Shen 2013; Peterson 2014; Shankar et al. 2019). The lower end of this range is consistent with the scatter seen in the  $M_{\text{BH}} - \sigma_*$  (or  $M_{\text{BH}} - M_{\text{host}}$ ) relation (e.g., Sani et al. 2011; Kormendy & Ho 2013), while the upper end also includes the other key ingredients of “virial”  $M_{\text{BH}}$  determinations in broad-line AGNs (e.g., Shen 2013; Peterson 2014). The uncertainties on  $\lambda_{\text{E}}$  are naturally dominated by the systematic uncertainties on  $M_{\text{BH}}$ , and are thus also of the order 0.3–0.5 dex, although the ranges and trends seen for bolometric corrections (e.g., Marconi et al. 2004; Vasudevan & Fabian 2009) suggest that the uncertainties on  $\lambda_{\text{E}}$  may be yet higher. In comparison, our *measurement* uncertainties on  $L$  ( $\text{bH}\alpha$ ),  $\text{FWHM}(\text{bH}\alpha)$ , and  $\sigma_*$  are typically of order 10%, which would add up to  $\sim 0.1$  dex uncertainty for  $M_{\text{BH}}$  estimates in broad-line AGNs and  $< 0.2$  dex in narrow-line AGNs. Our analysis takes into account the large (systematic) uncertainties on  $M_{\text{BH}}$  determinations for all BASS AGNs, as detailed in Section 3.

Finally,  $\lambda_{\text{E}}$  is determined by combining the  $L_{\text{bol}}$  and  $M_{\text{BH}}$  estimates mentioned above, using the relation

$$\log \lambda_{\text{E}} = \log(L_{\text{bol}}/\text{erg s}^{-1}) - \log(M_{\text{BH}}/M_{\odot}) - 38.18, \quad (5)$$

which is appropriate for solar metallicity gas. As the uncertainties in both luminosity and mass must be taken into account to calculate  $\lambda_{\text{E}}$ , we present one case in our main analysis where we assume a higher error in  $\log \lambda_{\text{E}}$  to take the uncertainties in luminosity measurement/bolometric correction into account, and find that our results converge on the same solution. Larger uncertainties in  $\log \lambda_{\text{E}}$  and results due to variable bolometric correction are presented in Appendix E.

There are alternative galaxy–BH scaling relationships suggested by Bernardi et al. (2007), Shankar et al. (2017), and Shankar et al. (2020), which correct for the selection biases that may affect the samples used for calibrating these mass measurement relationships. While recalculating the masses computed using Equation (4) (i.e., velocity dispersion) would be trivial, consistently recalibrating all the other masses, calculated using various other methods, to account for these selection effects is beyond the scope of the present analysis.

### 2.3. Source Number Counts

Figure 2 shows the cumulative and differential source counts (the number density per square degree and its differential form, respectively) for the various samples relevant for the present study, specifically: (1) the input 70 month catalog ( $z \leq 0.3$ ; 672 sources); (2) our redshift-restricted AGN sample

( $0.01 \leq z \leq 0.3$ ; 619 sources); and (3) our final BASS/DR2 BHMF/ERDF sample (i.e., with  $M_{\text{BH}}$  and  $\lambda_{\text{E}}$  cuts; 586 sources). All three samples exclude the sources described in Section 2.1.2. In all cases, the uncertainties are derived assuming that the source counts follow Poisson distributions. Figure 2 also shows the best-fit curves corresponding to the various samples, which use the following functional form for the differential number counts of the three samples:

$$\frac{dN}{dS} = A \times (S/10^{-11})^{-\alpha}. \quad (6)$$

We limit our fits to the  $F_{14-195, \text{obs}} \geq 10^{-11.1} \text{ erg s}^{-1} \text{ cm}^{-2}$  flux regime, since the flux–area curve for the Swift/BAT 70 month survey (discussed in more detail in Section 3) is sparsely sampled at lower flux levels, making it difficult to accurately calculate the surface density of faint BAT sources (see the left panel of Figure 2). Our fits are derived using orthogonal distance regression (ODR), so as to properly account for uncertainties on both axes (e.g.,  $\log S$  and  $\log N$ ). One limitation of the ODR method is the inherent assumption of symmetric uncertainties (which, in our case, are averages of the upper and lower errors). For the Poisson uncertainties relevant for our analysis, this introduces only a minor change compared with the real, asymmetric uncertainties (e.g., for a bin with 25 objects, the errors are +6.07 and –4.97; see Gehrels 1986). To verify that our results are not significantly affected by the choice of fitting method (and the associated treatment of uncertainties), we have carried out an additional maximum likelihood estimator (MLE) fitting, using a Fechner distribution (see Wallis 2014 and references therein).

The best-fit slopes derived using ODR are:  $\alpha = 2.50 \pm 0.04$ ,  $2.62 \pm 0.07$ , and  $2.67 \pm 0.05$ , for the 70 month AGN, the redshift-restricted, and the final BHMF/ERDF AGN samples, respectively. The best-fit normalizations are  $\log A = 9.43 \pm 0.03$ ,  $9.44 \pm 0.03$ , and  $9.43 \pm 0.02$ , respectively. The MLE-based best-fit results are in agreement with the ORD ones, within  $\pm 1\sigma$  errors. Our best-fit curve for the full sample is consistent with the expected slope for a fully uniform Euclidean distribution ( $\alpha = 2.5$ ), and also with the results of several previous studies of ultra-hard X-ray-selected AGNs (Tueller et al. 2008; Cusumano et al. 2010; Krivonos et al. 2010; Ajello et al. 2012; Harrison et al. 2016).

For the two limited samples, the slope is not perfectly Euclidean, but that is to be expected, as objects have been removed from the total sample. We conclude that our BASS/DR2 AGN samples, which are used to determine the XLF, BHMF, and ERDF, do not show any significant biases compared to the all-sky Swift/BAT 70 month catalog and/or other samples of ultra-hard X-ray-selected AGNs. We are thus confident that we can rely on the same selection criteria, and specifically the sky coverage curves, as derived for the parent Swift/BAT 70 month catalog.

### 3. Statistical Inference Methods

The main goal of the present study is to determine and interpret the intrinsic distributions of X-ray luminosity ( $L_{14-195 \text{ keV}}$ ), SMBH mass ( $M_{\text{BH}}$ ), and the Eddington ratio ( $\lambda_{\text{E}}$ )—namely, the XLF, BHMF, and ERDF—for AGNs in the present-day universe, in the most complete way possible. In what follows, we provide a detailed description of the statistical

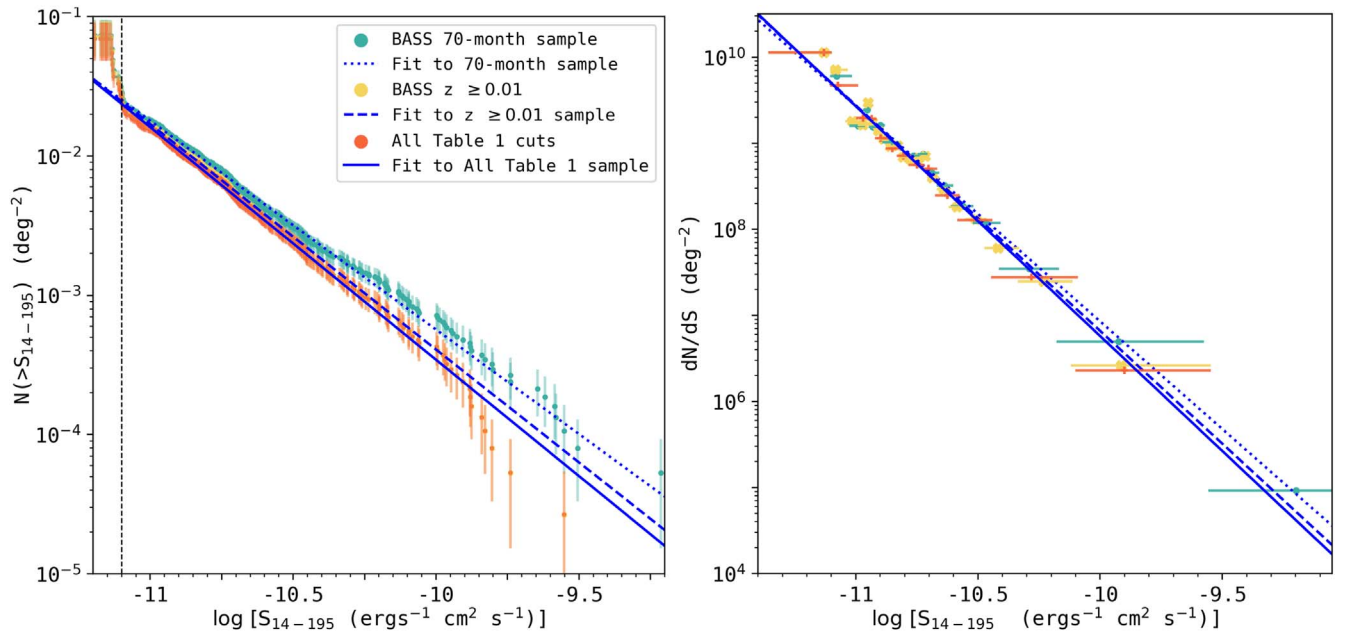


**Figure 2.** Swift/BAT cumulative number counts (left) and differential number counts (right) from the 70 month survey, with beamed sources, low-flux dual sources, sources close to the Galactic plane, and weak associations removed (672 sources, at  $z \leq 0.3$ ; turquoise data points); the same sample with an additional redshift cut applied ( $z \geq 0.01$ , 619 sources; yellow data points); and then with all Table 1 cuts applied (586 sources; red data points). The latter sample is used in our BHMF and ERDF calculations, and, as seen in this figure, it is representative of the redshift-restricted sample. We produce fits to these data using Equation (6), and report the slope and normalization of the fitted line in Section 2.3. To produce the fits, we apply a flux cut at  $F_{14-195, \text{obs}} > 10^{-11.1} \text{ erg s}^{-1} \text{ cm}^{-2}$  (shown in the left panel with the black dashed line), because the flux–area curve below that flux limit is not well constrained (Section 3 and Figure 3), artificially affecting the slope of the number counts (shown in the top left corner of the cumulative counts).

inference methods we use to derive these distributions from the basic measurements available for our sample of AGNs drawn from the all-sky Swift/BAT survey and the BASS project.

The main obstacle in deriving the statistical properties of any sample of astrophysical sources is accounting for the various factors of incompleteness and bias that are encoded in the observed sample in hand. The first and most obvious source of incompleteness for a flux-limited survey such as that of Swift/BAT AGNs is the Malmquist bias, where less-luminous sources can only be detected within a small volume at low redshift, whereas higher-luminosity ones are detected even at high  $z$ . This leads to the severe underestimation of the space densities of the former and an overestimation of the space densities of the latter.

More complex forms of bias are introduced once the incompleteness in terms of luminosity is translated into incompleteness in the distributions of related quantities, such as masses or growth rates (e.g., Marchesini et al. 2009; Pozzetti et al. 2010; Weigel et al. 2016). Specifically for the present study, the BASS AGN are selected according to their ultra-hard X-ray AGN luminosity. For the BHMF, this results in a bias against low-mass BHs that will be too faint to lie above the flux limit, unless they have exceptionally high Eddington ratios. Similarly, low-Eddington ratio AGNs will not be part of the ERDF, since they are too faint, even if they are massive. Schulze & Wisotzki (2010; hereafter, SW10) refer to this incompleteness as “sample censorship,” but we refer to it as “sample truncation,” hereafter.

Another potential source of bias may arise from the need to measure the properties for which the statistics are to be surveyed. Specifically, our estimates of BH mass depend on robustly measuring the luminosities and widths of broad emission lines (Equation (3)) or the widths of stellar absorption features (Equation (4)). This, in turn, requires well-calibrated,

medium-to-high spectral resolution observations, and also carries significant (systematic) uncertainties.

Our statistical inference methodology accounts for all these possible biases. We first constrain the XLF by using the classical  $1/V_{\text{max}}$  method (Schmidt 1968; Avni et al. 1980). We apply the same method to the  $M_{\text{BH}}$  and  $\lambda_{\text{E}}$  measurements, to gain initial guesses for the BHMF and the ERDF. We assume functional forms and fit the resulting distributions. We then use a parametric maximum likelihood approach and our initial guesses to simultaneously correct the BHMF and the ERDF for sample truncation. For the bias correction, we follow the approach used by SW10 and Schulze et al. (2015; hereafter, S15). We test our approach by creating mock catalogs, determining the corresponding distributions, and comparing those to the assumed inputs.

Throughout this work, we implicitly assume that the ERDF is  $M_{\text{BH}}$ -independent. This assumption is further justified by the analysis we present, based on splitting our sample into two  $M_{\text{BH}}$  regimes (Section 4). We also do not impose any Eddington ratio ( $\lambda_{\text{E}}$ ) dependence of the distribution of absorbing columns (i.e.,  $N_{\text{H}}$ ). Although a certain, complex, link between  $\lambda_{\text{E}}$  and  $N_{\text{H}}$  has been suggested by several studies (Ricci et al. 2017b, and references therein), our choice allows us to obtain independent evidence for such a link using our Type 1 (mostly unobscured) and Type 2 (mostly obscured) AGN samples, instead of assuming it a priori.

### 3.1. Survey-specific Considerations

We take advantage of the well-constrained flux–area curve of the Swift/BAT survey (Baumgartner et al. 2013). The flux–area curve  $\Omega_{\text{sel}}(\log F_{\text{X}})$ , shown in Figure 3, accounts for the fact that the effective area of the BAT survey is a function of the observed 14–195 keV X-ray flux. For bright, ultra-hard X-ray



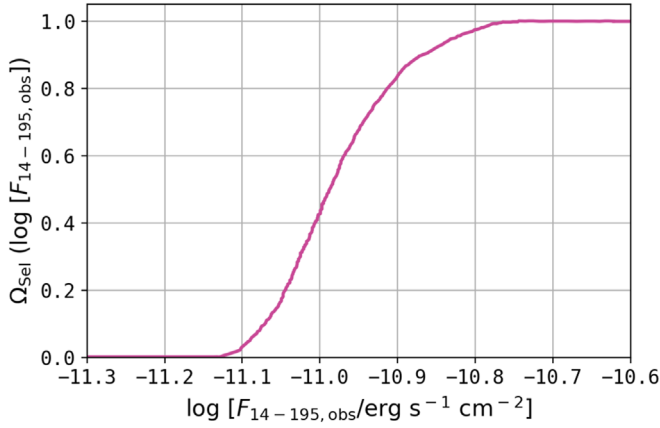


**Figure 3.** Flux–area curve of the Swift/BAT 70 month all-sky survey. To compute the XLF and gain initial guesses for the BHMF and the ERDF, we use this flux–area curve rather than a constant flux limit. For bright, ultra-hard X-ray sources,  $\log(F_{14-195, \text{obs}}/\text{erg cm}^{-2} \text{s}^{-1}) > -10.7$ , the survey is complete over the entire sky. For fainter sources, the completeness decreases as a function of the observed 14–195 keV X-ray flux. This figure converts Figure 10 of the Baumgartner et al. (2013) cumulative flux–area curve from  $\text{mCrab}$  to  $\text{erg cm}^{-2} \text{s}^{-1}$  units.

sources with  $\log(F_{14-195, \text{obs}}/\text{erg cm}^{-2} \text{s}^{-1}) > -10.7$ , the BAT survey is complete over the entire sky, i.e.,  $\Omega_{\text{sel}} = 1$ . Sources with  $\log(F_{X, \text{obs}}/\text{erg cm}^{-2} \text{s}^{-1}) < -11.3$  are completely missed by the BAT 70 month survey and catalog, and thus  $\Omega_{\text{sel}} = 0$ . Our analysis makes explicit use of the complete flux–area curve, including the intermediate values for sources with  $-11.3 \lesssim \log(F_{14-195, \text{obs}}/\text{erg cm}^{-2} \text{s}^{-1}) \lesssim -10.7$ . Note that this is the cumulative flux–area curve over the entire sky, and the sensitivity is somewhat nonuniform (as shown in Figure 1 of Baumgartner et al. 2013). Taking the slight positional differences in sensitivity into account is beyond the scope of this work.

Additionally, we account for the fact that the XLF describes the distribution of AGNs according to their *intrinsic* ultra-hard X-ray luminosity, while their detectability is a function of their *observed* (ultra-hard) X-ray flux, which depends on the amount of obscuration along the line of sight (in addition to distance, obviously). To correct the intrinsic luminosities for obscuration, and to compute the observed ultra-hard X-ray luminosities, we use the Swift/BAT attenuation curve shown in Figure 4. This observed luminosity is a sum of the transmission of the intrinsic power-law radiation and reflection from the accretion disk through the obscuring torus. This 14–195 keV attenuation curve is similar to the attenuation curve of Ricci et al. (2015), which was calculated using the torus model of Brightman & Nandra (2011) and based on the spectral models used in Ueda et al. (2014). We recalculated the attenuation curve using the BORUS02 model (Baloković et al. 2018), which updated the Brightman & Nandra (2011) torus, further assuming a photon index of  $\Gamma = 1.8$ ,  $E_{\text{cutoff}} = 200$  keV, a torus opening angle of  $60^\circ$ , and an inclination angle of  $72^\circ$  (Gilli et al. 2007; Lanzuisi et al. 2013; Ueda et al. 2014; Aird et al. 2015; Ananna et al. 2019, 2020a). We have tested how our results vary with changes in the torus opening angle and the (line-of-sight) inclination angle. Following Ricci et al. (2015), we also consider another attenuation curve for a model with an opening angle of  $35^\circ$  and an inclination angle of  $72^\circ$  (shown in Figure 4). We discuss the impacts of varying our template spectra (and other model-dependent parts of our approach) on our final results in Section 3.4.2.

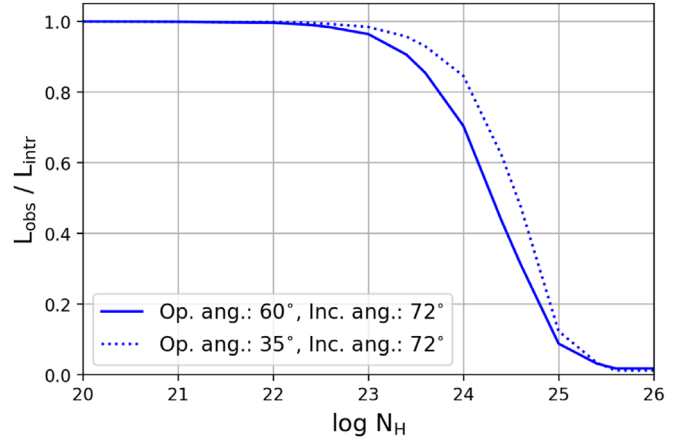


**Figure 4.** Hard X-ray (14–195 keV) attenuation curve for the BAT survey, assuming two torus opening angles:  $60^\circ$  (the solid blue line) and  $35^\circ$  (the dotted blue line). For extremely obscured sources, with  $\log(N_{\text{H}}/\text{cm}^{-2}) > 25$ , the fraction of observed luminosity relative to the intrinsic luminosity is less than 5%, making them very difficult to detect, even with the high-energy X-ray window of BAT. This is an update to the Ricci et al. (2015) attenuation curve, with a newer torus model (see the text for details).

While the BAT 14–195 keV energy range is not strongly affected by attenuation up to  $\log(N_{\text{H}}/\text{cm}^{-2}) \simeq 23.5$ , Figure 4 shows that for Compton-thick sources [ $\log(N_{\text{H}}/\text{cm}^{-2}) \gtrsim 24$ ], at least 30% and up to  $\sim 98\%$  of the intrinsic ultra-hard X-ray emission is lost [i.e., only the scattered component is detectable as  $\log(N_{\text{H}}/\text{cm}^{-2})$  approaches 26], and the luminosities of such sources may have been drastically underestimated. Our analysis makes explicit use of the complete attenuation curve, thus properly linking (limiting) observed fluxes and intrinsic luminosities, given the measured  $N_{\text{H}}$  of each AGN (Ricci et al. 2017a, Koss et al. 2022a).

We note that these links between observed fluxes, intrinsic luminosities, and surveyed angles (and volumes) affect not only the XLF, but also the BHMF and the ERDF, as the three key properties ( $L_{14-195 \text{ keV}}$ ,  $M_{\text{BH}}$ , and  $\lambda_{\text{E}}$ ) are closely related, through Equations (2) and (5).

### 3.2. The $1/N_{\text{max}}$ Method and the XLF

The  $1/V_{\text{max}}$  method (Schmidt 1968) provides a way to correct for the incompleteness (i.e., lower-luminosity/mass objects falling below the survey sensitivity at larger distances). When counting the sources within a given luminosity (or mass, etc.) bin, each source  $i$  is weighted by  $V_{\text{max}, i}$ —the maximum volume within which source  $i$  could have been detected, given the survey properties. In the case of an LF, low- and high-luminosity objects are weighted by small and large volumes, respectively. This increases and decreases their relative contribution to the respective space densities.

To measure the distribution of the AGN luminosities, BH masses, and Eddington ratios of the BASS sample, we bin in  $\log M_{\text{BH}}$ ,  $\log \lambda_{\text{E}}$ , and  $\log L_{\text{X}}$ .<sup>28</sup> We then use the  $1/V_{\text{max}}$  method to determine the corresponding space densities  $\Phi_{\text{M}}(\log M_{\text{BH}})$ ,  $\xi(\log \lambda_{\text{E}})$ , and  $\Phi_{\text{L}}(\log L_{\text{X}})$ . We compute the  $V_{\text{max}}$  values corresponding to the intrinsic, ultra-hard X-ray luminosity of each source by considering the respective observed flux and the survey completeness, as detailed below. As this  $1/V_{\text{max}}$ -based

<sup>28</sup> Note that, for simplicity, we use  $L_{\text{X}}$  to denote  $L_{14-195 \text{ keV}}$ , unless explicitly noted otherwise.

calculation does not include a robust correction either for sample truncation or for the uncertainties on the relevant key quantities, it only allows us to gain initial guesses for the BHMF and the ERDF.

For the XLF, the space density in the luminosity bin  $j$  is given by the sum over all  $N_{\text{bin}}$ -weighted objects within this bin:

$$\Phi_{L,j} d \log L_X = \sum_i^{N_{\text{bin}}} \frac{1}{V_{\text{max},i}}. \quad (7)$$

We compute  $\Phi_M(\log M_{\text{BH}})$  and  $\xi(\log \lambda_E)$  similarly, and use the bin sizes  $d \log L_X$ ,  $d \log M_{\text{BH}}$ , and  $d \log \lambda_E$ , given in Table 1.

To compute the  $V_{\text{max}}$  values for each AGN, we express the completeness of the BAT survey as a function of the intrinsic, ultra-hard X-ray luminosity, redshift, and column density:  $\Omega_{\text{sel}}(\log L_X, N_{\text{H}}, z)$ . For each object  $i$  at redshift  $z_i$  with intrinsic luminosity  $\log L_{X,i}$  and column density  $N_{\text{H},i}$ , the maximum comoving volume  $V_{\text{max},i}$  is then given by (e.g., Hogg 1999; Hiroi et al. 2012):

$$V_{\text{max},i}(\log L_{X,i}, N_{\text{H},i}, z_i) = 4\pi \times \frac{c}{H_0} \times \int_{z_{\text{min},s}}^{z_{\text{max},s}} \Omega_{\text{sel}}(\log L_{X,i}, N_{\text{H},i}, z) \frac{D_C(z)^2}{E(z)} dz. \quad (8)$$

In this expression,  $D_C(z)$  corresponds to the comoving distance to redshift  $z$ , and  $E(z)$  is given by  $\sqrt{\Omega_M(1+z)^3 + \Omega_\Lambda}$ . The integration limits  $z_{\text{min},s}$  and  $z_{\text{max},s}$  correspond to the minimum and maximum redshifts of our BASS/DR2 (refined) sample, respectively (see Table 1). Note that, unlike what is done in some studies, our calculation does not explicitly introduce a rigid flux limit, which in turn would impose a maximal redshift up to which each source could be observed,  $z_{\text{max},i}$ . Instead, this information is encoded in the flux–area curve, which ultimately provides the same outcome as  $\Omega_{\text{sel}} = 0$  when the source’s observed flux becomes too faint [i.e.,  $\log(F_{14-195,\text{obs}}/\text{erg cm}^{-2} \text{s}^{-1}) \lesssim -11.3$ ].

Note that the  $1/V_{\text{max}}$  method is very sensitive to the flux–area curve, which is nonuniform (as described in Section 3.1). As a specific example, the AGN in NGC 5283 (BAT ID 684), with  $z = 0.01036$  and  $\log(F_{14-195,\text{obs}}/\text{erg cm}^{-2} \text{s}^{-1}) = -11.14$ , falls within the criteria used to select the redshift-restricted sample (Table 1), and it is close both to the low- $z$  cut we use and to the regime where the flux–area curve drops to zero. As a result, the  $V_{\text{max}}$  within which this object can be detected above  $z > 0.1$  is very low, and this drives up the corresponding  $1/V_{\text{max}}$  value and any related contribution to the population-wide distributions under study. However, the method used to calculate the bias-corrected intrinsic BHMF and ERDF (described in Section 3.4) is *not* as dramatically affected by a single object as the direct  $1/V_{\text{max}}$  approach. We show the effect of including this single object on the  $1/V_{\text{max}}$  values in Appendix F, whereas the  $1/V_{\text{max}}$  values shown in the plots in the main body of the text exclude this object. We include this object in the bias-corrected part of our analysis.

There are several published statistical methods that address (some of) the limitations of the  $1/V_{\text{max}}$  approach, such as the Lynden-Bell–Woodrooffe–Wang estimator (Lynden-Bell 1971; Woodrooffe 1985; Choloniewski 1987; Wang 1989; Efron & Petrosian 1992), which corrects for sample truncation. Unlike the  $1/V_{\text{max}}$  method, this estimator does not depend on the assumed bin size and does not assume a constant space density over every given bin. Another flexible Bayesian parametric framework for estimating LFs while correcting for sample

truncation has been suggested by Kelly et al. (2008). However, most previous (X)LF works have used the  $1/V_{\text{max}}$  approach. Motivated by the desire for our XLF results to be directly comparable to previous studies, and by the fact that our core analysis methodology *does* ultimately correct for both sample truncation and the uncertainties on key quantities (in all three distribution functions), we chose to present the  $1/V_{\text{max}}$  results, if only as a first-order (albeit, somewhat biased) estimate of the XLF.

To estimate the random uncertainties on  $\Phi_L(\log L_X)$ ,  $\Phi_M(\log M_{\text{BH}})$ , and  $\xi(\log \lambda_E)$ , we follow the approach by Weigel et al. (2016; and see also Zhu et al. 2009; Gilbank et al. 2010). These errors are essentially Poisson errors on the number of sources in each bin, with effective weights applied based on the corresponding  $1/V_{\text{max}}$  estimates. The exact prescriptions used to calculate these uncertainties are provided in Appendix A.

### 3.3. Functional Forms for XLF, BHMF, and ERDF

Having determined the XLF and having determined an initial guess for the BHMF and the ERDF via the  $1/V_{\text{max}}$  method, we assume specific functional forms for all three distributions and fit the corresponding (differential) space densities. For the XLF, we assume a double power law of the following form:

$$\Phi_L(\log L_X) = \frac{dN}{d \log L} = \Phi_L^* \times \left[ \left( \frac{L_X}{L_X^*} \right)^{\gamma_1} + \left( \frac{L_X}{L_X^*} \right)^{\gamma_2} \right]^{-1}. \quad (9)$$

For the fitting procedure, we parameterize the second power-law slope as  $\gamma_2 = \gamma_1 + \epsilon_\gamma$ , with  $\epsilon > 0$  to avoid degeneracy between the two exponents. Given what is known about the rather universal nature of AGN LF (e.g., Shen et al. 2020, and references therein), in practice this means that our  $\gamma_1$  and  $\gamma_2$  correspond to what are often referred to as the faint- and bright-end LF slopes, respectively.

For the BHMF,  $\Phi_M(\log M_{\text{BH}}) \equiv \frac{dN}{d \log M_{\text{BH}}}$ , we use a modified Schechter function, defined as:

$$\Phi_M(\log M_{\text{BH}}) \propto \ln(10) \Phi^* \left( \frac{M_{\text{BH}}}{M_{\text{BH}}^*} \right)^{\alpha+1} \exp \left[ - \left( \frac{M_{\text{BH}}}{M_{\text{BH}}^*} \right)^\beta \right]. \quad (10)$$

This choice is motivated by the general shape of the galaxy stellar mass function (e.g., Baldry et al. 2012; Weigel et al. 2016; Davidzon et al. 2017, and references therein) and the close relations between SMBH and galaxy mass (Kormendy & Ho 2013).

For the ERDF, we use a broken power law, which we define as:

$$\xi(\log \lambda_E) = \frac{dN}{d \log \lambda_E} \propto \xi^* \times \left[ \left( \frac{\lambda_E}{\lambda_E^*} \right)^{\delta_1} + \left( \frac{\lambda_E}{\lambda_E^*} \right)^{\delta_2} \right]^{-1}. \quad (11)$$

This functional form is motivated by the fact that, qualitatively, the convolution of the BHMF with the ERDF should reproduce the LF, which directly links the bright-end slope of the XLF and the high- $\lambda_E$  slope of the ERDF (e.g., Caplar et al. 2015; Weigel et al. 2017). Similar to what was done with the XLF,

we parameterize  $\delta_2$  as  $\delta_1 + \epsilon_\lambda$ , with  $\epsilon_\lambda > 0$ , thus linking  $\delta_1$  and  $\delta_2$  with the low- and high- $\lambda_E$  ERDF slopes, respectively.

In the initial part of our analysis, we fit the  $1/V_{\max}$  measurements of the BHMF and the ERDF with these functional forms simply to obtain initial guesses for the more elaborate recovery of the intrinsic BHMF and ERDF. These same functional forms, however, are also relevant in various other parts of our analysis and interpretation.

To find the best-fitting parameters for the  $1/V_{\max}$ -based XLF, BHMF, and ERDF, we use the Markov Chain Monte Carlo (MCMC) sampler EMCEE (Foreman-Mackey et al. 2013). In Appendix B, we outline how we find the best-fitting functional form for the XLF. The BHMF and the ERDF are fit accordingly. We fit all three distributions independently. Note that this MCMC analysis only fits the functions given in Equations (9), (10), and (11) to  $1/V_{\max}$  estimates, and not directly to the observed astrophysical quantities (luminosities, masses, and/or Eddington ratios). In the next section, we describe a more elaborate method to correct for the limitations of the  $1/V_{\max}$  approach (discussed in Section 3.2), where we fit the aforementioned functions to the data directly.

### 3.4. Correcting the BHMF and the ERDF for Sample Truncation and for Uncertainties

#### 3.4.1. The Basic Principle

To correct for sample truncation—i.e., the bias against low-mass and low-Eddington ratio AGNs due to the flux-limited nature of the Swift/BAT and BASS samples—we follow the approach of SW10 and S15. The technique requires the assumption of (intrinsic) functional forms for the BHMF and the ERDF, and thus it should be considered as a parametric maximum likelihood approach.

Our aim is to constrain the intrinsic bivariate distribution function  $\Psi(\log M_{\text{BH}}, \log \lambda_E, z)$ , which also provides the BHMF and the ERDF, when integrated over  $\log \lambda_E$  and  $\log M_{\text{BH}}$ , respectively:

$$\begin{aligned}\Phi_{\text{M}}(\log M_{\text{BH}}, z) &= \int_{\log \lambda_{\text{E}, \text{min}, \text{s}}}^{\log \lambda_{\text{E}, \text{max}, \text{s}}} \Psi(\log M_{\text{BH}}, \log \lambda_E, z) d \log \lambda_E, \\ \xi(\log \lambda_E, z) &= \int_{\log M_{\text{BH}, \text{min}, \text{s}}}^{\log M_{\text{BH}, \text{max}, \text{s}}} \Psi(\log M_{\text{BH}}, \log \lambda_E, z) d \log M_{\text{BH}}.\end{aligned}\quad (12)$$

The integration limits  $\log \lambda_{\text{E}, \text{min}, \text{s}}$ ,  $\log \lambda_{\text{E}, \text{max}, \text{s}}$ ,  $\log M_{\text{BH}, \text{min}, \text{s}}$ , and  $\log M_{\text{BH}, \text{max}, \text{s}}$  correspond to the minimum and maximum Eddington ratios and BH mass values that we are considering in our analysis (see Table 1). The bivariate distribution  $\Psi(\log M_{\text{BH}}, \log \lambda_E)$  has physical units of space density, namely  $h^3 \text{Mpc}^{-3} \text{dex}^{-2}$  (i.e., per dex in  $M_{\text{BH}}$  and per dex in  $\lambda_E$ ). As the redshift range is very small, we consider only a single redshift bin and we do not model the redshift evolution of the XLF, the BHMF, and/or the ERDF; this is why our bivariate distribution function  $\Psi(\log M_{\text{BH}}, \log \lambda_E)$  does not depend directly on  $z$ . As noted above, we further assume that the ERDF is mass-independent. Under all these assumptions, the calculation of the BHMF and the ERDF from  $\Psi(\log M_{\text{BH}}, \log \lambda_E)$  (the expressions in Equation (12)) reduces

to:

$$\begin{aligned}\Phi_{\text{M}}(\log M_{\text{BH}}) &= \tilde{\Phi}(\log M_{\text{BH}}) \times \int_{\log \lambda_{\text{E}, \text{min}, \text{s}}}^{\log \lambda_{\text{E}, \text{max}, \text{s}}} \tilde{\xi}(\log \lambda_E) d \log \lambda_E \\ \xi(\log \lambda_E) &= \tilde{\xi}(\log \lambda_E) \times \int_{\log M_{\text{BH}, \text{min}, \text{s}}}^{\log M_{\text{BH}, \text{max}, \text{s}}} \tilde{\Phi}(\log M_{\text{BH}}) d \log M_{\text{BH}}.\end{aligned}\quad (13)$$

The assumed functional forms for  $\tilde{\Phi}(\log M_{\text{BH}})$  and  $\tilde{\xi}(\log \lambda_E)$  are given by the right sides of Equations (10) and (11), respectively. These two functions are proportional to the actual BHMF and ERDF. To determine  $\Phi_{\text{M}}(\log M_{\text{BH}})$  and  $\xi(\log \lambda_E)$ , we have to define the  $M_{\text{BH}}$  and  $\lambda_E$  range that is being considered and marginalize over the other distribution. As Equation (13) shows,  $\tilde{\Phi}(\log M_{\text{BH}})$  and  $\tilde{\xi}(\log \lambda_E)$  retain their assumed shapes, but their normalizations are adjusted. In Section 3.4.4, we explain how these normalizations are determined after constraining the functional forms.

To estimate  $\Psi(\log M_{\text{BH}}, \log \lambda_E)$ , we compute the log-likelihood of observing our main BASS sample, which is given by

$$\ln \mathcal{L} = \sum_i^{N_{\text{obs}}} \ln p_i(\log M_{\text{BH}, i}, \log N_{\text{H}, i}, \log \lambda_{\text{E}, i}, z_i), \quad (14)$$

where  $p_i$  is the probability of observing object  $i$  with BH mass  $\log M_{\text{BH}, i}$ , Eddington ratio  $\log \lambda_{\text{E}, i}$ , and redshift  $z_i$ . The log-likelihood thus represents the sum of such (log) probabilities, over the total number of observed sources,  $N_{\text{obs}}$ . For an assumed  $\Psi(\log M_{\text{BH}}, \log \lambda_E)$ ,  $p_i$  is given by the expected number of objects with similar properties to object  $i$ , relative to the total number of sources that are predicted to be observed;  $p_i$  thus encodes all the relevant selection effects, such as the flux limit of the survey, as we explain in detail in Section 3.4.2 immediately below. To estimate  $\Psi(\log M_{\text{BH}}, \log \lambda_E)$ , and thus the intrinsic BHMF and ERDF, we maximize the likelihood  $\mathcal{L}$ , i.e., the probability of observing our ensemble of  $N_{\text{obs}}$  sources.

#### 3.4.2. The Probability of Observing a Given Source

For a given bivariate distribution function  $\Psi$ , we express the probability of observing a specific object (index  $i$ ) in the following way:

$$\begin{aligned}p_i(\log M_{\text{BH}, i}, \log \lambda_{\text{E}, i}, \log N_{\text{H}, i}, z_i) &= \frac{N_i(\log M_{\text{BH}, i}, \log \lambda_{\text{E}, i}, \log N_{\text{H}, i}, z_i)}{N_{\text{tot}}} \\ &= \frac{1}{N_{\text{tot}}} \Psi(\log M_{\text{BH}, i}, \log \lambda_{\text{E}, i}) \\ &\quad \Omega_{\text{sel}}(\log M_{\text{BH}, i}, \log \lambda_{\text{E}, i}, \log N_{\text{H}, i}, z_i) \\ &\quad p(\log N_{\text{H}, i}) p(z_i) \frac{dV_{\text{C}}(z_i)}{dz}.\end{aligned}\quad (15)$$

Note that this expression by itself does *not* correct for measurement uncertainties. We explain the mechanism that does ultimately account for these uncertainties in Section 3.4.3 below. For simplicity, we assume that  $p(z_i)$  and  $p(\log N_{\text{H}, i})$  are independent of  $\Psi$  in this expression. The specifics of how these functions are treated for our survey and redshift range are discussed in more detail below.

Here, we describe each of the the terms used for the calculation of  $p_i$ :

1.  $\Psi$ , the intrinsic bivariate distribution function of the BH mass and Eddington ratio: for a given set of  $\log M_{\text{BH},i}$  and  $\log \lambda_{\text{E},i}$  values, the bivariate distribution function returns the space density of the objects with those properties, i.e., the *intrinsic* number of such AGNs per unit of comoving volume, per dex of BH mass and Eddington ratio.
2.  $dV_C/dz$ , the comoving volume element: by multiplying the space density of the objects with  $\log M_{\text{BH},i}$  and  $\log \lambda_{\text{E},i}$  with the comoving volume element at  $z_i$ , the space density is converted to an absolute number of sources. The comoving volume element for the entire sky is defined as (e.g., Hogg 1999):

$$\frac{dV_C(z)}{dz} = 4\pi \frac{c}{H_0} \frac{D_C(z)^2}{E(z)}, \quad (16)$$

where  $D_C$  and  $E(z)$  were defined in Section 3.2.

3.  $N_{\text{tot}}$ , the normalization: to obtain a probability, the number of sources with properties similar to object  $i$  is normalized by the total number of sources that are expected to be part of the sample after the selection effects have been taken into account.  $N_{\text{tot}}$  is given by an integral that accounts for all the quantities that affect the observability of our AGNs within the survey:

$$N_{\text{tot}} = \iiint \int \Omega_{\text{sel}}(\log M_{\text{BH}}, \log \lambda_{\text{E}}, \log N_{\text{H}}, z) \Psi(\log M_{\text{BH}}, \log \lambda_{\text{E}}) p(\log N_{\text{H}}) p(z) \frac{dV_C(z)}{dz} d \log M_{\text{BH}} d \log N_{\text{H}} d \log \lambda_{\text{E}} dz. \quad (17)$$

Here,  $d \log M_{\text{BH}}$ ,  $d \log \lambda_{\text{E}}$ , and  $dz$  are computed over the corresponding minimum and maximum values considered in the sample (see Table 1).

4.  $p(\log N_{\text{H}})$ : a bias-corrected intrinsic absorption function needs to be assumed, from which the  $\log(N_{\text{H}}/\text{cm}^{-2})$  values of the intrinsic AGN population are drawn. As explained above, while the intrinsic luminosities of AGNs are the product of their  $M_{\text{BH}}$  and  $\lambda_{\text{E}}$ , any selection or distribution function that depends on their *observed* fluxes would also have to depend on (the distribution of the) line-of-sight obscuration, which we generally associate with circumnuclear (toroidal) dusty gas. Ricci et al. (2015) derived an *intrinsic*  $\log N_{\text{H}}$  distribution specifically for Swift/BAT-detected AGNs, considering X-ray reflection from a torus. This model assumed an opening angle of  $60^\circ$  and considered two luminosity bins—above and below  $\log(L_{14-195 \text{ keV}}/\text{erg s}^{-1}) = 43.7$ . This intrinsic  $\log N_{\text{H}}$  distribution is shown in Figure 5.

To test the impacts of different models, we also calculate the results for an absorption function with a torus opening angle of  $35^\circ$  (also from Ricci et al. 2015), the results of which are reported in Section 4 and shown in Appendix F. For consistency, the attenuation curve used when testing the effect of this absorption function also assumes an opening angle of  $35^\circ$  (see Figure 4). While one may expect that our results would have changed significantly if the input absorption function and attenuation curve were substantially different, we find

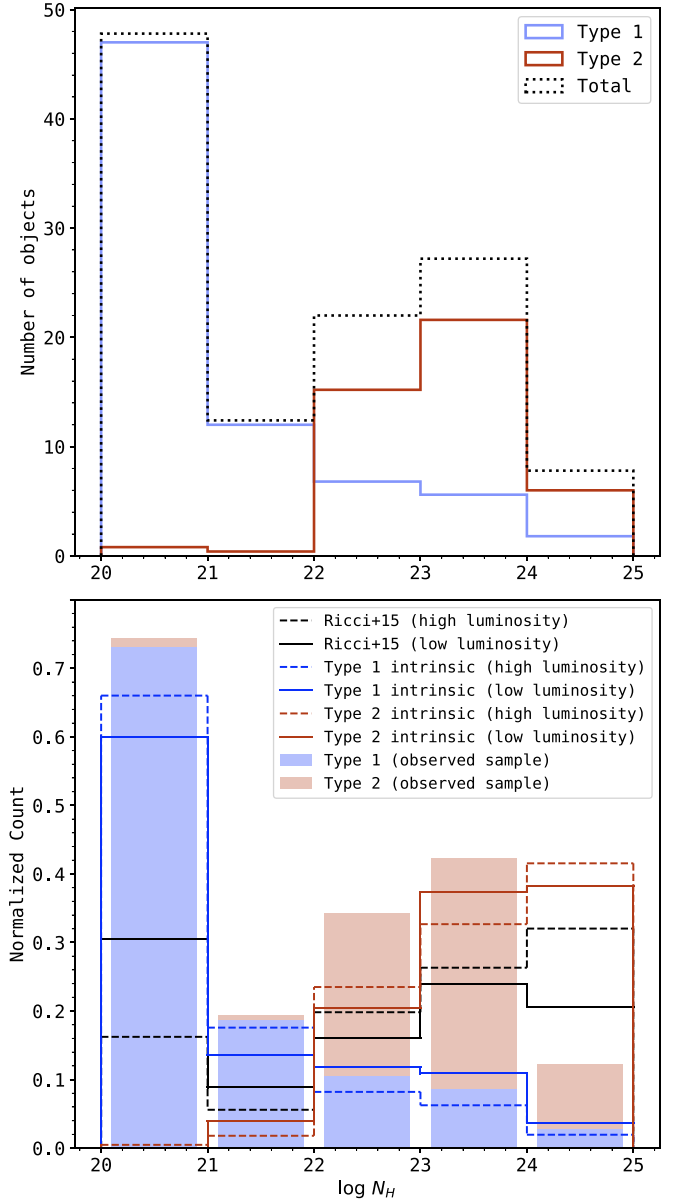


**Figure 5.** Top panel: observed histograms of absorbing column density,  $\log N_{\text{H}}$ , for Type 1 (blue lines) and Type 2 (red lines) AGNs, and the overall distribution (black dotted lines). Bottom panel: normalized distributions observed for Type 1 (blue stacked bars) and Type 2 (red stacked bars) AGNs, along with the bias-corrected column density distribution of the BASS 70 month survey sample (Ricci et al. 2015), calculated for two luminosity bins:  $\log(L_{14-195 \text{ keV}}/\text{erg s}^{-1}) \leq 43.7$  (black solid lines) and  $\log(L_{14-195 \text{ keV}}/\text{erg s}^{-1}) > 43.7$  (black dashed lines). For Type 1 AGNs (blue lines), we assume the intrinsic and observed column densities are the same, as Type 1 AGNs tend to be relatively unobscured, then we calculate the Type 2 distribution (red lines) by subtracting the Type 1 distribution from the overall distribution in each luminosity bin. We use the intrinsic distributions when calculating the BHMF and the ERDF for the sample.

that this small change in the assumed opening angle did not alter our results substantially. This indicates that our overall conclusions are robust against reasonably motivated changes to the model-dependent components.

We argue that since the intrinsic absorption function derived in Ricci et al. (2015; in particular, with  $60^\circ$ ) is calculated specifically for the BAT sample, this is the appropriate function for our purposes. We note that this

absorption function is defined over the range  $\log(N_{\text{H}}/\text{cm}^{-2}) = 20\text{--}25$  in discrete bins of 1 dex width. While calculating  $N_{\text{tot}}$  for all AGNs, we assign  $\log(N_{\text{H}}/\text{cm}^{-2})$  to each object from the underlying distribution by drawing values from this absorption function, taking the luminosity dependence into account. In this work, we choose to incorporate the luminosity-dependent absorption function as provided by Ricci et al. (2015), and do not impose any direct  $\lambda_{\text{E}}$  dependence on the absorption function. While a  $\lambda_{\text{E}}$  dependence is supported by some studies (e.g., Ricci et al. 2017b, and references therein), imposing such a dependence a priori would limit our ability to reveal the differences in the BHMF and the ERDF of obscured and unobscured sources. The distributions used in our calculations are shown in the bottom panel of Figure 5. When we compute the BHMF and the ERDF for Type 1 AGNs, we assume the intrinsic absorption function to be identical to the observed one, which is justified given the negligible effects of absorption in such sources. For Type 2 AGNs, we subtract the distribution of Type 1 AGNs from the bias-corrected overall distribution in each luminosity bin. These distributions are shown using the red dashed and solid lines (for high- and low-luminosity bins, respectively) in the bottom panel of Figure 5. Note that as the Ricci et al. (2015) absorption function is luminosity-dependent, the  $p(\log N_{\text{H}})$  used in this work is in fact  $p(\log N_{\text{H}}|L_X(M_{\text{BH}}, \lambda_{\text{E}}))$ .

5.  $p(z)$ : this is the redshift dependence term in the general expression, which in our case is considered constant (i.e., set to 1 in both the numerator and denominator of  $p_i$ ).
6.  $\Omega_{\text{sel}}$ : in Equation (15), the term  $\Omega_{\text{sel}}(\log M_{\text{BH},i}, \log \lambda_{\text{E},i}, \log N_{\text{H},i}, z_i)$  corresponds to the selection function of the survey. In its simplest form,  $\Omega_{\text{sel}}$  returns the value of the flux–area curve,  $\Omega_{\text{sel}}(\log F_X)$ , for each source (see Section 3.2). To predict the X-ray flux  $\log F_{X,i}$  for source  $i$  with BH mass  $\log M_{\text{BH},i}$ , an Eddington ratio  $\log \lambda_{\text{E},i}$ , a column density  $\log N_{\text{H},i}$ , and a redshift  $z_i$ , we perform the following sequence of calculations.

First, we compute the corresponding bolometric luminosity,  $L_{\text{bol}}$ , using Equation (5) (in Appendix E, we experiment with a variable, luminosity-dependent bolometric correction); from  $L_{\text{bol}}$ , we then calculate the intrinsic, ultra-hard X-ray luminosity over the 14–195 keV range,  $L_{14\text{--}195 \text{ keV}}$ , using Equation (2); from that we deduce the luminosity and flux as measured by BAT, taking into account the column density (using the curve shown in Figure 4) and the luminosity distance to the source (using  $z_i$ ). The calculated  $\log F_{X,i}$  is then used to obtain the selection function, based on the curve shown in Figure 3.

### 3.4.3. The Observed Bivariate Distribution Function

As presented in Equation (15),  $p_i$  is a four-dimensional normalized probability distribution function, and in order to properly account for the various selection functions in play, it needs to be convolved with the uncertainties in each of the four underlying parameters. Specifically, the selection effect–

corrected  $p_i$  is as follows:

$$\begin{aligned}
 p_{i, \text{conv}}(\log M_{\text{BH},i}, \log \lambda_{\text{E},i}, \log N_{\text{H},i}, z_i) &= \frac{N_{i, \text{conv}}}{N_{\text{tot}}} \\
 &= \frac{1}{N_{\text{tot}}} \iiint \int \Psi(\log M_{\text{BH}}, \log \lambda_{\text{E}}, \log N_{\text{H}}, z) \\
 &\quad \times \Omega_{\text{sel}}(\log M_{\text{BH}}, \log \lambda_{\text{E}}, \log N_{\text{H}}, z) \\
 &\quad \times p(\log N_{\text{H}}) p(z) \frac{dV_C(z)}{dz} \\
 &\quad \times \omega(\log M_{\text{BH},i}, \log \lambda_{\text{E},i}, \log N_{\text{H},i}, z_i | \log M_{\text{BH}}, \log \lambda_{\text{E}}, \log N_{\text{H}}, \\
 &\quad d \log M_{\text{BH}} \ d \log \lambda_{\text{E}} \ d \log N_{\text{H}} \ dz).
 \end{aligned} \tag{18}$$

Here, the denominator  $N_{\text{tot}}$  is the normalization constant of the original probability distribution  $p_i$ , and retains the value presented in Equation (17), while  $\omega$  is the four-dimensional Gaussian distribution function that reflects the uncertainties related to the  $i$ th object, for all four directly or indirectly measured quantities. That is:

$$\begin{aligned}
 &\omega(\log M_{\text{BH},i}, \log \lambda_{\text{E},i}, \log N_{\text{H},i}, z_i | \log M_{\text{BH}}, \log \lambda_{\text{E}}, \log N_{\text{H}}, z) \\
 &= \frac{1}{4\pi^2 \sigma_{\log M_{\text{BH}}} \sigma_{\log \lambda_{\text{E}}} \sigma_{\log N_{\text{H}}} \sigma_z} \\
 &\quad \times \exp\left(-\frac{(\log M_{\text{BH},i} - \log M_{\text{BH}})^2}{2\sigma_{\log M_{\text{BH}}}^2} - \frac{(\log \lambda_{\text{E},i} - \log \lambda_{\text{E}})^2}{2\sigma_{\log \lambda_{\text{E}}}^2}\right) \\
 &\quad \times \exp\left(-\frac{(\log N_{\text{H},i} - \log N_{\text{H}})^2}{2\sigma_{\log N_{\text{H}}}^2} - \frac{(z_i - z)^2}{2\sigma_z^2}\right),
 \end{aligned} \tag{19}$$

where  $\sigma_{\log M_{\text{BH}}}$ ,  $\sigma_{\log \lambda_{\text{E}}}$ ,  $\sigma_{\log N_{\text{H}}}$ , and  $\sigma_z$  correspond to the assumed uncertainties on  $\log M_{\text{BH}}$ ,  $\log \lambda_{\text{E}}$ ,  $\log N_{\text{H}}$ , and  $z$ , respectively (see Table 1). Note that—at least for  $\log M_{\text{BH}}$  and  $\log \lambda_{\text{E}}$ —these are dominated by systematic uncertainties inherent to the BH mass estimation methods we rely on.

Since we have spectroscopic redshifts for all sources in our sample, and the obscuring column densities  $\log N_{\text{H}}$  are derived from extensive spectral decomposition of multimission X-ray data (combining Swift/BAT and ancillary spectra at  $E < 10$  keV), the convolution over  $\log N_{\text{H}}$  and  $z$  (with  $\sigma_{\log N_{\text{H}}} = 0.25$  and  $\sigma_z = 0.005$ ) does not change our results, but makes the process significantly more computationally expensive. Thus, in practice, we choose to only convolve over two dimensions:

$$\begin{aligned}
 &\omega(\log M_{\text{BH},i}, \log \lambda_{\text{E},i} | \log M_{\text{BH}}, \log \lambda_{\text{E}}) \\
 &= \frac{1}{2\pi \sigma_{\log M_{\text{BH}}} \sigma_{\log \lambda_{\text{E}}}} \\
 &\quad \times \exp\left(-\frac{(\log M_{\text{BH},i} - \log M_{\text{BH}})^2}{2\sigma_{\log M_{\text{BH}}}^2} - \frac{(\log \lambda_{\text{E},i} - \log \lambda_{\text{E}})^2}{2\sigma_{\log \lambda_{\text{E}}}^2}\right).
 \end{aligned} \tag{20}$$

We note that convolving over  $z$  and/or  $\log N_{\text{H}}$  may be, in principle, essential and beneficial for the analysis of samples that have photometric redshifts and/or more uncertain column density measurements.

In our main analysis, we have assumed  $\sigma_{\log M_{\text{BH}}} = \sigma_{\log \lambda_{\text{E}}} = 0.3$  dex (see Table 1). The assumption of no uncertainties (i.e.,

$\sigma_{\log M_{\text{BH}}} = \sigma_{\log \lambda_E} = 0$ ) is used only to test and demonstrate our analysis framework in Appendix D. A higher value of  $\sigma_{\log M_{\text{BH}}} = \sigma_{\log \lambda_E} = 0.5$  dex is required for Type 2 AGNs, to take into account the rotation and aperture effects in the optical spectroscopy that is used to measure  $\sigma_*$  (see, e.g., Gültekin et al. 2009 and Shankar et al. 2019). Additionally, we report results for a scenario where  $\sigma_{\log M_{\text{BH}}} = 0.3$  dex, along with a total uncertainty of 0.2 dex in bolometric luminosity ( $\sigma_{\log L_{\text{scatt}}}$ ), which reflects both measurement and systematic uncertainties (dominated by the latter). As  $\log \lambda_E$  is calculated using two observed quantities (luminosity and mass), the uncertainty in the luminosity measurement also contributes to the total uncertainty in  $\log \lambda_E$ . Therefore, the uncertainty in  $\log \lambda_E$  is  $\sigma_{\log \lambda_E} \simeq 0.36$  (i.e., the log uncertainties in mass and luminosity added in quadrature). We note that this approach to calculating  $\sigma_{\log \lambda_E}$  is conservative, since the actual measurement errors on (X-ray) luminosities are much smaller than 0.2 dex, and since the intertwined nature of  $L$ ,  $M_{\text{BH}}$ , and  $\lambda_E$  means that any systematic errors on  $\log M_{\text{BH}}$  and  $\log \lambda_E$  would be anticorrelated, rather than independent. As shown in Section 4, the various (conservative) levels of uncertainty we assume do not significantly affect our key results, attesting to the robustness of our conclusions.

In Appendix E, we report the results of an even more complex scenario, assuming a luminosity-dependent bolometric correction (from Duras et al. 2020), and an even larger error on  $\log \lambda_E$ . Our framework has also been tested by using mock catalogs for this scenario, and the results are shown in Appendix D. In the main part of the analysis, we present the results of the simpler scenario with constant bolometric correction.

We stress again that we have *not* imposed any dependence of obscuration on luminosity,  $M_{\text{BH}}$ , or  $\lambda_E$  in the main analysis. Thus, any difference between the XLF, BHMF, and/or ERDF derived for the obscured and unobscured subsamples (Type 1 and 2 AGNs) would occur independent of our model assumptions. In Appendix E, where we present results for variable bolometric correction, some more complex assumptions are introduced. For example, Type 1 and Type 2 AGNs have different bolometric corrections. This might artificially introduce differences in the results between the two populations, therefore we keep such assumptions to a minimum in our main analysis.

#### 3.4.4. Constraining $\Psi$

To determine the intrinsic bivariate distribution function,  $\Psi(\log M_{\text{BH}}, \log \lambda_E)$ , we maximize the likelihood of observing our main input sample. Expressing the log-likelihood (Equation (14)) using Equation (15) gives:

$$\ln \mathcal{L} = \sum_i^{N_{\text{obs}}} \ln [N_{i, \text{conv}} \times (\log M_{\text{BH},i}, \log \lambda_{E,i}, \log N_{H,i}, z_i)] - \ln N_{\text{tot}}. \quad (21)$$

Similar to the fitting procedure for the  $1/V_{\text{max}}$  values, we use the MCMC PYTHON package EMCEE to maximize  $\ln \mathcal{L}$  (Foreman-Mackey et al. 2013). The number of free parameters in these fits, which is six ( $\gamma_1, \epsilon_\lambda, \lambda_E^*, \alpha, \beta$ , and  $M_{\text{BH}}^*$ ), reflects the functional forms assumed for the BHMF and the ERDF. The initial guesses are based on the MCMC fits to the  $1/V_{\text{max}}$

values, and 50 walkers are allowed to take 3000 steps (the chains usually converge within 2500 steps).

Equation (18) shows that the normalization of the intrinsic bivariate distribution function,  $\Psi^*$ , does not affect the probability of observing source  $i$ , and thus also has no impact on the log-likelihood  $\ln \mathcal{L}$ . When applying the MCMC procedure, we thus use constant normalizations for both the BHMF ( $\Phi_{\text{init}}^*$ ) and the ERDF ( $\xi_{\text{init}}^*$ ). Having determined the best-fitting parameters, we renormalize  $\Psi$  and determine  $\Psi^*$  as follows:

$$\Psi^* = a_{\text{rescale}} \times \frac{N_{\text{obs}}}{N_{\text{tot, best-fit}}(\Phi_{\text{init}}^*, \xi_{\text{init}}^*)}. \quad (22)$$

Here,  $N_{\text{obs}}$  corresponds to the total number of objects observed in our sample, while  $N_{\text{tot, best-fit}}$  is determined by using Equation (17), the best-fitting parameters for  $\Psi$ , and the initial normalizations  $\Phi_{\text{init}}^*$  and  $\xi_{\text{init}}^*$ . The parameter  $a_{\text{rescale}}$  corresponds to an additional rescaling factor that can be used to correct for only partially available data (i.e.,  $z$  and/or  $M_{\text{BH}}$  measurements). As our sample is spectroscopically complete (excluding the nonbeamed, non-Galactic sources, along with the others discussed in Section 2.1.2), we assume  $a_{\text{rescale}} = 1$  for this work.

Finally, we use Equation (13) to determine the bias-corrected intrinsic BHMF and ERDF:

$$\begin{aligned} \tilde{\Phi}_M(\log M_{\text{BH}}) &= \Psi^* \tilde{\Phi}(\log M_{\text{BH}}, \Phi_{\text{init}}^*) \\ &\int_{\log \lambda_{E, \text{min}, s}}^{\log \lambda_{E, \text{max}, s}} \tilde{\xi}(\log \lambda_E, \xi_{\text{init}}^*) d \log \lambda_E \\ \tilde{\xi}(\log \lambda_E) &= \Psi^* \tilde{\xi}(\log \lambda_E, \xi_{\text{init}}^*) \\ &\int_{\log M_{\text{BH}, \text{min}, s}}^{\log M_{\text{BH}, \text{max}, s}} \tilde{\Phi}(\log M_{\text{BH}}, \Phi_{\text{init}}^*) d \log M_{\text{BH}}. \end{aligned} \quad (23)$$

As  $\Psi^*$  has units of space density, namely  $h^3 \text{Mpc}^{-3} \text{dex}^{-2}$ , so do  $\tilde{\Phi}^*$  and  $\tilde{\xi}^*$ .

We have tested our methodology end to end to verify that we can indeed uncover the intrinsic distributions of BHMF and ERDF using this approach. To this end, we created two mock catalogs for both Type 1 and Type 2 AGNs, and tested our method using three different levels of uncertainty on the (mock)  $\log M_{\text{BH}}$  and  $\log \lambda_E$  values. These tests and mock catalogs are described in detail in Appendix D.

## 4. Results: The Intrinsic Distributions Governing the BASS Sample

In this section, we present our results for the XLF, the BHMF, and the ERDF of the BASS/DR2 sample, including the distributions corresponding to the subsets of Type 1 and Type 2 AGNs. We discuss some of the considerations made when determining the XLF, present the XLF for AGNs in different  $\log N_H$  bins (in addition to the Type 1 and Type 2 AGN XLFs), and compare to the results of previous studies of AGNs selected in the ultra-hard X-ray regime. We then determine the bias-corrected BHMF and ERDF for BASS/DR2 AGNs, and again compare our results to those of previous studies. We finally demonstrate that the XLF that we derive from our fundamental bivariate, bias-corrected  $M_{\text{BH}}$ - and  $\lambda_E$ -dependent distribution can reproduce the XLF that we measure directly from the observations.

We note that the  $1/V_{\text{max}}$ -based XLF reported in this work is a way of understanding the distribution of the *observed* data

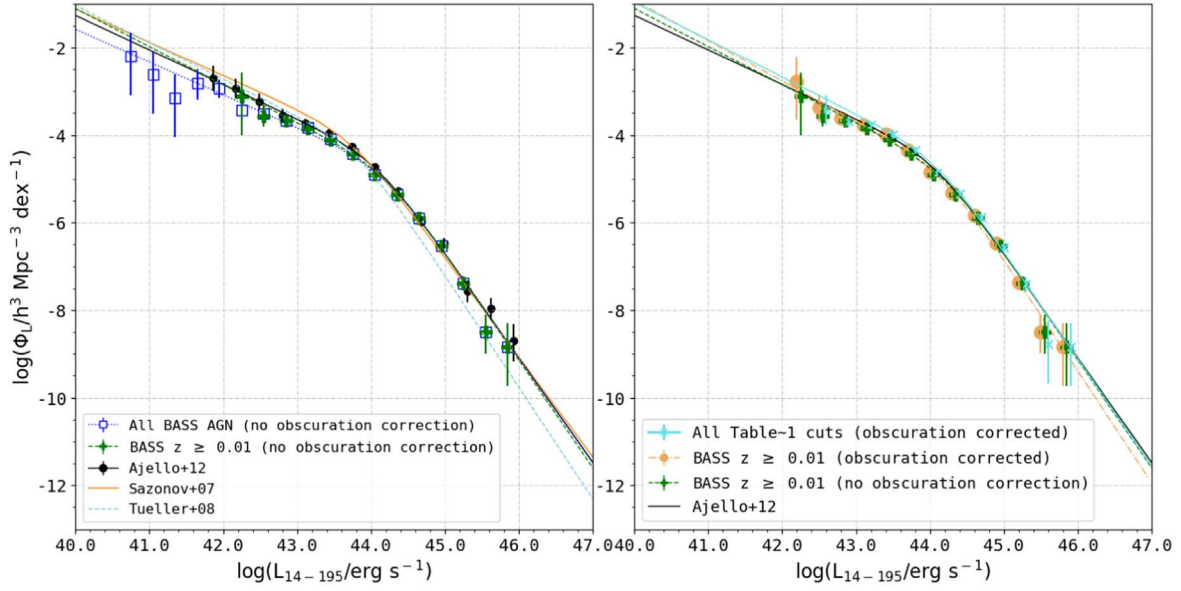


**Figure 6.** The effect of the low redshift cut and obscuration on the BASS XLF. Left panel: the BASS XLF determined without a low- $z$  cut (blue squares; 672 sources), and the corresponding fit (dotted blue line). The Green plus signs show the XLF after excluding nearby sources with  $z < 0.01$  (leaving 659 sources in the sample), with the green dashed line showing the fit to these  $\Phi_L$  values. For comparison, we show the XLFs by Sazonov et al. (2007), Tueller et al. (2008), and Ajello et al. (2012). Right panel: the obscuring column density  $N_{\text{H}}$  has a small but systematic effect on the XLF. The Green plus signs and the green dashed line show the XLF computed by not taking obscuration into account when computing the  $1/V_{\text{max}}$  values, while the orange filled circles (shifted left by 0.05 dex for clarity) illustrate the obscuration-corrected  $\Phi_L$  values. The  $N_{\text{H}}$  correction consistently increases the space densities in most luminosity bins. The turquoise crosses (shifted right by 0.05 dex for clarity) and the turquoise solid line show the XLF after applying all the cuts in Table 1 (586 sources).

**Table 2**  
Best-fitting XLF Parameters<sup>a</sup>

Selection	$\log(L_X^*/\text{erg s}^{-1})$	$\log(\Phi_L^*/h^3 \text{ Mpc}^{-3})$	$\gamma_1$	$\epsilon_\gamma$
BASS AGNs at $z \leq 0.3$ (672; no obscuration correction)	$44.17_{-0.18}^{+0.13}$	$-4.71_{-0.19}^{+0.25}$	$0.75_{-0.11}^{+0.11}$	$1.64_{-0.10}^{+0.11}$
$0.01 \leq z \leq 0.3$ (619; no obscuration correction)	$44.23_{-0.24}^{+0.18}$	$-4.79_{-0.30}^{+0.34}$	$0.87_{-0.21}^{+0.19}$	$1.59_{-0.13}^{+0.14}$
$0.01 \leq z \leq 0.3$ (619; obscuration-corrected)	$44.24_{-0.31}^{+0.24}$	$-4.78_{-0.39}^{+0.35}$	$0.92_{-0.25}^{+0.21}$	$1.63_{-0.19}^{+0.10}$
$0.01 \leq z \leq 0.3$ , $\log N_{\text{H}} < 22$ (316)	$44.17_{-0.20}^{+0.19}$	$-5.04_{-0.31}^{+0.36}$	$0.77_{-0.26}^{+0.16}$	$1.53_{-0.13}^{+0.21}$
$0.01 \leq z \leq 0.3$ , $22 \leq \log N_{\text{H}} < 24$ (263)	$44.30_{-0.19}^{+0.06}$	$-5.35_{-0.04}^{+0.40}$	$0.99_{-0.18}^{+0.13}$	$1.81_{-0.18}^{+0.17}$
$0.01 \leq z \leq 0.3$ , $\log N_{\text{H}} \geq 24$ (40)	$43.59_{-0.38}^{+0.23}$	$-4.51_{-0.44}^{+0.50}$	$0.33_{-0.40}^{+0.44}$	$1.81_{-0.57}^{+0.13}$
Type 1 AGNs only (366; all Table 1 cuts)	$44.12_{-0.22}^{+0.21}$	$-4.75_{-0.36}^{+0.27}$	$0.69_{-0.26}^{+0.22}$	$1.60_{-0.14}^{+0.22}$
Type 2 AGNs only (220; all Table 1 cuts)	$44.14_{-0.33}^{+0.13}$	$-4.88_{-0.49}^{+0.29}$	$0.93_{-0.26}^{+0.21}$	$1.75_{-0.21}^{+0.20}$
<b>All Table 1 Selection AGNs (586)</b>	$44.10_{-0.19}^{+0.20}$	$-4.46_{-0.44}^{+0.19}$	$0.83_{-0.25}^{+0.17}$	$1.60_{-0.12}^{+0.19}$

**Note.**

<sup>a</sup> For the XLF, we assume a double-power-law shape (see Equation (9)). All samples described here exclude sources falling within the Galactic plane ( $-5 < \text{latitude} < 5$ ), weak X-ray associations, dual sources falling below the flux limit of the survey, beamed sources, and sources with  $z > 0.3$ .

with respect to AGN luminosity, rather than an involved derivation of the intrinsic XLF (such as the XLFs presented in Gilli et al. 2007; Ueda et al. 2014; Aird et al. 2015; Buchner et al. 2015, and Ananna et al. 2019). Indeed, we report the  $1/V_{\text{max}}$ -based estimates (and fits) for all three distribution functions (BHMF, ERDF, and XLF) as a first-order approximation, as a way of making our results more directly and readily comparable with the observed distributions reported in previous studies (e.g., Greene & Ho 2009; Schulze & Wisotzki 2010; Ajello et al. 2012; Schulze et al. 2015).

#### 4.1. The XLF of Low-redshift AGNs

To determine the AGN XLF of the ultra-hard X-ray-selected AGNs, we use the  $1/V_{\text{max}}$  approach. As discussed in Section 3.2, we bin our sources according to their intrinsic 14–195 keV luminosities. When determining the corresponding space densities,

we take the flux–area curve and attenuation by high column densities into account (Figures 3, 4). Once we have determined  $\Phi_L$ , we fit the XLF with a double power law (Equation (9)). The  $1/V_{\text{max}}$  space densities are given in Appendix F (specifically, Table F5) and the best-fitting double-power-law parameters of the various subsamples we consider are given in Table 2. The analysis steps are further discussed in what follows.

In Figure 6, we present the XLF determined for the BASS/DR2 AGNs, regardless of their classification (i.e., both Type 1 and Type 2 sources). First, we use the redshifts, intrinsic 14–195 keV X-ray luminosities ( $L_{14-195 \text{ keV}}$ ), and column densities ( $N_{\text{H}}$ ) of all 672 nonbeamed, high-Galactic latitude BASS/DR2 AGNs at  $z \leq 0.3$ ; their XLF is shown in the left panel with the blue open squares and dotted blue line. Second, the left panel of Figure 6 shows the XLF of the 619 sources that meet our redshift restrictions ( $0.01 \leq z \leq 0.3$ ), *without* any corrections due to obscuration being applied to their selection

function. The only noticeable difference between the XLF of all BASS/DR2 AGNs and the redshift-restricted subsample is in the low- $L$  end. The redshift-restricted subsample lacks the 15 lowest- $L$  AGNs (i.e., in the  $\log[L_X/\text{erg s}^{-1}] < 42.25$  bins), which are also some of the lowest-redshift AGNs in BASS/DR2 (i.e.,  $z < 0.01$ ). At higher luminosities, the number of AGNs in each luminosity bin for the second sample is nonzero, and usually equal to the number of AGNs in the supersample. As shown in Figure 6 and Table F5, in a few bins, the redshift-restricted sample has slightly higher space densities than the supersample, even when the latter has more sources in those bins. This is possible because the lower redshift cut leads to smaller  $V_{\text{max}}$  (and therefore higher  $1/V_{\text{max}}$ ) values in some cases.

We further analyze the XLF of our samples in the right panel of Figure 6. In addition to the XLF of the redshift-restricted subsample, we show how this XLF changes when obscuration corrections are applied to the selection function. The obscuration corrections result in slightly higher values of  $1/V_{\text{max}}$  at all luminosities (as the  $V_{\text{max}}$  value of the obscured object is smaller). The  $1/V_{\text{max}}$  values and the corresponding errors are given in Tables F2 and F5. The best-fitting parameters for each XLF are shown in Table 2.

The correction due to obscuration is generally very small, which is to be expected, as the radiation in the 14–195 keV regime only starts to get attenuated beyond  $\log(N_{\text{H}}/\text{cm}^{-2}) \gtrsim 23$  in the local universe (as shown in Figure 4). Therefore, taking the effect of obscuration into account for ultra-hard X-rays may not lead to significant changes, unless the sample at hand preferentially selects heavily obscured sources. For example, the lowest-luminosity bin of the redshift-restricted sample contains a single object with  $\log(N_{\text{H}}/\text{cm}^{-2}) = 23.15$ , and therefore the effect of obscuration in that bin is noticeable, as shown in the right panel of Figure 6. As our sample includes both unobscured and heavily obscured sources, we apply an obscuration correction to all other  $1/V_{\text{max}}$  calculations, except for the two cases shown in Figure 6. In the figure, we show the  $1/V_{\text{max}}$  values and XLF fit to the sample used for the BHMF/ERDF analysis (after applying all cuts from Table 1).

Figure 6 also shows previous determinations of the ultra-hard XLF of low-redshift AGNs by Sazonov et al. (2007), Tueller et al. (2008), and Ajello et al. (2012). We also show the binned  $1/V_{\text{max}}$  XLF measurements of the latter study (black symbols). To convert these previous results to the 14–195 keV range we use here, we have assumed  $\Gamma = 1.8$ . For the results by Ajello et al. (2012), this implies  $L_{14-195 \text{ keV}} = 2.31 \times L_{15-55 \text{ keV}}$ . To convert from  $L_{20-40 \text{ keV}}$  and  $L_{17-60 \text{ keV}}$  to  $L_{14-195 \text{ keV}}$ , we used multiplicative factors of 4.34 and 2.33, respectively.

The left panel in Figure 6 shows that our parent sample of (unbeamed) BASS/DR2 AGNs reaches down to hard X-ray luminosities that are  $\approx 1$  dex fainter than the faintest luminosities covered by Ajello et al. (2012), which relied on the 60 month Swift/BAT all-sky catalog. As a natural result of the lower redshift cut at  $z = 0.01$ , our redshift-restricted sample ( $0.01 \leq z \leq 0.3$ ) only goes down to  $\log(L_X/\text{erg s}^{-1}) = 42.48$ , which is higher than the lowest luminosities reached by Ajello et al. (2012).

Overall, Figure 6 shows that the  $1/V_{\text{max}}$ -based  $\Phi_L$  values for our BASS/DR2 AGNs are in excellent agreement with previous results.

## 4.2. The XLF of AGNs with Various Levels of Absorption

The size of the BASS sample allows us to determine the XLF for various subsets of AGNs. In Figure 7, we split the AGNs by  $\log N_{\text{H}}$ , and calculate the binned XLF separately for unabsorbed Compton-thin [ $\log(N_{\text{H}}/\text{cm}^{-2}) < 22$ ], absorbed Compton-thin [ $22 \leq \log(N_{\text{H}}/\text{cm}^{-2}) < 24$ ], and Compton-thick [ $\log(N_{\text{H}}/\text{cm}^{-2}) \geq 24$ ] sources. For comparison, the blue solid lines in the top panels of Figure 7 illustrate the XLF for our redshift-restricted unbeamed AGN sample. For reference, in the top right panel of Figure 7, we also show the XLF of Compton-thick AGNs reported by Akylas et al. (2016). They used 53 Compton-thick AGNs selected from the the same parent catalog as the one we use (the Swift/BAT 70 month catalog), and determined a relatively low “break” luminosity in the 14–195 keV range,  $\log(L_X^*/\text{erg s}^{-1}) \simeq 42.8$ , compared to our value of  $43.59_{-0.23}^{+0.38}$ . Note that we also have 53 Compton-thick objects in our parent sample, 11 of which are at  $z < 0.01$ , one of which falls above  $z > 0.3$ , and another one of which is a faint dual source. Our individual  $1/V_{\text{max}}$   $\Phi_L$  values are generally consistent with the fit by Akylas et al. (2016), within errors, in all but the highest luminosity bin, although at  $\log(L_{14-195 \text{ keV}}/\text{erg s}^{-1}) > 44$  the Akylas et al. (2016) Compton-thick XLF lies above our data points. This may be caused by the different volumes considered, and/or by the fact that Akylas et al. (2016) uses a Poissonian MLE that considers individual sources, rather than a fit to  $1/V_{\text{max}}$  (see also Loredò 2004).

To further demonstrate the fractional densities of the  $\log N_{\text{H}}$  subsamples, the bottom panels of Figure 7 show the ratios between the space densities of each subsample compared to the entire sample, as a function of  $L_{14-195 \text{ keV}}$ . These ratios are computed using the  $1/V_{\text{max}}$   $\Phi_L$  values, and the errors on the ratios are calculated using the Wilson Score Interval method (Wilson 1927), which provides binomial confidence intervals without any assumption about the symmetry of the error bars.

We stress again that the XLFs and the related ratios shown in Figure 7 are estimated using the  $1/V_{\text{max}}$  method, and thus are for the observed sample of sources only. While these XLFs account for the effects of absorption on the sources observed in our survey, they do *not* account for absorbed populations that are completely missing from the sample due to selection biases (that are accounted for in more sophisticated studies, e.g., Ueda et al. 2014 and Ananna et al. 2019). Deriving such intrinsic  $N_{\text{H}}$ -dependent XLFs and ratios requires a much more involved approach than the  $1/V_{\text{max}}$  estimates we use here, which is beyond the scope of the present work.

We discuss the insights from Figure 7 in more detail in Section 5.

## 4.3. The BHMF and the ERDF of Local AGNs

To determine the BHMF and the ERDF for local AGNs, we use the  $M_{\text{BH}}$  and  $\lambda_{\text{E}}$  measurements of 586 ultra-hard X-ray-selected BASS/DR2 AGNs, as described in Section 2.2. Since the  $M_{\text{BH}}$  (and thus  $\lambda_{\text{E}}$ ) of Type 1 (broad-line) and Type 2 (narrow-line) BASS/DR2 AGNs are determined through two different approaches, with different systematics and potentially different selection effects in play, we first treat these two subsets separately, and only then address the BHMF and the ERDF of the total BASS/DR2 AGN sample.

To gain initial guesses for the two distribution functions, we use the  $1/V_{\text{max}}$  approach, assume functional forms, and fit the



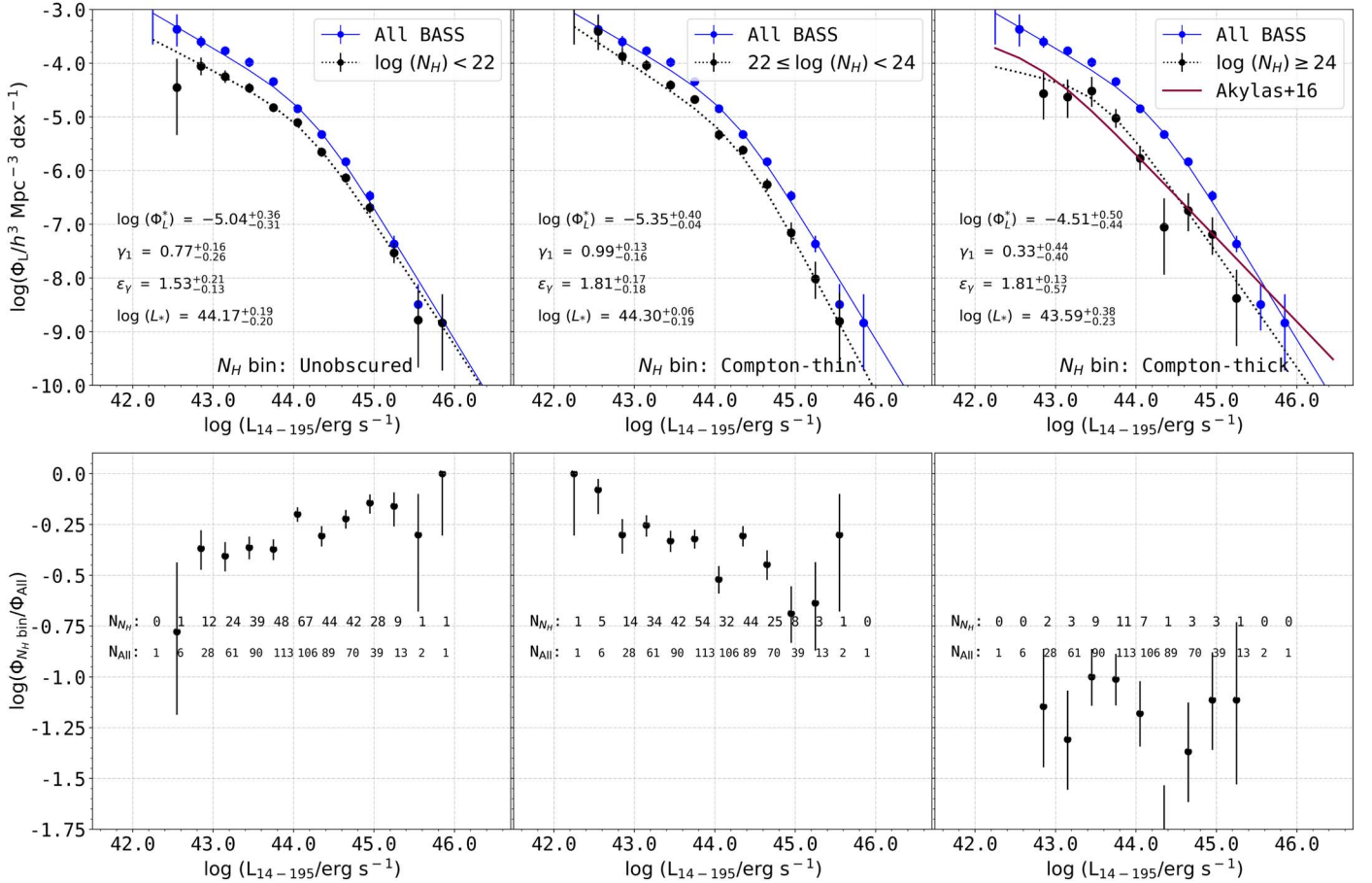


**Figure 7.** The XLFs for BASS AGNs in different regimes of  $N_{\text{H}}$ . Top panels: from left to right, the black points and black lines show the XLF for unobscured Compton-thin ( $N_{\text{H}} < 10^{22} \text{ cm}^{-2}$ ), obscured Compton-thin ( $10^{22} \text{ cm}^{-2} \leq N_{\text{H}} < 10^{24} \text{ cm}^{-2}$ ), and Compton-thick ( $N_{\text{H}} > 10^{24} \text{ cm}^{-2}$ ) AGNs. The XLF for the entire BASS sample is shown by the blue filled circles and the blue solid lines. Also shown in the top right panel is the XLF of the BAT Compton-thick AGNs from Akylas et al. (2016), which includes objects at  $z < 0.01$ , below the limit used in our analysis. Bottom panels: the ratios between the  $N_{\text{H}}$  subsample XLFs and the XLF of all AGNs in each  $\log L_{\text{X}}$  bin (the black data points), along with the associated Wilson score intervals (the black vertical lines). The numbers refer to the objects in each bin, with the upper and lower rows corresponding to the subsample and the full sample, respectively. These XLFs and ratios should be treated as representing the AGNs observed within BASS/DR2, in the corresponding absorption bins, rather than intrinsic XLFs (which would also account for the AGNs completely missed by our survey; see the main text).

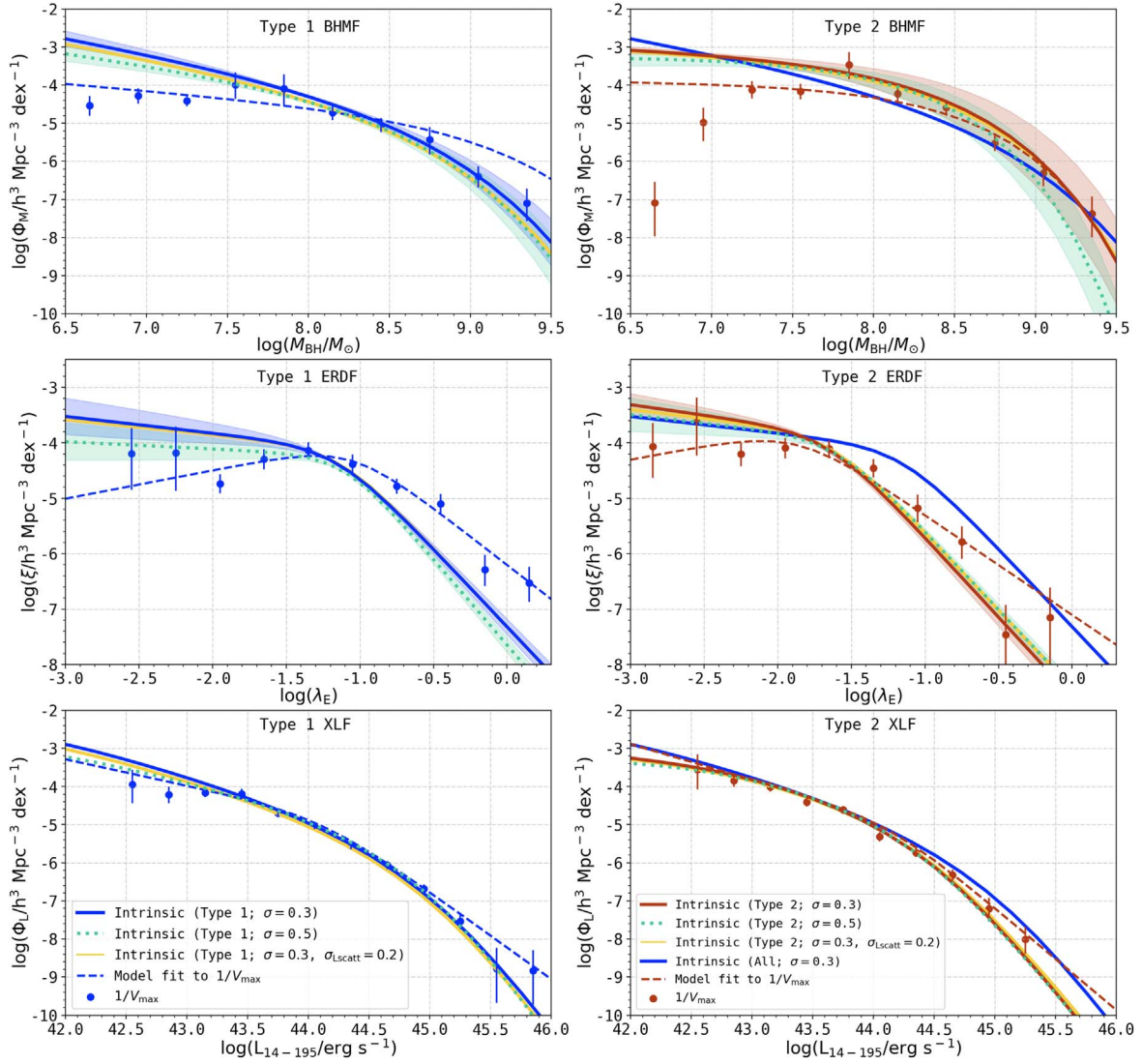
individual  $\Phi$  and  $\xi$  values independently. For the BHMF and the ERDF, we assume a modified Schechter function and a double power law, respectively (see Equations (10) and (11) in Section 3.3). To correct for sample truncation, i.e., the bias against low-mass and low-Eddington ratio AGNs, we use the parametric maximum likelihood approach outlined in Section 3.4. The  $1/V_{\text{max}}$  values for both the BHMF and the ERDF are given in Appendix F.

Figure 8 shows the BHMFs (top panels) and the ERDFs (center panels) for Type 1 and Type 2 BASS AGNs (the left and right columns), respectively. The two bottom panels of Figure 8 show the XLFs reproduced from these BHMFs and ERDFs, as explained below. Figure 9 presents the BHMF, ERDF, and XLF for the overall sample (Type 1 + Type 2) in a similar format. We recall that the normalizations are kept constant during the bias correction, and the method of computing them is described in Section 3.4.1. We are thus left with six free parameters: the break and two slopes of the BHMF ( $M_{\text{BH}}^*$ ,  $\alpha$ , and  $\beta$ ), and the break and two slopes of the ERDF ( $\lambda_{\text{E}}^*$ ,  $\delta_1$ , and  $\delta_2$ ). We note that the high- $\lambda_{\text{E}}$  slope,  $\delta_2$ , is parameterized as  $\delta_1 + \epsilon_{\lambda}$ , with  $\epsilon_{\lambda} > 0$ . We vary  $\delta_1$  and  $\epsilon_{\lambda}$  in the MCMC. We also recall that for the bias correction we assume uncertainties of 0.3 dex and 0.5 dex on both  $\log M_{\text{BH}}$  and  $\log \lambda_{\text{E}}$

(see Equations (18) and (20)), as well as an additional scenario with  $\sigma_{\log M_{\text{BH}}} = 0.3$  and  $\sigma_{\log L_{\text{scatt}}} = 0.3$  (i.e.,  $\sigma_{\log \lambda_{\text{E}}} = 0.36$ ). The results from all these different  $\sigma$  values reassuringly converge on the same solution, as shown in the figure. In Appendix E, we present the BHMF/ERDF calculated by assuming a luminosity-dependent bolometric correction from Duras et al. (2020). Note that we prefer the constant bolometric correction because it minimizes the number of assumptions we have to make, and because there is some conflict between different prescriptions of luminosity-dependent bolometric corrections (shown in Figure 6 of Duras et al. 2020), and it is unclear which prescription is the most accurate.

The contour plots presenting the likelihoods resulting from our MCMC analysis are shown in Figure F1 in Appendix F. The best-fitting BHMF and ERDF parameters for all three samples are given in Tables 3 and 4, respectively. Note that we also report the results assuming an attenuation curve and absorption function calculated using a torus opening angle of  $35^\circ$  (as discussed in Section 3.4.2) in these tables. As shown in Figure F2, our final results for both torus geometries are consistent with each other.

As discussed in Section 1, and shown in detail in Appendix D, the bolometric LF corresponds to the convolution



**Figure 8.** BH mass, Eddington ratio, and luminosity distribution functions of BASS/DR2 Type 1 (left panels) and Type 2 (right panels) AGNs. For both types of AGNs, combining the BHMf (top row) and the ERDF (middle row) reproduces the observed XLF (bottom row). The data points come from the  $1/V_{\max}$  analysis, and the dashed lines represent the fits to these data points. The solid lines and the shaded areas show the final, bias-corrected intrinsic distribution functions. The lines of different colors trace the intrinsic distributions, assuming various levels of uncertainty (see the legends for details). Specifically, the blue (left) and red (right) solid lines assume uncertainties of  $\sigma_{\log M_{\text{BH}}} = \sigma_{\log \lambda_{\text{E}}} = 0.3$ ; the orange solid lines assume  $\sigma_{\log M_{\text{BH}}} = 0.3$  and  $\sigma_{\log L_{\text{scatt}}} = 0.2$  (or  $\sigma_{\log \lambda_{\text{E}}} = 0.36$ ); and the green dotted lines assume  $\sigma_{\log M_{\text{BH}}} = \sigma_{\log \lambda_{\text{E}}} = 0.5$  dex. The intrinsic distributions of Type 1 AGNs (assuming  $\sigma = 0.3$ ) are also shown in the right panels, to highlight the differences between Type 1 and 2 AGNs. Note that the  $1/V_{\max}$  points shown for each subset of AGNs were calculated by considering only the AGNs of the respective type (i.e., Type 1 or 2 AGNs). The  $1/V_{\max}$  values are reported in Tables F2–F4.

of the BHMf and the ERDF. By “reversing” the bolometric correction, the XLF can thus be predicted from the best-fit BHMf and ERDF. We test if the bias-corrected BHMfs and ERDFs for each subset of AGNs (i.e., Type 1, Type 2, and the overall sample) allow us to predict the corresponding observed XLF. Note that for the convolution, we use the normalized ERDF (see Equation (32)). The normalization of the predicted XLF is thus driven by the normalization of the BHMf.

Figures 8 and 9 illustrate the importance of bias correction. For the BHMf, relying solely on the model fit to  $1/V_{\max}$  values would have led us to underestimate the space density of low-mass AGNs at the lowest-mass bin ( $\log[M_{\text{BH}}/M_{\odot}] = 6.65$ ) by  $\gtrsim 1$  dex for both Type 1 and Type 2 sources. At low  $M_{\text{BH}}$  and/or  $\lambda_{\text{E}}$ , the  $1/V_{\max}$  method underestimates the intrinsic space density of AGNs, due to the survey’s incompleteness. At high  $M_{\text{BH}}$  and/or  $\lambda_{\text{E}}$ , the  $1/V_{\max}$  method *overestimates* the intrinsic AGN space densities, due to the uncertainties

associated with the key AGN parameters. As shown by the mock catalogs (Figures D1 and D2), and Figure 17 of S15, as measurement uncertainty ( $\sigma_{\log M_{\text{BH}}}$ ,  $\sigma_{\log \lambda_{\text{E}}}$ ) increases, this overestimation increases at the high- $M_{\text{BH}}$  and/or high- $\lambda_{\text{E}}$  end. This effect is a manifestation of the so-called Eddington bias (Eddington 1913): the uncertainty causes objects from lower- $M_{\text{BH}}$  (or lower- $\lambda_{\text{E}}$ ) bins to scatter into higher- $M_{\text{BH}}$  (or higher- $\lambda_{\text{E}}$ ) bins, and vice versa. Intrinsically, there are always fewer objects with higher  $M_{\text{BH}}$  (or  $\lambda_{\text{E}}$ ), therefore the scattering from the lower to the higher bins causes significant overestimation of the space densities in the higher bins. The bottom panels in Figures 8 and 9 demonstrate that our convolution-based reconstruction of the XLF matches what we measure directly from observations.

Figure 8 shows that the normalization of the bias-corrected BHMf of Type 2 AGNs is higher than that of Type 1 AGNs at most masses. The bias-corrected ERDF of Type 2 AGNs has

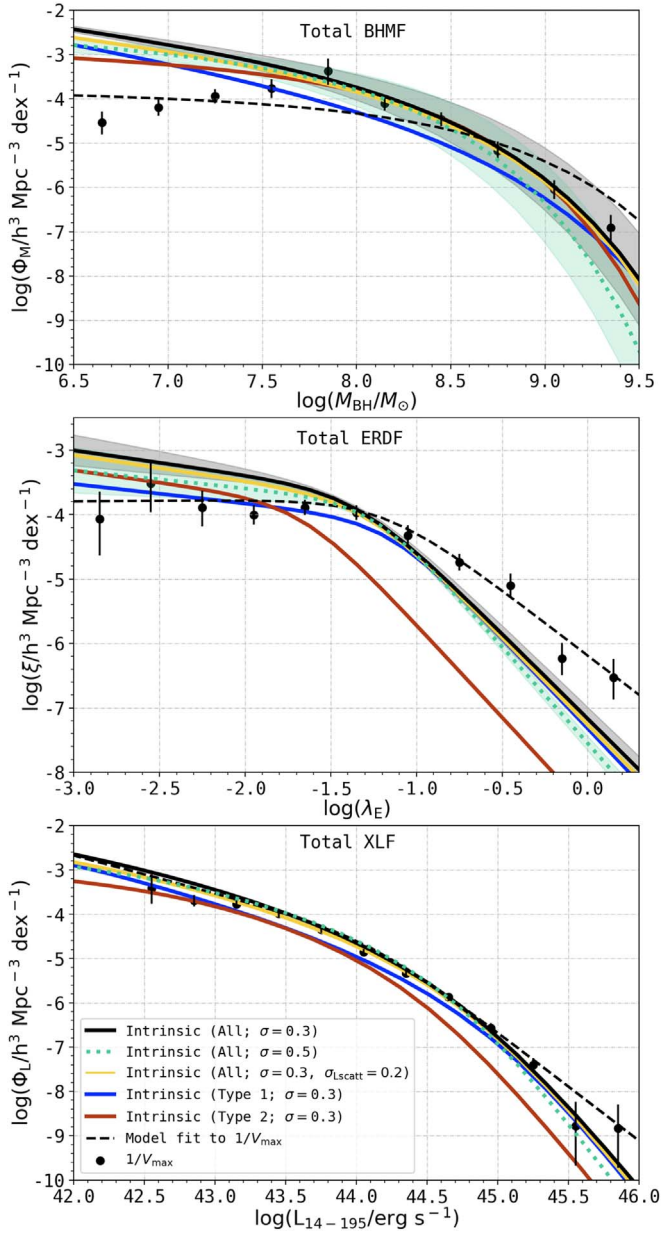


**Figure 9.** Distribution functions for all BASS/DR2 AGNs that fall within the criteria specified in Table 1 (586 sources). As in Figure 8, the BHMf, ERDFs, and reconstructed XLFs are shown in the top, middle, and bottom panels, respectively. We show the intrinsic distributions derived for all AGNs, assuming uncertainties of either  $\sigma = 0.3$  dex or  $\sigma = 0.5$  dex in  $\log M_{\text{BH}}$  and  $\log \lambda_{\text{E}}$  (the black solid and green dotted lines), respectively. The orange solid lines show intrinsic functions, derived assuming  $\sigma_{\log M_{\text{BH}}} = 0.3$  and  $\sigma_{\log L_{\text{scatt}}} = 0.2$  (or  $\sigma_{\log \lambda_{\text{E}}} = 0.36$ ). The black data points in the bottom panel show the direct  $1/V_{\text{max}}$  XLF estimates, and the black dashed line is the fit to those points. The solid black lines show the final, bias-corrected intrinsic distribution functions for the complete AGN sample. For comparison, we also show the distribution functions of Type 1 and Type 2 AGNs (the blue and red lines), respectively, from Figure 8.

higher space densities at  $\log \lambda_{\text{E}} \leq -1.7$ . Beyond this point, the ERDF of Type 2 AGNs drops off rapidly below the ERDF of Type 1 AGNs. This is because the break in the ERDF of Type 2 AGNs is at  $\log \lambda_{\text{E}} = -1.657^{+0.087}_{-0.064}$ , which is significantly below the break of the Type 1 AGNs at  $\log \lambda_{\text{E}} = -1.152^{+0.089}_{-0.053}$ . Figure 9 shows the Type 1 and Type 2 BHMf, ERDFs, and XLFs, along with the overall sample results.

Figure 10 illustrates how we can use the bivariate distribution (i.e.,  $\Psi$ ) to reproduce the (univariate) BHMf and ERDF, following Equation (23). In the top panels, we show how the bivariate distribution varies as a function of  $\log M_{\text{BH}}$  and  $\log \lambda_{\text{E}}$  for Type 1 (left panels) and Type 2 (right panels) AGNs. We also indicate the intervals over which we integrate to produce the BHMf and ERDFs, as shown in the lower panels. In the middle panels, we show the reconstructed BHMf for two bins of  $\log \lambda_{\text{E}}$  (bin widths of 0.3 dex), as well as the integrated BHMf (over all  $\lambda_{\text{E}}$  we consider). Similarly, the bottom panels show the reconstructed ERDFs for two  $\log M_{\text{BH}}$  bins (bin widths of 0.3 dex), as well as the integrated ERDF over all  $M_{\text{BH}}$ . We note that, in a graphical sense, the reconstructed XLFs would correspond to integrating the bivariate distribution along antidiagonal stripes (see the top left panel in Figure 10), illustrating that the bivariate distribution function fully captures the statistical properties of AGNs.

Note that there is some degeneracy between several pairs of parameters describing the fitting functions, as shown in our MCMC chain contour plots in Appendix F (Figure F1). For all three AGN populations (Type 1, Type 2, and overall), the parameters of the BHMf show significant correlation. The pairs of parameters  $(\alpha, \beta)$  and  $(\alpha, \log M_{\text{BH}}^*)$  seem to be anticorrelated, while the pair  $(\beta, \log M_{\text{BH}}^*)$  is positively correlated. These trends are expected: while fitting the same intrinsic population, if we fix the break in the BHMf at a higher mass, the slope at low mass ( $\alpha$ ) has to be shallower, and the slope at high mass ( $\beta$ ) has to be steeper, to compensate for the higher mass break and to produce a good fit. For the ERDF, the slopes  $(\delta_1 - \epsilon_{\lambda})$  are negatively correlated for all three samples. The break of the ERDF ( $\log \lambda_{*}$ ) is weakly positively correlated with  $\delta_1$ , and shows no significant correlation with  $\epsilon_{\lambda}$ . The figure also shows that even when these functions converge to the same distribution for one parameter, it may occupy distinctly different locations in six-dimensional parameter space. These degeneracies should be kept in mind when one tries to directly compare individual fitting parameters within our own analysis (e.g., between Type 1 and Type 2 AGNs), or when comparing our best-fit parameters to those found in other studies. In what follows, instead of comparing the values of individual parameters, we often refer to the similarities (or lack thereof) in the shapes of certain fitting functions shown in the figure.

In Figure 11, we compare the BASS BHMf and ERDFs for Type 1 AGNs (left panels) and Type 2 AGNs (right panels) to previously published determinations of these distributions. In the top panels, we show the  $1/V_{\text{max}}$   $\Phi$  values and the bias-corrected BHMf in blue (left panels; Type 1) and red (right panels; Type 2). In the top left panels, the green data points show the  $\Phi$  values determined by Greene & Ho (2007, 2009), based on a large sample of SDSS AGNs with broad  $\text{H}\alpha$  lines, which is not corrected for sample truncation. The yellow data points and dashed-dotted line illustrate the  $1/V_{\text{max}}$   $\Phi$  values and the incompleteness-corrected distribution, respectively, as determined by SW10, based on the quasar sample of HES (Wisotzki et al. 2000). Note that SW10 does not correct for measurement uncertainties. The purple dashed lines in Figure 11 show the BHMf and ERDF determined by Schulze et al. (2015), based on a joint analysis of  $1 < z < 2$  AGNs from the SDSS, zCOSMOS, and VVDS samples (Schneider et al. 2010; Lilly et al. 2009 and Gavignaud et al. 2008,

**Table 3**  
Sample Truncation-corrected BHMFs<sup>a</sup> and Fits to  $1/V_{\max}$  Values for the BHMFs for Type 1 AGNs, Type 2 AGNs, and Both Samples Together<sup>b</sup>

	$\log(M_{\text{BH}}^*/M_{\odot})$	$\log(\Psi^*/h^3 \text{ Mpc}^{-3})$	$\alpha$	$\beta$
All				
Intrinsic ( $\sigma = 0.3$ )	$7.88^{+0.21}_{-0.22}$	$-3.52$	$-1.576^{+0.147}_{-0.078}$	$0.593^{+0.078}_{-0.069}$
Intrinsic ( $\sigma = 0.3; \sigma_{\log L, \text{scatt}} = 0.2$ )	$7.92^{+0.13}_{-0.22}$	$-3.67$	$-1.530^{+0.114}_{-0.094}$	$0.612^{+0.053}_{-0.063}$
Intrinsic ( $\sigma = 0.5$ )	$7.67^{+0.25}_{-0.20}$	$-3.37$	$-1.26^{+0.19}_{-0.11}$	$0.630^{+0.065}_{-0.086}$
Intrinsic ( $\sigma = 0.3; \text{OA} = 35^\circ$ )	$7.92^{+0.18}_{-0.27}$	$-3.49$	$-1.576^{+0.057}_{-0.137}$	$0.600^{+0.066}_{-0.082}$
$1/V_{\max}$	$8.12^{+0.14}_{-0.11}$	$-4.33^{+0.22}_{-0.37}$	$-1.06^{+0.12}_{-0.30}$	$0.574^{+0.112}_{-0.040}$
Type 1				
Intrinsic ( $\sigma = 0.3$ )	$7.97^{+0.17}_{-0.30}$	$-4.19$	$-1.753^{+0.137}_{-0.088}$	$0.561^{+0.062}_{-0.073}$
Intrinsic ( $\sigma = 0.3; \sigma_{\log L, \text{scatt}} = 0.2$ )	$7.93^{+0.25}_{-0.22}$	$-4.27$	$-1.73 \pm 0.11$	$0.566^{+0.085}_{-0.071}$
Intrinsic ( $\sigma = 0.5$ )	$7.91^{+0.16}_{-0.27}$	$-4.27$	$-1.56 \pm 0.13$	$0.590^{+0.104}_{-0.050}$
$1/V_{\max}$	$8.73^{+0.26}_{-0.31}$	$-5.10^{+0.26}_{-0.50}$	$-1.35^{+0.18}_{-0.23}$	$0.681^{+0.087}_{-0.114}$
Type 2				
Intrinsic ( $\sigma = 0.3$ )	$7.82^{+0.15}_{-0.26}$	$-3.6$	$-1.16^{+0.14}_{-0.20}$	$0.637^{+0.067}_{-0.075}$
Intrinsic ( $\sigma = 0.3; \sigma_{\log L, \text{scatt}} = 0.2$ )	$7.79^{+0.17}_{-0.22}$	$-3.64$	$-1.18^{+0.16}_{-0.17}$	$0.617^{+0.100}_{-0.044}$
Intrinsic ( $\sigma = 0.5$ )	$7.76^{+0.19}_{-0.15}$	$-3.6$	$-0.99^{+0.21}_{-0.19}$	$0.703^{+0.086}_{-0.069}$
Intrinsic ( $\sigma = 0.3; \text{OA} = 35^\circ$ )	$7.73^{+0.25}_{-0.12}$	$-3.44$	$-1.26^{+0.17}_{-0.16}$	$0.635^{+0.085}_{-0.053}$
$1/V_{\max}$	$8.102^{+0.172}_{-0.095}$	$-4.33^{+0.19}_{-0.23}$	$-1.04^{+0.30}_{-0.29}$	$0.732^{+0.074}_{-0.050}$

**Notes.**

<sup>a</sup> We assume a modified Schechter function (see Equation (10)) for the BHMF.

<sup>b</sup> We use a constant bolometric correction (Equation (2)) to compute these results.

**Table 4**  
Sample Truncation-corrected ERDFs<sup>a</sup> and Fits to  $1/V_{\max}$  Values for the ERDFs for Type 1 AGNs, Type 2 AGNs, and the Full AGN Sample<sup>b</sup>

	$\log \lambda_{\text{E}}^*$	$\log(\xi^*/h^3 \text{ Mpc}^{-3})$	$\delta_1$	$\epsilon_{\lambda}$
All				
Intrinsic ( $\sigma = 0.3$ )	$-1.338 \pm 0.065$	$-3.64$	$0.38^{+0.12}_{-0.10}$	$2.260^{+0.121}_{-0.082}$
Intrinsic ( $\sigma = 0.3; \sigma_{\log L, \text{scatt}} = 0.2$ )	$-1.286^{+0.059}_{-0.076}$	$-3.76$	$0.40 \pm 0.12$	$2.322^{+0.095}_{-0.105}$
Intrinsic ( $\sigma = 0.3; \text{OA} = 35^\circ$ )	$-1.332^{+0.077}_{-0.068}$	$-3.68$	$0.484^{+0.091}_{-0.133}$	$2.210^{+0.066}_{-0.106}$
Intrinsic ( $\sigma = 0.5$ )	$-1.249^{+0.059}_{-0.061}$	$-3.8$	$0.28^{+0.13}_{-0.12}$	$2.72^{+0.13}_{-0.14}$
$1/V_{\max}$	$-1.19^{+0.23}_{-0.21}$	$-3.76^{+0.18}_{-0.30}$	$-0.02^{+0.29}_{-0.39}$	$2.06^{+0.30}_{-0.27}$
Type 1				
Intrinsic ( $\sigma = 0.3$ )	$-1.152^{+0.053}_{-0.089}$	$-4.08$	$0.30 \pm 0.14$	$2.51^{+0.11}_{-0.15}$
Intrinsic ( $\sigma = 0.3; \sigma_{\log L, \text{scatt}} = 0.2$ )	$-1.138^{+0.070}_{-0.058}$	$-4.09$	$0.27^{+0.13}_{-0.12}$	$2.57^{+0.12}_{-0.16}$
Intrinsic ( $\sigma = 0.5$ )	$-1.103^{+0.065}_{-0.054}$	$-4.23$	$0.13^{+0.15}_{-0.14}$	$2.97^{+0.18}_{-0.19}$
$1/V_{\max}$	$-1.06^{+0.28}_{-0.25}$	$-4.02^{+0.22}_{-0.32}$	$-0.51^{+0.53}_{-0.41}$	$2.57^{+0.33}_{-0.45}$
Type 2				
Intrinsic ( $\sigma = 0.3$ )	$-1.657^{+0.064}_{-0.087}$	$-3.82$	$0.376^{+0.099}_{-0.253}$	$2.50 \pm 0.17$
Intrinsic ( $\sigma = 0.3; \sigma_{\log L, \text{scatt}} = 0.2$ )	$-1.628^{+0.079}_{-0.084}$	$-3.84$	$0.32^{+0.18}_{-0.20}$	$2.50 \pm 0.17$
Intrinsic ( $\sigma = 0.3; \text{OA} = 35^\circ$ )	$-1.675^{+0.091}_{-0.067}$	$-3.8$	$0.33^{+0.15}_{-0.20}$	$2.51^{+0.14}_{-0.16}$
Intrinsic ( $\sigma = 0.5$ )	$-1.593^{+0.080}_{-0.096}$	$-3.92$	$0.30^{+0.21}_{-0.20}$	$2.53^{+0.26}_{-0.11}$
$1/V_{\max}$	$-1.87^{+0.38}_{-0.40}$	$-3.74^{+0.35}_{-0.43}$	$-0.50^{+1.08}_{-0.56}$	$2.30^{+0.81}_{-0.69}$

**Notes.**

<sup>a</sup> We assume a double-power-law shape for the ERDF (see Equation (11)).

<sup>b</sup> We use a constant bolometric correction (Equation (2)) to compute these results.

respectively). Note that the Schulze et al. (2015) BHMF and ERDF for Type 2 AGNs are *predicted* from the corresponding distributions for Type 1 AGNs, by assuming a luminosity-dependent fraction of obscured systems, which is in turn determined from X-ray surveys. The higher space densities of the Schulze et al. (2015) BHMFs and ERDFs are expected, given the well-known redshift evolution of AGN abundance (e.g., Aird et al. 2015; Caplar et al. 2015; Aird et al. 2018;

Shen et al. 2020). The turquoise shaded region in the top panels of Figure 11 also shows the *total* local BHMF—that is, including both active and inactive SMBHs—determined by Shankar et al. (2009). The total BHMF naturally occupies a much higher space density than our BASS AGNs-only BHMF. The recent study by Shankar et al. (2020) used a different set of  $M_{\text{BH}} - \sigma$  relations (discussed in Section 2.2) to derive an updated total BHMF. However, as our analysis relies on the more widely used  $M_{\text{BH}} - \sigma$

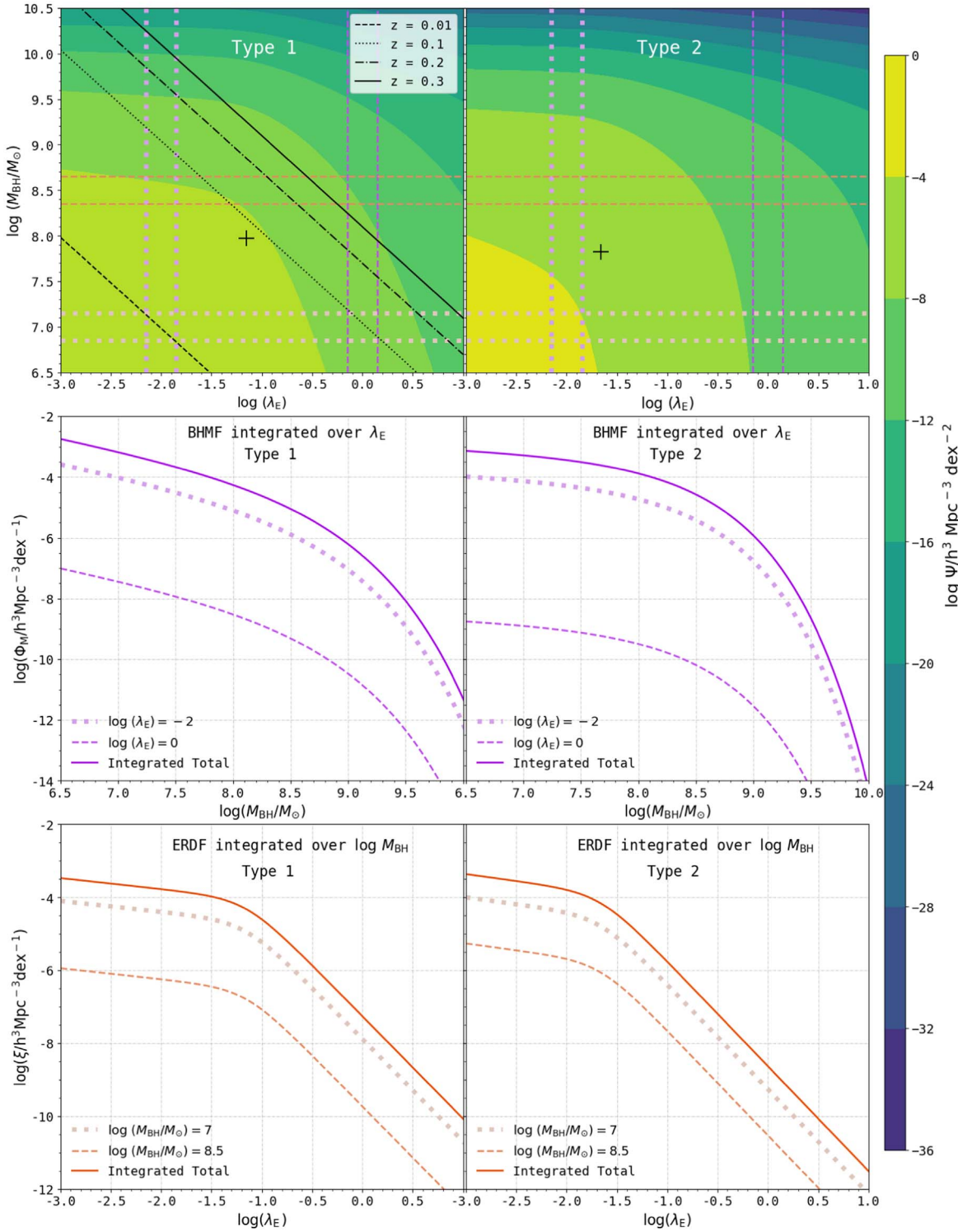


**Figure 10.** Contour plots of the best-fit bivariate distribution functions (top panels), BHMf marginalized over bins of  $\log \lambda_E$  (middle panels), and ERDF marginalized over bins of  $\log M_{\text{BH}}$  (bottom panels). Type 1 AGNs are shown on the left, with Type 2 AGNs on the right. In the top panels, the contours highlight the levels of constant  $\Psi$  values, with  $\log$ -uniform spacing (see the color bar); the black crosses mark the positions of  $[\log(\lambda_E^*), \log(M_{\text{BH}}^*/M_\odot)]$ ; and the black lines highlight the flux limits at different redshifts. In the middle panels, we show the integrals for  $\log \lambda_E = -2 \pm 0.15$  (the dotted pink lines),  $\log \lambda_E = 0 \pm 0.15$  (the dashed pink lines), and all  $\log \lambda_E$  (the solid pink lines). In the bottom panels, we show the integrals for  $\log(M_{\text{BH}}/M_\odot) = 7 \pm 0.15$  (the dotted orange lines),  $\log(M_{\text{BH}}/M_\odot) = 8.5 \pm 0.15$  (the dashed orange lines), and all  $\log(M_{\text{BH}}/M_\odot)$ . Each  $\log \lambda_E$  and  $\log(M_{\text{BH}}/M_\odot)$  bin over which a function is marginalized is shown in the top panels in the corresponding color and line style (e.g., the purple dashed lines show the  $\log \lambda_E$  range over which the BHMf is marginalized, and the result of the marginalization is shown with the dashed purple lines in the middle panels). For the purpose of this plot, we assume a constant flux limit of  $\log(F_{14-195 \text{ keV}}/\text{erg s}^{-1}) = -11.1$  (which corresponds to a sky coverage completeness of just 2%–3%; see Figure 3). The lines of the constant flux limits in the top left panel are also lines of constant luminosity, and integrating along these lines produces the local XLF. This figure demonstrates that the bivariate distribution function fully captures the statistical properties of AGNs.

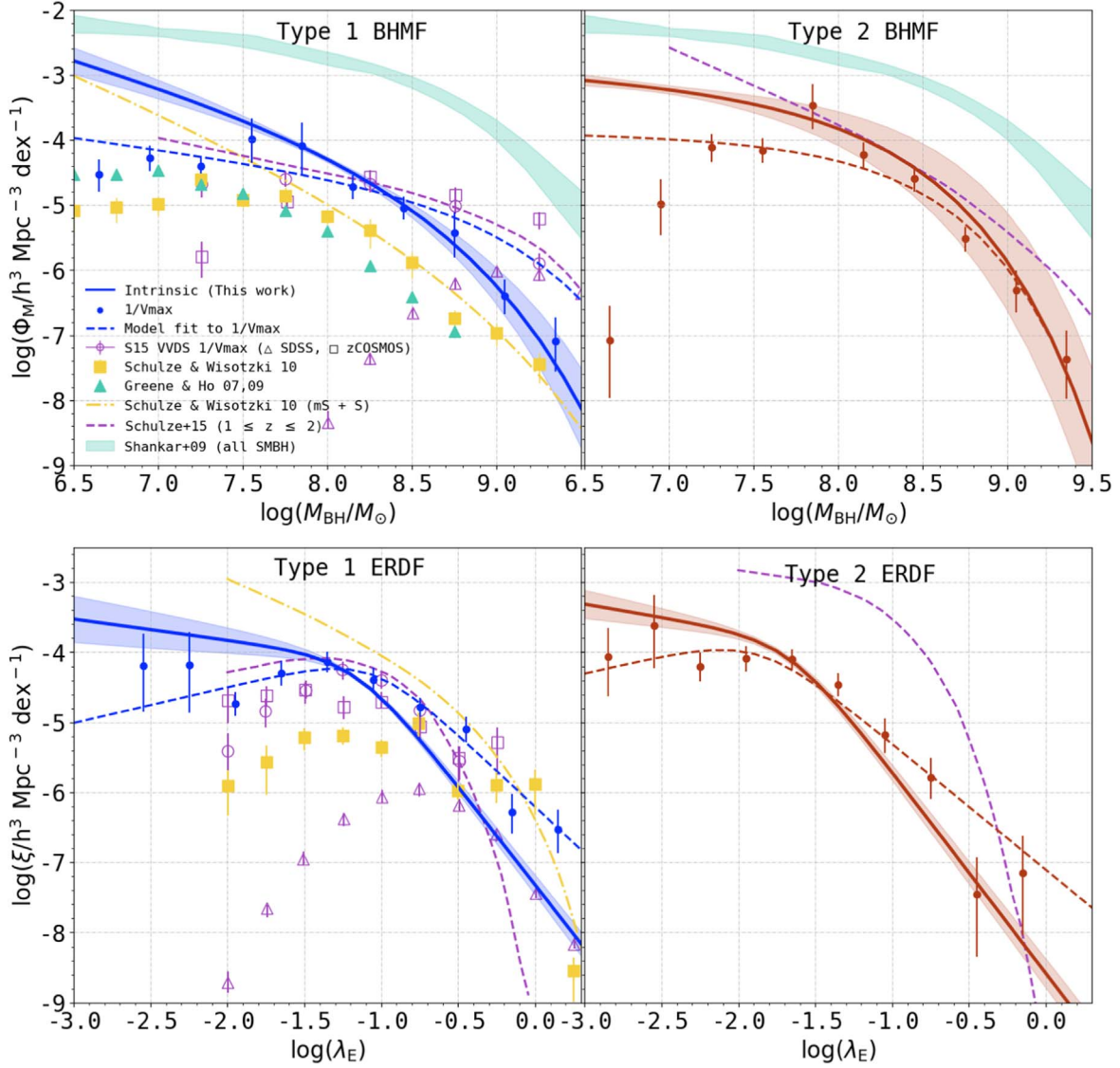


**Figure 11.** Comparisons of the BASS BHMFs and ERDFs for Type 1 AGNs (left panels) and Type 2 AGNs (right panels) to previous studies. The blue/red solid lines show the *intrinsic* BASS BHMFs and ERDFs. Top panels: the BHMFs of Type 1 and Type 2 AGNs. The green triangles show the bias-uncorrected  $1/V_{\max}$  results from Greene & Ho (2007, 2009), calculated using a sample of local broad-line AGNs from SDSS. The yellow squares and dashed-dotted lines show the  $1/V_{\max}$  and incompleteness-corrected (but not uncertainty-corrected) BHMFs of Schulze & Wisotzki (2010), calculated using local broad-line AGNs from HES. The fully bias-corrected Type 1 BHMf and predicted Type 2 BHMf from Schulze et al. (2015), evaluated at  $1 < z < 2$ , are shown with the purple dashed lines. The  $1/V_{\max}$  points from Schulze et al. (2015), constrained using VVDS, SDSS, and zCOSMOS data sets, are also shown using open purple circles, open purple triangles, and open purple squares, respectively. For reference, we also plot the total BHMf (including inactive BHs) from Shankar et al. (2009; the turquoise shaded region). Bottom panels: the ERDFs of Type 1 and Type 2 AGNs. The data points and lines from Schulze & Wisotzki (2010) and Schulze et al. (2015) follow the same scheme as in the top panels.

relation of Kormendy & Ho (2013), we do not compare our results with the Shankar et al. (2020) BHMf.

#### 4.4. Mass Independence of the ERDF Shape

We used our BASS/DR2 sample to directly verify that our assumption of a mass-independent ERDF is a reasonable assumption, at least for the data in hand. To this end, we divided each of the Type 1 and Type 2 AGN subsamples into two broad mass bins,  $\log(M_{\text{BH}}/M_{\odot}) \leq 7.8$  and  $\log(M_{\text{BH}}/M_{\odot}) \geq 8.2$ . The 0.4 dex wide gap in  $\log M_{\text{BH}}$  was imposed to minimize the “mixing” between the mass bins, due to uncertainties on the  $M_{\text{BH}}$  estimation. We then derived the  $1/V_{\max}$  measurements (which are susceptible to selection

biases, as discussed in detail in Section 3), the associated functional fits of these measurements, and the bias-corrected intrinsic functional forms for each of the four subsamples (Type 1s and Type 2s, low-mass and high-mass), following the same methodology as used for our main analysis.

The results of this analysis are shown in Figure 12. We find that the *shapes* of the bias-corrected intrinsic distributions of the low-mass and high-mass bins—that is, the power-law exponents and the locations of the breaks—are in excellent agreement (for each of the AGN subtypes), as can also be seen from the best-fit parameters (Table F1). The low-mass subsets naturally have higher number densities (i.e., normalizations), as expected, given the generally decreasing nature of the BHMf with increasing  $M_{\text{BH}}$ . This analysis indicates that the shape of

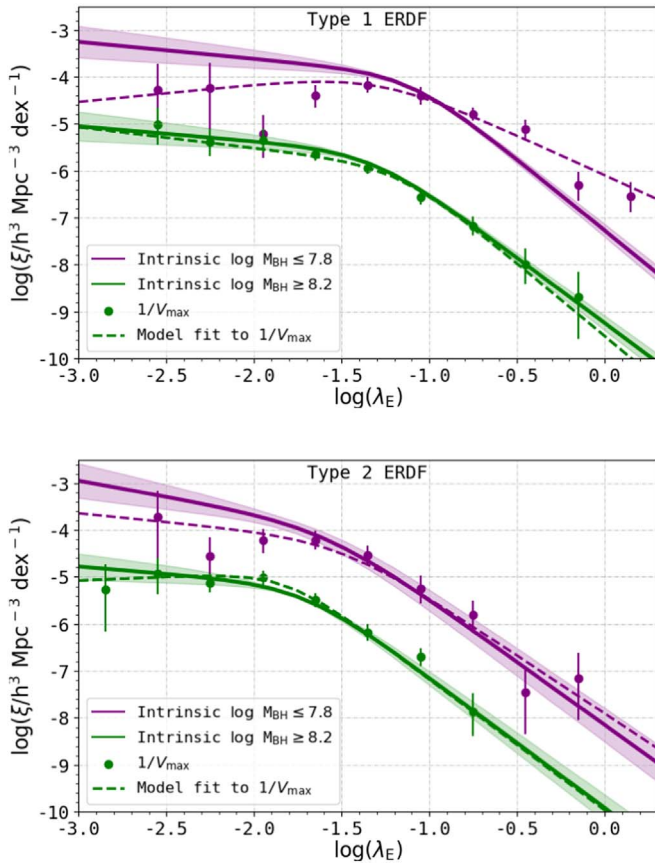


**Figure 12.** The ERDFs of Type 1 (top panel) and Type 2 (bottom panel) AGNs, divided into two mass bins:  $\log M_{\text{BH}} \leq 7.8$  (the purple lines and points) and  $\log M_{\text{BH}} \geq 8.2$  (the green lines and points). The data points represent  $1/V_{\text{max}}$  in each  $\lambda_E$  bin, the dashed lines represent the fits to the  $1/V_{\text{max}}$  points, and the solid lines represent the bias-corrected intrinsic distribution functions. Dividing the sample in this way shows that, for both Type 1 and Type 2 AGNs, the shape of the ERDF is independent of mass.

the ERDF is indeed mass-independent, for both obscured and unobscured AGNs.

## 5. Discussion

We have derived the XLF, BHMF, and ERDF of a large, complete sample of ultra-hard X-ray-selected, low-redshift AGNs from the BASS/DR2 data set. Our analysis has included the direct  $1/V_{\text{max}}$  approach, as well as an elaborate inference scheme that allowed us to recover the intrinsic distribution functions, accounting for numerous generic, AGN-related, and survey-specific potential biases. In both cases, we derived functional fits to the distribution functions, considering the combined BASS/DR2 sample of (nonbeamed) AGNs, as well as subsamples based on the AGN optical spectral classes (Type 1s and Type 2s) and line-of-sight obscuration (parameterized by their  $N_{\text{H}}$ ). We finally demonstrated that the intrinsic BHMF and ERDF can be combined to reproduce the XLF, and that the assumption of the mass-independence of the shape of the ERDF is justified, at least for our sample.

Before moving to a higher-level discussion, we briefly list the main results of our main analyses:

1. Our main results are the intrinsic BHMFs and ERDFs for Type 1 and Type 2 AGNs, presented in Figure 8 and Tables 3 and 4. The method used to derive these

functions overcomes the limitations of the  $1/V_{\text{max}}$  approach (e.g., the Eddington bias; Eddington 1913) and incompleteness at low luminosities, masses, and/or accretion rates.

2. We show the source number counts for all the AGN samples drawn from the Swift/BAT 70 month catalog in Figure 2, and provide the best-fit power-law slopes and normalizations of the differential number counts for all samples under study in Section 2.3.
3. We present the overall XLFs in Figure 6. The key observed quantities for these XLFs (i.e.,  $1/V_{\text{max}}$ -based space densities) are given in Tables F2 and F5, while their best-fit, broken power-law parameters are given in Table 2.
4. We present the XLFs of unabsorbed objects, Compton-thin objects, and Compton-thick objects separately in Figure 7. The corresponding  $1/V_{\text{max}}$  values and best-fit parameters are given in Tables F6 and 2, respectively.
5. The  $1/V_{\text{max}}$  fits to the BHMFs, ERDFs, and XLFs of Type 1, Type 2, and combined AGN samples are given in Tables F3, F4, and F2, respectively. The parameter fits to the *observed*  $1/V_{\text{max}}$ -based measurements for all three distributions, as well as the *intrinsic* BHMF and ERDF, are given in Tables 3, 4, and 2 (again, respectively). The top (BHMF), middle (ERDF), and bottom (XLF) panels in Figures 8 and 9 show the observed quantities and the (intrinsic) best-fit distribution functions.

We next discuss several higher-level topics pertaining to the population of accreting SMBHs in the local universe, based on the results of our main analysis. In particular, we (1) discuss the relation between accretion power and (circumnuclear) obscuration; (2) compare the intrinsic BHMF and ERDF to earlier studies, and discuss possible ways of interpreting their shapes; and (3) discuss the AGN duty cycle.

### 5.1. AGN Obscuration and Demographics

Our analysis of the BASS/DR2 sample offers several insights concerning the role of obscuration in the distributions describing the (low-redshift) AGN population. First, we have fully considered the effect of line-of-sight obscuration on the derived intrinsic luminosity of every AGN in our sample, and thus on the derived XLF (as well as the BHMF and the ERDF). This is motivated by the significant attenuation expected for highly obscured sources [ $\log(N_{\text{H}}/\text{cm}^{-2}) > 23$ ], even in the ultra-hard 14–195 keV band (i.e., Figure 4).

Second, the BASS sample allowed us to construct and explore the XLF for AGNs of several  $N_{\text{H}}$  regimes. The top panels of Figure 7 show the XLFs in each of the three  $N_{\text{H}}$  bins, while the bottom panels show the fractions of objects in each  $N_{\text{H}}$  bin relative to all AGNs (in a luminosity-resolved way; see the details in Section 4.2). We find that (1) the fraction of unabsorbed AGNs *increases* with luminosity; (2) the fraction of Compton-thin sources *decreases* with luminosity; and (3) the fraction of Compton-thick objects remains roughly *constant* with luminosity.

The observation that unobscured sources dominate the high- $L$  end of the AGN LF is often interpreted as evidence for the so-called “receding torus model” (e.g., Lawrence 1991; Simpson 2005). In this model, the covering factor of the dusty torus, which obscures the nuclear region, decreases with increasing AGN luminosity—a trend that is observed in many

(X-ray) AGN samples and surveys (e.g., Lawrence & Elvis 1982; Steffen et al. 2003; Barger et al. 2005; Simpson 2005; Hasinger et al. 2005; La Franca et al. 2005; Treister & Urry 2006; Maiolino et al. 2007; Brusa et al. 2010; Burlon et al. 2011). As the opening angle increases, the probability of detecting an obscured source decreases. Some studies have suggested that unobscured AGNs with higher bolometric luminosities may have less (dusty) torus material, based on the mid-IR to bolometric ratio, again supporting the receding torus model (e.g., Treister et al. 2008). Some alternative explanations have also been suggested. For example, Akylas & Georgantopoulos (2008) showed that the photoionization of the obscuring screen around AGNs roughly reproduces the relationship between the fraction of obscured AGNs and X-ray luminosity, as observed by XMM-Newton and Chandra. Hönig & Beckert (2007) suggested that the Eddington limit on a clumpy torus may also cause the obscured fraction to decrease with luminosity. It is important to note that the apparent decrease in the fraction of obscured AGNs at high luminosities could be partially due to selection effects, as suggested by, e.g., Treister & Urry (2006)—further emphasizing the need for large, highly complete samples, drawn from homogeneous input catalogs (such as BASS).

Many of these studies have often made the (pragmatic) assumption that Compton-thin AGNs trace *all* obscured objects (e.g., Ueda et al. 2014; see also Hickox & Alexander 2018). Specifically, several analyses of AGN LFs have assumed that the abundance of AGNs stays constant throughout the  $\log(N_{\text{H}}/\text{cm}^{-2}) = 24 - 26$  regime, thus predicting significant space densities of  $\log(N_{\text{H}}/\text{cm}^{-2}) > 25$  AGNs (e.g., Ueda et al. 2014; Aird et al. 2015; Buchner et al. 2015; Ananna et al. 2019). In contrast, only a handful of objects (three) with  $\log(N_{\text{H}}/\text{cm}^{-2}) \geq 25$  are observed in the (70 month) all-sky Swift/BAT survey, conducted in the ultra-hard 14–195 keV band (Ricci et al. 2015, 2017b). To see how our BASS-based results relate to this issue, we consider the Ananna et al. (2019) XLF, which suggests that Compton-thick AGNs would comprise  $\approx 50\%$  of all AGNs in the local universe. If we apply the appropriate BAT flux limits to that XLF (i.e., the 70 month survey), and limit the XLF to  $\log(N_{\text{H}}/\text{cm}^{-2}) < 25$ , we find that  $< 10\%$  of the *observable* sample would in fact be Compton-thick, which is consistent with the results shown in Figure 7. We also note that the Ricci et al. (2015) study, from which the intrinsic  $N_{\text{H}}$  distribution shown in Figure 5 was derived, also presents the *observed*  $N_{\text{H}}$  distribution of the Swift/BAT AGN sample used in that study (their Figure 4, bottom panel). The observed Compton-thick fraction in that study is  $\lesssim 10\%$ , again consistent with the result we show in Figure 7 here (note that the Ricci et al. (2015) analysis also includes AGNs at  $z < 0.01$ ).

As the attenuation curve in Figure 4 shows, the observed luminosity of an object with  $\log(N_{\text{H}}/\text{cm}^{-2}) \geq 25$  is  $\leq 5\%$  of its intrinsic luminosity in the 14–195 keV band, therefore we have to probe very faint fluxes to be able to detect such heavily obscured AGNs. Vito et al. (2018), Yan et al. (2019), and Carroll et al. (2021) find evidence for IR-selected luminous AGNs that completely lack X-ray detection, even in the NuSTAR 3–79 keV band.<sup>29</sup> It is therefore possible that even

high-energy X-ray observations, such as the Swift/BAT survey, do not individually identify the most obscured Compton-thick objects, and thus the fractions reported here for the high- $N_{\text{H}}$  subsample should be treated with some caution.

Considering the physical driver for the trends linking (Compton-thin) obscuration and accretion power, our results in Figure 7 seem at face value to be consistent with the receding torus scenario. However, note that there is no clear drop in the (relative) space densities of Compton-thick AGNs with increasingly high luminosities (i.e., there is no downward trend in the bottom right panel of Figure 7). Indeed, the small sample size and the correspondingly large errors mean we cannot robustly rule out the possibility that the luminosity dependence of the Compton-thick space densities is consistent with that of Compton-thin sources. With this caveat in mind, if the Compton-thick fraction indeed remains (roughly) constant with luminosity, it may lead to some important insights regarding the distribution of circumnuclear matter in AGNs.

Fabian et al. (2006, 2008) and Fabian et al. (2009) suggested that the radiation pressure exerted on the dusty torus gas is crucial for understanding the links between AGN accretion power and obscuration. This was corroborated by the BASS/DR1-based study by Ricci et al. (2017b), which tied radiation pressure, gravity, and orientation angle together, and suggested an explanation for the relation between the fraction of obscured sources and luminosity. In this scenario, the fraction of obscured (Compton-thin) sources fundamentally depends on the Eddington ratio, which dictates the effective radiation pressure on the dusty torus gas. As the luminosity exceeds the effective Eddington limit for the dusty gas, the torus material is pushed away from the central engines, thus significantly decreasing the abundance of high- $\lambda_{\text{E}}$ , high- $N_{\text{H}}$  sources. The observed luminosity dependence is then simply a consequence of the  $\lambda_{\text{E}}$  dependence, dictated by the (limited) range of  $M_{\text{BH}}$  probed in AGN surveys. Most importantly, Ricci et al. (2017b) showed that the fraction of Compton-thick AGNs is independent of luminosity, indicating that these clouds are apparently unaffected by radiation pressure, or that the effective  $\lambda_{\text{E}}$  threshold for Compton-thick clouds is too high and is seldom exceeded.<sup>30</sup>

Our results provide further support for this radiation pressure-driven scenario. The ERDFs we constructed for Type 1 and Type 2 AGNs (Figure 8) clearly show that obscured AGNs (Type 2 sources) are indeed increasingly rare beyond  $\log \lambda_{\text{E}}^* \simeq -1.7$ , which is remarkably consistent with the effective Eddington limit for dusty gas [ $\log \lambda_{\text{E}} \approx -1.7$  for  $\log(N_{\text{H}}/\text{cm}^{-2}) = 22$ ; see Ricci et al. (2017b) and references therein]. The downturn in the space densities of unobscured (Type 1) AGNs occur at higher accretion rates,  $\log \lambda_{\text{E}}^* = -1.152^{+0.089}_{-0.053}$ , and may instead be linked to the physics of accretion disks and/or the (circumnuclear-scale) fueling mechanisms. We therefore propose that the much higher space densities of unobscured AGNs (relative to obscured AGNs) at high  $\lambda_{\text{E}}$  could be naturally explained through the effect of radiation pressure on the dusty obscuring material.

Indeed, looking more closely at the different shapes of the ERDFs for Type 1 and Type 2 AGNs, another line of interpretation suggests itself, relating small-scale physics to large-scale population statistics. First, high accretion rates (i.e.,

<sup>29</sup> Carroll et al. (2021) showed that X-ray emission from these sources can be determined via stacking analysis of Chandra data, indicating that these objects do emit X-rays. It is possible that the heavy obscuration around them extinguishes most of it.

<sup>30</sup> The  $N_{\text{H}}$  dependence of this threshold value is shown in Figure 3 of Ricci et al. (2017b).



high  $\lambda_E$ ) can be triggered by major galaxy mergers, and theoretical models (e.g., Hopkins et al. 2006a, 2006b; Blecha et al. 2018) and observations (Treister et al. 2012; Glikman et al. 2012; Banerji et al. 2015; Glikman et al. 2015; Ricci et al. 2017c; Glikman et al. 2018; Koss et al. 2018; Banerji et al. 2021) suggest that luminous, merger-triggered AGNs start from a highly obscured state (i.e., Type 2), but eventually blow away the obscuring material to become unobscured AGNs (i.e., Type 1). The ratio of Type 2 to Type 1 AGN number densities at high  $\lambda_E$  could therefore reflect the ratio of the short duration of the obscured phase to a much longer, unobscured phase. In contrast, at low  $\lambda_E$ , where accretion is less violent or disruptive, the ratio of Type 2 to Type 1 AGNs likely reflects the geometry of circumnuclear obscuration, as in the traditional unification scheme that is well established locally (Barthel 1989; Antonucci 1993; Urry & Padovani 1995). At intermediate  $\lambda_E$ , a transition occurs, where a mix of AGN types coexist, and where the break in the ERDF of Type 2 AGNs likely reflects the onset of significant radiative feedback, as explained above. If the picture of obscured AGNs transitioning into unobscured AGNs during a merger-driven accretion episode is correct, then we would expect that, at higher redshifts, more high- $\lambda_E$  obscured AGNs would be transitioning into unobscured AGNs, since both merger rates and gas fractions generally increase with redshift. Therefore, we predict that the break in the Type 2 AGN ERDF at higher redshift should occur at higher  $\lambda_E$  (e.g., Jun et al. 2021). Quantitative exploration of these ideas will be deferred to a future work.

We caution that our sample still has relatively few high-luminosity obscured sources. Still, the very existence of such sources indicates that the receding torus scenario is at the very least incomplete (see also Bär et al. 2019), and our extensive bias corrections suggest that the dearth of high- $\lambda_E$  obscured AGNs is real, and cannot be easily explained by obvious observational biases.

## 5.2. Comparison of the Intrinsic BHMF and ERDF to Previous Studies

In Figure 8, the similarity in shape of the BHMFs for Type 1 and Type 2 AGNs, and the difference in the shape of the ERDFs, could potentially imply that the observed difference between the two populations is mainly due to the different distributions in the Eddington ratio. It could also highlight the possibility of a fundamental difference between the two AGN populations. As explained in the preceding section, this difference may be related to AGN fueling mechanisms, including galaxy mergers and large-scale environments (e.g., as seen in the BASS-based clustering analysis of Powell et al. 2018); to smaller-scale feedback mechanisms, including the radiation-regulated unification scheme (as supported by the BASS/DR1-based analysis of Ricci et al. 2017b); or perhaps to some other mechanisms. In any case, any comparison of our results to other studies should take into account these differences between Type 1 and Type 2 AGNs.

In Figure 11, we compare the BHMFs and ERDFs for BASS Type 1 and Type 2 AGNs with other BHMFs and ERDFs reported in the literature. We compare our BHMF for the Type 1 AGN subsample to the  $1/V_{\max}$ -based BHMF of the local broad-line SDSS AGNs derived by Greene & Ho (2007) and Greene & Ho (2009). We find that the BASS observed space densities are higher, by  $\geq 0.5$  dex, in the range  $\log(M_{\text{BH}}/M_{\odot}) > 7.0$ , which may have been caused by

differences in the selection method. We note that the Greene & Ho (2007) and Greene & Ho (2009) studies focused on a broad (optical) selection function, which included host-dominated continuum sources with broad  $H\alpha$  lines, and not just quasar-like AGNs. Our higher space densities thus indicate that the ultra-hard X-ray selection of AGNs provides larger, likely more complete samples even of (high-luminosity) broad-line AGNs, compared to SDSS. Some of this discrepancy may be related to the *bright* flux limit imposed as part of the SDSS spectroscopy ( $i > 15$  mag), which BASS does not impose. Specifically, the fact that our  $1/V_{\max}$  space densities extend to higher masses implies that the X-ray selection is probing a different  $M_{\text{BH}}$  (and possibly  $\lambda_E$ ) range.

SW10 assumed a modified Schechter function-shaped BHMf and a Schechter function-shaped ERDF, evaluated over essentially the same redshift interval as the present work ( $z < 0.3$ ). While SW10 does correct for incompleteness at the low- $M_{\text{BH}}/\lambda_E$  range, unlike the  $1/V_{\max}$  method, it does not account for measurement uncertainty. For the BHMf, SW10 report the following best-fitting parameters:  $\log(M_{\text{BH}}^*/M_{\odot}) = 8.11$ ,  $\log(\Phi^*/h^3 \text{ Mpc}^{-3}) = -5.10$ ,  $\alpha = -2.11$ , and  $\beta = 0.5$ . The  $1/V_{\max}$  values of the BHMf of SW10 are  $\simeq 0.5$  dex lower at  $\log(M_{\text{BH}}/M_{\odot}) \leq 9$  than this work. These differences in  $1/V_{\max}$  between SW10 and this work are also reflected in the discrepancy between the intrinsic BHMf, particularly at intermediate masses. As both SW10 and the present work focus on the same redshift regime, the differences between the two observed populations likely arise from the distinct selections by the optical and ultra-hard X-ray bands.

The differences in the two samples become clearer when we look at the ERDF. There is a noticeable discrepancy between SW10 and our Type 1 results—in both the observed data points and the intrinsic functions. Again, the discrepancy in the observed samples might be due to the different selection methods. Optical surveys are more likely to be biased toward high-luminosity AGNs, because in order for an object to be identified as an AGN, it has to dominate over host galaxy emission. Therefore, this sample would be skewed toward high luminosity (and  $\lambda_E$ ). Additionally, our sample of Type 1 AGNs covers all objects with broad  $H\alpha$  lines, including intermediate types (such as 1.5 and 1.9). These intermediate types tend to be somewhat obscured, even in the Compton-thin regime, which means that if the radiation-regulated unification model is indeed the dominant mechanism, a sample of luminous quasars (such as that of SW10) would be skewed toward higher  $\lambda_E$ , compared to the more complete BASS sample. As the SW10 study does not account for measurement uncertainty, that could also lead to part of the discrepancy.

S15 presented the BHMf and ERDF for Type 1 AGNs as being in the redshift range  $1 < z < 2$ . Additionally, S15 predicted the BHMf and ERDF of Type 2 AGNs as being in the same redshift range, by using a luminosity-dependent obscured fraction function (from Merloni et al. 2014). By comparing our local BASS results with the  $1 < z < 2$  S15 results, it appears that, at higher redshifts, there are more high-mass AGNs of both types, whereas in the local universe the lower-mass AGNs become more abundant. This suggests that many high-mass SMBHs have become inactive between  $1 \lesssim z \lesssim 2$  and  $z \lesssim 0.3$ , or that the average accretion rate has decreased over time (e.g., due to fewer mergers or because interstellar gas has been depleted). The S15 Type 1 AGN ERDF agrees well with our Type 1 ERDF, while both the

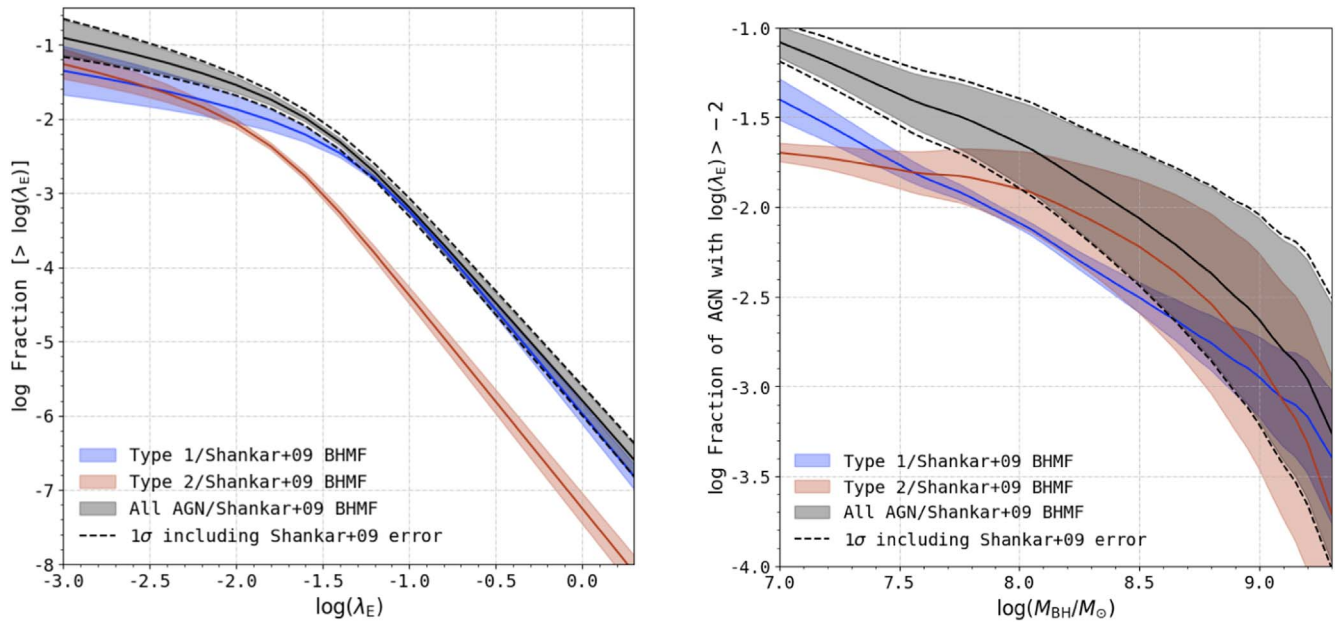


**Figure 13.** Left panel: the fraction of AGNs that lie above  $\log \lambda_E$ , according to our model, relative to the total number of SMBHs (from Shankar et al. 2009). Right panel: the fraction of AGNs that lie above  $\log \lambda_E > -2$  as a function of mass. We divide our best-fit Type 1 (the blue line and shaded region), Type 2 (the red line and shaded region), and overall (the black line and shaded region) functions by the local total BHMf (including inactive SMBHs) from Shankar et al. (2009). For both panels, for the overall curve (black), the shaded regions illustrate the uncertainty due to errors in our ERDFs and BHMf, while the black dashed lines also include the uncertainty due to the ranges in the total BHMf, as shown in Figure 7 of Shankar et al. (2009). For the curves for Type 1 and Type 2 AGNs only (blue and red), the shaded regions show the errors in ERDFs and BHMf, for ease of comparison between the two types. The total SMBH mass density according to Shankar et al. (2009) is  $\approx (3 - 5) \times 10^{-5} M_\odot h^3 \text{Mpc}^{-3}$ , while the *active* SMBH mass density according to our analysis is  $3.58^{+0.41}_{-0.23} \times 10^{-4} M_\odot h^3 \text{Mpc}^{-3}$  (i.e., 6%–10% of the total mass density).

normalization and the shape of the S15 Type2 ERDF are significantly different from our Type 2 results. Specifically, the shapes of the two S15 ERDFs are consistent with each other, whereas the shapes of our Type 1 and Type 2 ERDFs are significantly different. Note that the predicted S15 Type 2 estimates are based on several assumptions. As suggested in Merloni et al. (2014), even though the obscuration fraction is reported as redshift-independent, some redshift dependence is still seen at high luminosities. Additionally, Merloni et al. (2014) reported some issues that could lead to incorrect estimations of intrinsic luminosities (i.e., due to incorrect assumptions about the complex geometry of the obscurer). As this fraction is constrained using  $\leq 10$  keV data, these uncertainties could be significant, due to the degeneracy of AGN spectral parameters (Gilli et al. 2007; Ricci et al. 2017a; Ananna et al. 2020a). If the  $z \simeq 1 - 2$  ERDF represents the underlying Type 2 population at that redshift, it would imply that AGN activity has decreased over time. The overall normalizations of the BHMf at  $1 < z < 2$  are also higher than the BHMf of the local universe, which supports the decreased activity scenario.

### 5.3. AGN Duty Cycle

A highly useful observational constraint on theoretical models of SMBH evolution is the AGN duty cycle—that is, the fraction of all SMBHs (including inactive SMBHs) that are actively accreting, above a certain Eddington ratio (and at any given cosmic epoch). The AGN duty cycle has been addressed by numerous observational and theoretical studies. Some hydrodynamical galaxy simulations have tried to quantify the AGN duty cycle by tracing the gas inflow onto the central SMBHs. Novak et al. (2011) simulated a single galaxy and

found that the SMBH accretes at  $\log \lambda_E > -3$  for  $\lesssim 30\%$  of the time span (12 Gyr) covered by the simulation. Angles-Alcazar et al. (2021) recently reported a duty cycle of  $\sim 0.25$  at  $z < 1.1$ . Phenomenological AGN population models can constrain and/or deduce the AGN duty cycle by linking the observed (redshift-resolved) AGN LF with the local (active and inactive) BHMf, or indeed the (integrated) BH mass density, generally following the Soltan (1982) argument (e.g., Cavaliere & Padovani 1989; Marconi et al. 2004; Shankar et al. 2009). For example, Shankar et al. (2009) found that, in the local universe, less than 1% of all SMBHs should be considered as active (i.e., accreting at the fiducial accretion rate of their model; see their Figure 7). The active fraction or duty cycle is often defined as a ratio of LF to mass function, independent of Eddington ratio. Both simulations and population synthesis studies typically have to assume an AGN radiative efficiency (Shankar et al. 2009), and often also have to assume an ERDF, or even a universal  $\lambda_E$  (e.g., Shankar et al. 2013; Weigel et al. 2017).

Highly complete AGN surveys naturally provide the observational benchmark for the AGN duty cycle. For example, Goulding et al. (2010) reported an active fraction of  $\approx 0.27$ , based on a volume-limited, mid-IR-selected sample of  $D < 15$  Mpc galaxies—although their definition of “active” includes AGNs with Eddington ratios as low as  $\log \lambda_E \geq -5$ .

There are theoretical, phenomenological, and observational lines of argument for the AGN duty cycle to depend on galaxy and/or BH mass, and perhaps on other properties as well (e.g., galaxy environment and/or clustering; Haiman & Hui 2001; Martini & Weinberg 2001; Shen et al. 2007; White et al. 2008; Shen et al. 2009; Shankar et al. 2010b, 2010a). In Figure 13, we show the AGN duty cycle in the local universe, based on our BASS/DR2 AGN sample. In the left panel of Figure 13, we show the  $\lambda_E$ -dependent duty cycle, expressed as the

cumulative probability of having  $\log \lambda_E$  greater than a given value,  $P(>\log \lambda_E)$ . We calculate this probability by integrating over all BH mass bins and  $\log \lambda_E$  bins above a given value, then dividing by the integrated total local BHMF (i.e., including inactive SMBHs), taken from Shankar et al. (2009). The Shankar et al. (2009) BHMF was compiled by taking into account the dispersions in all the local SMBHs that were available at the time (e.g., McLure & Dunlop 2002; Marconi & Hunt 2003; Tundo et al. 2007). As discussed in Section 2.2, Shankar et al. (2020) report a BHMF  $\sim 4$  lower than the Shankar et al. (2009) BHMF (in terms of space densities at all masses), as the later study uses a recalibrated  $M$ - $\sigma$  relationship. As Koss et al. (2022c) use the canonical Kormendy & Ho (2013) prescription to estimate the masses for BASS/DR2 objects, we compare our results to the Shankar et al. (2009) BHMF in Figure 13.

The  $M_{\text{BH}}$ -integrated AGN duty cycles for the entire BASS/DR2 sample relative to the Shankar et al. (2009) BHMFs at  $\log \lambda_E = -2, -1$ , and  $0$  are about  $P(\log \lambda_E > -2) \simeq 2.85 \times 10^{-2}$ ,  $P(\log \lambda_E > -1) \simeq 6.45 \times 10^{-4}$ , and  $P(\log \lambda_E > 0) \simeq 1.61 \times 10^{-6}$ , respectively. At the lowest- $\lambda_E$  threshold that is reasonable for radiatively efficient SMBH accretion, we obtain  $P(\log \lambda_E > -3) \simeq 0.1$ – $0.16$ . According to the Shankar et al. (2009) SMBH mass function, the total mass density of all SMBHs in the local universe is  $\approx (3 - 5) \times 10^{-5} M_{\odot} h^3 \text{Mpc}^{-3}$ , while the *active* SMBH mass density is  $3.58_{-0.23}^{+0.41} \times 10^{-4} M_{\odot} h^3 \text{Mpc}^{-3}$  (i.e., 6%–10% of the total SMBH mass density).

Considering the Type 1 and Type 2 AGNs in our samples, their duty cycles are essentially identical at the fiducial threshold corresponding to  $P(\log \lambda_E \simeq -2.5)$ . For lower-threshold Eddington ratios ( $\log \lambda_E < -2.5$ ), the cumulative duty cycle is slightly higher for Type 2 sources than it is for Type 1 sources (but within the  $1\sigma$  error budget), while for higher-threshold  $\lambda_E$ , the duty cycle of Type 1 AGNs is significantly higher. This means that a lower fraction of obscured AGNs have such high  $\lambda_E$ , which is not surprising given the differences between the Type 1 and Type 2 ERDFs (Figure 8).

The right panel of Figure 13 shows the fraction of active SMBHs (AGNs) with  $\log \lambda_E > -2$  among the total SMBH population (including inactive BHs), as a function of  $M_{\text{BH}}$ . The general trend for all BASS AGNs is that the AGN fraction decreases with increasing  $M_{\text{BH}}$ . This general trend is in agreement with what was found in several previous studies, including both direct observations (e.g., Greene & Ho 2007; Goulding et al. 2010) and population models (e.g., Marconi et al. 2004; Shankar et al. 2009, 2013). Our AGN fraction (10%–16%) is about an order of magnitude above what was found by Shankar et al. (2009) using their fiducial model ( $< 1\%$  active), which assumes a constant radiative efficiency of 0.065. Our results are in slightly better agreement with the redshift-dependent Eddington ratio model from the Shankar et al. (2009) study. This demonstrates the importance of independent, observational determinations of the AGN ERDFs, fractions, and duty cycles to (phenomenological) models of the cosmic evolution of SMBHs. We note that these trends may evolve with redshift.

Among the more nuanced trends in the right panel of Figure 13, we note that at lower masses,  $\log(M_{\text{BH}}/M_{\odot}) < 9$ , the fraction of Type 2 AGNs with  $\log \lambda_E > -2$  is higher than that of Type 1 AGNs. This is driven by the fact that the space density of Type 2 AGNs is higher than that of Type 1 AGNs at

$\log \lambda_E < -1.7$ , as shown in Figure 8. This trend flips completely if the threshold is moved to  $\log \lambda_E \geq -1$  (not shown in the figure), and Type 1 AGNs dominate the fraction of AGNs at all mass bins.

Assuming that the trends found here hold for other surveys (and out to higher redshifts), they highlight why different survey strategies may lead to ambiguous or contradictory conclusions about the obscured AGN fraction. Specifically, wide-field surveys that pick up the rarest, highest- $M_{\text{BH}}$  systems are expected to be biased toward unobscured systems; conversely, deeper (and narrower) surveys that uncover the more abundant lower- $M_{\text{BH}}$  population may be (mildly) biased toward obscured AGNs. Mateos et al. (2017) reported that by studying the torus structure and covering factor of X-ray-selected samples (at  $< 10$  keV), they find that a significant population of obscured objects should exist at high luminosities, and are missed by X-ray surveys. These heavily obscured high-luminosity AGNs have been identified in recent studies using IR, optical, and X-ray data (e.g., Yan et al. 2019; Carroll et al. 2021). Treister et al. (2010) also reached similar conclusions by analyzing IR-selected sources. As discussed in Section 5.1, and as implied by Figure 4 and these results, given Swift/BAT’s current flux limits, many heavily obscured (i.e.,  $\log[N_{\text{H}}/\text{cm}^{-2}] > 25$ ), massive AGNs may still be undetected by BAT.

#### 5.4. Comparison between the Galaxy Stellar Mass Function and Active Black Hole Mass Function

We finally use the BHMF we derive from the BASS/DR2 data to speculate about the BH to stellar mass ratio. The local universe provides ample evidence for a close relation between the mass of SMBHs and the stellar mass of their host galaxies (particularly their bulge components). The ratio of SMBHs to stellar mass lies in the range  $-3.55 < \log(M_{\text{BH}}/M_{\text{gal}}) < -2.31$  (e.g., Marconi & Hunt 2003; Häring & Rix 2004; Sani et al. 2011; Kormendy & Ho 2013; Marleau et al. 2013; McConnell & Ma 2013; Reines & Volonteri 2015, and references therein). If SMBH masses scale (roughly) linearly with host galaxy masses, then the corresponding mass functions should have similar shapes, with a horizontal shift that scales as  $M_{\text{BH}}/M_{\text{gal}}$ .<sup>31</sup> We explore the  $M_{\text{BH}} - M_{\text{gal}}$  scaling relationship by comparing the break in our BHMF ( $M_{\text{BH}}^*$ ) with the break in the galaxy stellar mass function ( $M_{\text{gal}}^*$ ).

Some recent determinations of the galaxy stellar mass function, based on large optical low-redshift surveys, find breaks at  $10.5 \lesssim \log(M_{\text{gal}}^*/M_{\odot}) \lesssim 10.7$  (e.g., MacLeod et al. 2010; Baldry et al. 2012; Weigel et al. 2016), with relatively limited variance between different galaxy types (see the discussion in, e.g., Moffett et al. 2016; Davidzon et al. 2017, and references therein). Comparing these galaxy stellar mass function breaks directly with the BHMF break we find for all BASS/DR2 AGNs [ $\log(M_{\text{BH}}^*/M_{\odot}) = 7.88_{-0.22}^{+0.21}$ ], we get  $-2.82 \lesssim \log(M_{\text{BH}}^*/M_{\text{gal}}^*) \lesssim -2.62$ . This agrees well with the range of  $\log(M_{\text{BH}}^*/M_{\text{gal}}^*)$  derived from direct measurements in individual systems.

We caution that these results are highly speculative, as they inherently link the *active* BHMF (i.e., the BHMF of AGNs) to a quantity of stellar mass functions that are dominated by

<sup>31</sup> The vertical shift would scale with SMBH occupation fraction and AGN duty cycle.

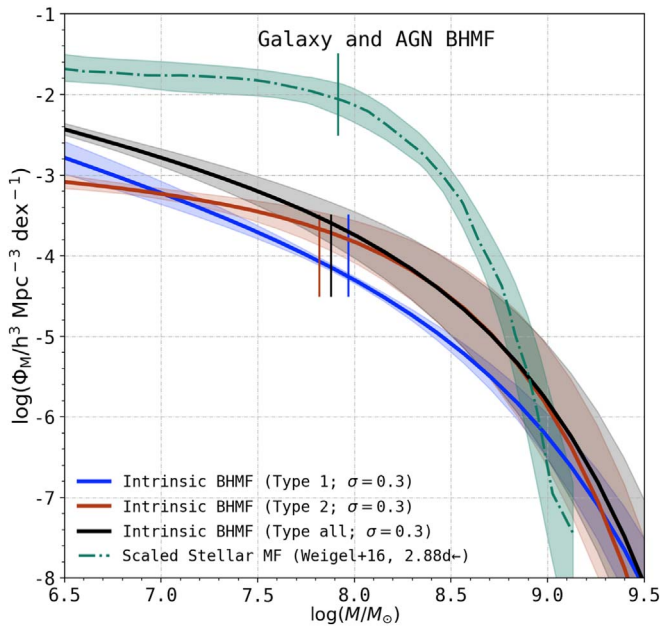


**Figure 14.** The BASS/DR2 BHMf: Type 1 (the blue solid line), Type 2 (the red solid line), and all AGNs (the black solid line), compared to the Weigel et al. (2016) galaxy stellar mass function (the green dashed–dotted line), shifted left in mass by 2.88 dex to line up the breaks in galaxy Schechter function (the green vertical line) and the modified Schechter function for all AGNs (the black vertical line). The dispersion in the galaxy stellar mass function also includes the galaxy stellar mass functions of Peng et al. (2010), Baldry et al. (2012), and Taylor et al. (2015). All shaded regions show  $\pm 1\sigma$  errors for each function.

inactive galaxies, thus assuming that the BASS-based  $M_{\text{BH}}^*$  is representative of all SMBHs and/or that BASS AGN hosts are indistinguishable from the general galaxy population. The actual analysis of BASS AGN hosts and the measurement of their stellar masses is beyond the scope of this work, but is expected to be pursued in a future BASS study.

Figure 14 shows the galaxy mass function (shifted left by 2.88 dex, for ease of comparison in the figure) and the AGN BHMf for our overall sample, as well as for the Type 1 and Type 2 subsamples. In this figure, we use a modified Schechter function to represent the AGN samples, and a double Schechter function to represent the galaxy stellar mass function (e.g., Weigel et al. 2016, 2017). The shape of the galaxy stellar mass function may differ from the BH mass functions because of the different functional forms used to fit the data. However, this might also mean that the ratio of BH to galaxy mass, or even bulge to galaxy mass, varies with galaxy mass (e.g., Bell et al. 2017). Fitting a modified Schechter function to galaxy stellar masses is beyond the scope of this work, but will also be explored in our future project.

We stress again that these simplistic galaxy–BH scaling relationships provide only a limited view of the relations between (BASS) AGNs and their hosts, as some studies suggest that close SMBH–host links should only be applicable to the (true) bulge or spheroidal components of galaxies and/or to certain types of galaxies (see the detailed discussions in, e.g., Graham et al. 2011 and Kormendy & Ho 2013).

## 6. Summary and Conclusions

We have determined the XLF, the BHMf, and the ERDF for the large and highly complete ultra-hard X-ray-selected sample of BASS/DR2 AGNs, covering the redshift range

$0.01 \leq z \leq 0.3$ . Our comprehensive methodology corrects these distributions for incompleteness at low masses and low Eddington ratios, and also corrects for the overestimation of space densities, due to measurement uncertainty at high masses and high Eddington ratios. We then convolved the bias-corrected BHMf and ERDF to verify that the observed XLF is reproduced self-consistently. We further calculated the XLFs, BHMf, and ERDFs separately for Type 1 and Type 2 AGN. Indeed, thanks to the high sensitivity of Swift/BAT to heavily obscured sources, and the BASS spectroscopic follow-up, we are able to present a highly complete determination of the BHMf and ERDF of Type 2 AGNs.

We then used these key distribution functions to address several questions pertaining to the demographics of low-redshift AGNs.

We summarize our inferences from this work as follows:

1. In the observed BASS/DR2 sample, the fraction of unabsorbed AGNs increases with luminosity, the fraction of Compton-thin AGNs decreases with luminosity, and the fraction of Compton-thick objects stays constant with luminosity<sup>32</sup> (as shown in Figure 7). This result is consistent with the radiation-regulated unification model (proposed by Ricci et al. 2017b).
2. As shown in Figure 8, the shape of the ERDF of Type 1 AGNs is significantly different from that of Type 2 AGNs, as the ERDF of Type 2 AGNs is skewed toward low  $\lambda_E$ . The difference in the break in the ERDFs between the Type 1 sample ( $-1.152^{+0.089}_{-0.053}$ ) and the Type 2 sample ( $-1.657^{+0.087}_{-0.064}$ ) is statistically significant. The increasing rarity of obscured AGNs above  $\lambda_E \approx 0.02$  is remarkably consistent with the radiation-regulated unification model, and may indicate the role of blowout at high  $\lambda_E$ , while geometry and orientation dominate at low  $\lambda_E$ .
3. As shown in Figure 12, we demonstrate that the ERDF maintains its shape independent of BH mass, for two distinct mass regimes (and both Type 1 and Type 2 AGNs).
4. Concerning the AGN duty cycles and mass density fraction, we find that the fraction of Type 2 AGNs is higher than Type 1 AGNs at all masses (for  $\log \lambda_E \geq -2$ ). We find that the active fraction, defined as the fraction of AGNs with  $\log \lambda_E > -3$  relative to the total BHMf (including relic systems), is 10%–16%. In the local universe, the percentage of mass in active SMBHs is 6%–10% of all SMBH mass.

Our extensive analysis opens the door for several potential follow-up investigations. In the future, we will further explore the relationship between obscuring column density and Eddington ratio. With detailed host galaxy measurements for BASS AGNs, we may be able to study the key distribution functions (XLF, BHMf, and ERDF) split by host morphology, star formation state, environment (i.e., merger state), or other properties. Combining our results with higher-redshift samples, we expect that the present analysis of the BASS sample would serve as the low-redshift benchmark for studying the evolving population of accreting SMBHs, as probed by its key distribution functions.

<sup>32</sup> Note that some caution is required in this interpretation, as the error bars for this trend in Compton-thick AGNs are large, due to the small sample size.

We thank the anonymous reviewers for their constructive and detailed comments, which helped us improve the quality of this paper. T.T.A. and R.C.H. acknowledge support from NASA, through ADAP award 80NSSC19K0580. R.C.H. also acknowledges support from the National Science Foundation, through CAREER award 1554584. B.T. acknowledges support from the Israel Science Foundation (grant No. 1849/19) and from the European Research Council (ERC), under the European Union’s Horizon 2020 research and innovation program (grant agreement number 950533). M.K. acknowledges support from NASA, through ADAP award NNH16CT03C. C.M.U. acknowledges support from the National Science Foundation, under grant No. AST-1715512. C.R. acknowledges support from the Fondecyt Iniciacion, grant 11190831. We acknowledge support from ANID-Chile Basal AFB-170002 and FB210003 (E.T., F.E.B.), FONDECYT Regular 1200495 and 1190818 (E.T., F.E.B.), ANID Anillo ACT172033 (E.T.), Millennium Nucleus NCN19\_058 (TITANS; E.T.), and the Millennium Science Initiative Program—ICN12\_009 (F.E.B.). K.O. acknowledges support from the National Research Foundation of Korea (NRF-2020R1C1C1005462). The work of K.I. is supported by the Japan Society for the Promotion of Science (JSPS) KAKENHI (18K13584, 20H01939). J.d.B. acknowledges funding from the European Research Council (ERC), under the European Union’s Horizon 2020 research and innovation program (grant agreement No.726384/Empire). This work was performed in part at the Aspen Center for Physics, which is supported by National Science Foundation grant PHY-1607611.

This research made use of `Astropy` (Astropy Collaboration et al. 2013; Price-Whelan et al. 2018), `Matplotlib` (Hunter 2007), `EMCEE` (Foreman-Mackey et al. 2013), `NumPy` (van der Walt et al. 2011), `Topcat` (Taylor 2005), `XSPEC` and `PYXSPEC` (Arnaud 1996), and `ChainConsumer` (Hinton 2016).

## Appendix A

### Estimating Random Errors for the $1/V_{\max}$ Approach

To estimate the random errors on  $\Phi_L(\log L_X)$ ,  $\Phi_M(\log M_{\text{BH}})$ , and  $\xi(\log \lambda_E)$ , we follow the approach by Weigel et al. (2016; see also Gehrels 1986; Zhu et al. 2009; Gilbank et al. 2010). The upper and lower errors on  $\Phi_L(\log L_X)$  in bin  $j$  are given by:

$$\begin{aligned} \sigma_{j,\text{up}} &= -\Phi_{L,j} + W_{\text{eff},j} \times \kappa_{\text{up}}(N_{\text{eff},j}) \\ \sigma_{j,\text{low}} &= \Phi_{L,j} - W_{\text{eff},j} \times \kappa_{\text{low}}(N_{\text{eff},j}). \end{aligned} \quad (24)$$

$W_{\text{eff}}$  and  $N_{\text{eff}}$  correspond to the effective weight and the number, respectively, and are defined as:

$$\begin{aligned} W_{\text{eff},j} &= \left( \sum_i^{N_{\text{bin}}} \frac{1}{V_{\text{max},i}^2} \right) \times \left( \sum_i^{N_{\text{bin}}} \frac{1}{V_{\text{max},i}} \right)^{-1} \\ N_{\text{eff},j} &= \left( \sum_i^{N_{\text{bin}}} \frac{1}{V_{\text{max},i}} \right) \times (W_{\text{eff},j})^{-1}. \end{aligned} \quad (25)$$

$\kappa_{\text{up}}$  and  $\kappa_{\text{low}}$  represent the functions that allow us to compute the upper and lower limits on the effective number  $N_{\text{eff}}$  (see Gehrels 1986, Equations (7) and (11)). To determine the upper limits on  $\Phi_L(\log L_X)$ , we compute  $V_s$ , the comoving volume for the entire sky between  $z_{\text{min},s}$  and  $z_{\text{max},s}$ . In bins with  $N_{\text{bin}} = 0$ ,

the upper limit on  $\Phi_L(\log L_X)$  is then given by:

$$\sigma_{\text{limit}} = -\frac{1}{V_s} + \frac{1}{V_s} \times \kappa_{\text{up}}(N_{\text{eff}} = 0), \quad (26)$$

with  $\kappa_{\text{up}}(N_{\text{eff}} = 0) = 1.841$  (Gehrels 1986). We compute the random errors on  $\Phi_M(\log M_{\text{BH}})$  and  $\xi(\log \lambda_E)$  accordingly.

## Appendix B

### Fitting the $1/V_{\max}$ $\Phi$ Values

Below, we outline how we find the best-fitting functional form for the XLF. The BHMf and the ERDF are fit accordingly. We fit all three distributions independently.

The errors on  $\log \Phi_L(\log L_X)$  are asymmetric. As we fit the values in log-space, we thus assume that  $\log \Phi_L(\log L_X)$  is distributed log-normally, rather than assuming a normal distribution. Following the method of Weigel et al. (2017), we use an MCMC and the following probability density function for the fitting:

$$p(x, \mu, \sigma) = \frac{1}{x\sigma\sqrt{2\pi}} \times \exp\left(-\frac{(\ln x - \mu)^2}{2\sigma^2}\right). \quad (27)$$

For the XLF, we determine the properties of  $p$ , i.e.,  $\mu$  and  $\sigma$ , in each  $\log L_X$  bin  $j$ . We use the following definitions:

$$\begin{aligned} \bar{x}_j &= \log(\Phi_{L,j}) + a \\ \mu_j &= \ln(\bar{x}_j) \\ \sigma_{j,16} &= \frac{\ln(\bar{x}_j - \bar{\sigma}_{j,\text{low}}) - \mu}{\text{PPF}(0.16)} \\ \sigma_{j,84} &= \frac{\ln(\bar{x}_j + \bar{\sigma}_{j,\text{up}}) - \mu}{\text{PPF}(0.84)} \\ \sigma_j &= \sqrt{\sigma_{j,16}^2 + \sigma_{j,84}^2}. \end{aligned} \quad (28)$$

The constant,  $a$ , ensures that all  $\bar{x}$  values are positive. PPF(0.16) and PPF(0.84) correspond to the value at which the integral over a normal distribution with  $\mu = 0$ ,  $\sigma = 1$  reaches 16% and 84%, respectively. We add  $\sigma_{j,16}$  and  $\sigma_{j,84}$  in quadrature to determine  $\sigma_j$ , since the log-normal distribution only represents an approximation for the distribution of  $\log \Phi_L(\log L_X)$  values.

For each functional XLF form that is proposed by the MCMC, we compute the predicted  $\log \Phi_{L,\text{pred}}$  values in all  $\log L_X$  bins. We then use  $x_j = \log \Phi_{L,\text{pred},j}$  to compute the log-likelihood  $\ln \mathcal{L}$ :

$$\begin{aligned} \mathcal{L} &= \prod_j^{\text{all bins}} p(x_j, \mu_j, \sigma_j) \\ \ln \mathcal{L} &\propto - \sum_j^{\text{all bins}} \ln(x_j + a) - \sum_j^{\text{all bins}} \frac{(\ln(x_j + a) - \mu_j)^2}{2\sigma_j^2}. \end{aligned} \quad (29)$$

The MCMC allows us to maximize  $\ln \mathcal{L}$  and to find the best-fitting parameters for the assumed functional form. To constrain the bright-end slope of the XLF and the corresponding error, we determine the sum of the  $\gamma_1$  and  $\epsilon_L$  chains. We then determine the median  $\gamma_2$  value and its credible intervals from this new chain. We proceed in the same way when fitting the ERDF with a double power law. We do not include upper limits in the fitting procedure.

## Appendix C

### Estimating the Random Error on the BHMF and the ERDF

We estimate the random error on the bias-corrected  $\Phi_M(\log M_{\text{BH}})$  and  $\xi(\log \lambda)$  by using the covariance matrix, which we derive from the MCMC chain. This approach is similar to the method used by Weigel et al. (2016).

We use the MCMC chain after burn-in to derive the covariance matrix  $\Sigma$ . On its main diagonal,  $\Sigma$  contains the variance on the best-fitting  $\Psi$  parameters. We also use the off-diagonal elements, which express the covariance. If we assume a modified Schechter function for the BHMF and a broken power law for the ERDF,  $\Psi$  has six free parameters: the break and the two slopes of the BHMF ( $M_{\text{BH}}^*$ ,  $\alpha$ , and  $\beta$ ), and the break and the two slopes of the ERDF ( $\lambda$ ,  $\delta_1$ , and  $\epsilon_\delta$ ). As discussed above, the normalization of  $\Psi$  is kept constant in the MCMC. The  $1\sigma$  random errors on the BHMF and the ERDF are given by:

$$\begin{aligned} \sigma_{\Phi}^2(\log M_{\text{BH}}) &= \left( \frac{\partial \Phi}{\partial M_{\text{BH}}^*} \right)^2 \Sigma_{MM} \\ &+ \left( \frac{\partial \Phi}{\partial \alpha} \right)^2 \Sigma_{\alpha\alpha} + \left( \frac{\partial \Phi}{\partial \beta} \right)^2 \Sigma_{\beta\beta} \\ &+ 2 \left( \frac{\partial \Phi}{\partial M_{\text{BH}}^*} \right) \left( \frac{\partial \Phi}{\partial \alpha} \right) \Sigma_{M\alpha} + 2 \left( \frac{\partial \Phi}{\partial M_{\text{BH}}^*} \right) \left( \frac{\partial \Phi}{\partial \beta} \right) \\ &\times \Sigma_{M\beta} + 2 \left( \frac{\partial \Phi}{\partial \alpha} \right) \left( \frac{\partial \Phi}{\partial \beta} \right) \Sigma_{\alpha\beta} \end{aligned} \quad (30)$$

$$\begin{aligned} \sigma_{\xi}^2(\log \lambda) &= \left( \frac{\partial \xi}{\partial \log \lambda^*} \right)^2 \Sigma_{\lambda\lambda} + \left( \frac{\partial \xi}{\partial \delta_1} \right)^2 \Sigma_{\delta\delta} + \left( \frac{\partial \xi}{\partial \epsilon_\delta} \right)^2 \Sigma_{\epsilon\epsilon} \\ &+ 2 \left( \frac{\partial \xi}{\partial \log \lambda^*} \right) \left( \frac{\partial \xi}{\partial \delta_1} \right) \Sigma_{\lambda\delta} + 2 \left( \frac{\partial \xi}{\partial \log \lambda^*} \right) \\ &\times \left( \frac{\partial \xi}{\partial \epsilon_\delta} \right) \Sigma_{\lambda\epsilon} + 2 \left( \frac{\partial \xi}{\partial \delta_1} \right) \left( \frac{\partial \xi}{\partial \epsilon_\delta} \right) \Sigma_{\delta\epsilon}. \end{aligned} \quad (31)$$

$\Sigma_{XX}$  and  $\Sigma_{XY}$  correspond to the main and off-diagonal elements of the covariance matrix, respectively. As we assume the ERDF to be mass-independent, we neglect the matrix elements that express the covariance between the BHMF and the ERDF.

## Appendix D

### Testing the Method

We use two sets of parameters to create mock populations, and examine the robustness of our approach to recovering the underlying parameter space by using three different measurement uncertainties for each set of parameters.

To test our approach to correcting for sample truncation and to examine possible biases, we create mock catalogs. We assume the shapes of the BHMF and the ERDF. We randomly draw sources from the assumed distributions and subject them to selection effects. We then use this mock BASS survey as input, follow the steps outlined above, and test whether our method allows us to recover the initial input distributions.

Besides the bias correction, this approach also allows us to test our ability to recover the XLF. The bolometric LF is given

by the convolution of the BHMF and the ERDF (e.g., Weigel et al. 2017). We use Equation (5) and define the bolometric LF in the following way:

$$\begin{aligned} \Phi_L(\log L_{\text{bol}}) &= \int_{\log \lambda_{\text{E,min},s}}^{\log \lambda_{\text{E,max},s}} \Phi_M(\log L_{\text{bol}} \\ &- \log \lambda_{\text{E}} - 38.18) \xi_{\text{norm}}(\log \lambda_{\text{E}}) d \log \lambda_{\text{E}}. \end{aligned} \quad (32)$$

$\xi_{\text{norm}}(\log \lambda_{\text{E}})$  corresponds to the normalized ERDF, given by:

$$\xi_{\text{norm}}(\log \lambda_{\text{E}}) = \frac{\xi(\log \lambda_{\text{E}})}{\int_{\log \lambda_{\text{E,min},s}}^{\log \lambda_{\text{E,max},s}} \xi(\log \lambda_{\text{E}}) d \log \lambda_{\text{E}}}. \quad (33)$$

After applying the bolometric correction (Equation (2)), we are able to compare the XLF that we recover with the  $1/V_{\text{max}}$  method to our prediction.

To create a mock sample, we proceed according to the following steps:

1.  $N_{\text{draw}}$ : to determine the sample size of our mock catalog,  $N_{\text{draw}}$ , we integrate the assumed BHMF from  $\log M_{\text{BH,min},s}$  to  $\log M_{\text{BH,max},s}$ , and multiply this space density with the comoving volume for the entire sky between  $z_{\text{min},s}$  and  $z_{\text{max},s}$ . Note that to increase the sample size, the simulated volume can be increased.
2.  $\log M_{\text{BH}}$ : we construct the cumulative distribution function (CDF) of the assumed BHMF to randomly draw  $\log M_{\text{BH}}$  values. We draw  $N_{\text{draw}}$  values between 0 and 1 from a uniform distribution, and invert the CDF to determine  $\log M_{\text{BH}}$ .
3.  $\log \lambda_{\text{E}}$ : we use the CDF of the assumed ERDF to assign  $N_{\text{draw}}$  Eddington ratio values. By drawing from the CDFs of the BHMF and the ERDF, the information on their assumed normalizations,  $\Phi^*$  and  $\xi^*$ , is lost. Only  $N_{\text{draw}}$  affects the resulting normalizations. As we determine  $N_{\text{draw}}$  by integrating over the BHMF, the assumed  $\xi^*$  is irrelevant. By construction, integrating over the predicted BHMF and ERDF will result in the same space densities.
4.  $z$ : we assign a redshift between  $z_{\text{min},s}$  and  $z_{\text{max},s}$  to each of the  $N_{\text{draw}}$  entries in our mock catalog. We assume that, within the considered redshift range,  $\Phi_M(\log M_{\text{BH}})$  and  $\xi(\log \lambda_{\text{E}})$  remain constant. Following Herbel et al. (2017), we draw  $z$  values from a nonuniform distribution to account for the evolution of the comoving volume with  $z$ .
5.  $\log L_X$ : once we have estimated  $\log M_{\text{BH}}$  and  $\log \lambda_{\text{E}}$ , we are able to compute the bolometric luminosities, according to Equation (5). By assuming a constant bolometric correction, or alternatively following the luminosity-dependent bolometric correction presented in Duras et al. (2020; see Appendix E below), we are able to translate these bolometric luminosities to (ultra-hard) X-ray luminosities  $\log L_X$ . In the latter scenario, we assign a scatter of  $\sigma_{\log L, \text{scatt}} = 0.37$  dex to the intrinsic luminosity (see Duras et al. 2020), to account for the scatter in the bolometric to X-ray luminosity conversion, and calculate a scattered “intrinsic” luminosity  $\log L_{X, \text{scatt}}$ .
6.  $\log N_H$ : for Type 2 AGNs, we draw a sample of  $\log N_H$  with the intrinsic distribution described in Ricci et al. (2015), as described in detail in Section 3.4.2, based on the scattered X-ray luminosity  $\log L_{X, \text{scatt}}$ .

7. Mass estimation uncertainty effects: we add an additional (log-normal) scatter term, with a standard deviation between 0 and 0.5 dex (see Table 1), to the simulated  $\log M_{\text{BH}}$  values, to account for the uncertainties related to determining  $M_{\text{BH}}$  from observations. Note that these uncertainties are in fact dominated by systematic uncertainties inherent to the mass estimation methods. We then recalculate the observed  $\lambda_{\text{E,obs}}$  using the scattered mass and  $\log L_{\text{X,scatt}}$  values. These values are used for computing the unbiased ERDF and BHMF.
8. Selection effects: finally, to create a realistic mock catalog, we expose the simulated sources to selection effects. The flux limit of the BASS survey represents the most prominent bias. Using  $\log L_{\text{X}}$ ,  $z$ , and  $\log N_{\text{H}}$ , we compute the hard X-ray flux of each source in our mock catalog. For each object  $i$ , we randomly draw a value between 0 and 1 from a uniform distribution. If this random value lies below  $\Omega_{\text{sel}}(\log F_{\text{X},i})$ , the source remains in the sample. We eliminate all other sources that, according to the flux-area curve, are too faint to be included in the sample.

In Figures D1 and D2, we show two examples for our random draw test. We assume the following initial BHMF and ERDF parameters: for Mock #1,  $\log(\Phi^*/h^3 \text{Mpc}^{-3}) = -3.16$ ,  $\log(M_{\text{BH}}^*/M_{\odot}) = 8$ ,  $\alpha = -1.6$ ,  $\beta = 0.6$ ,  $\log(\xi^*/h^3 \text{Mpc}^{-3}) = -4.8$ ,  $\log \lambda_{\text{E}}^* = -1$ ,  $\delta_1 = 0.6$ , and  $\epsilon_{\lambda_{\text{E}}} = 2.5$ . For Mock #2,  $\log(\Phi^*/h^3 \text{Mpc}^{-3}) = -3.16$ ,  $\log(M_{\text{BH}}^*/M_{\odot}) = 8.2$ ,  $\alpha = -1.4$ ,  $\beta = 0.7$ ,  $\log(\xi^*/h^3 \text{Mpc}^{-3}) = -4.8$ ,  $\log \lambda_{\text{E}}^* = -1.4$ ,  $\delta_1 = 0.8$ , and  $\epsilon_{\lambda_{\text{E}}} = 2$ . As mentioned above, the normalization of the ERDF ( $\xi^*$ ) cannot be constrained with our random draw

method. By construction, the integral over the ERDF corresponds to the integral over the BHMF. In all panels of the figure, we illustrate the marginalized probability distribution functions and give the recovered, best-fitting, and bias-corrected BHMF and ERDF parameters.

For both mock catalogs, the effect of adding uncertainty is evident at the high-mass end of the BHMF and the high- $\lambda_{\text{E}}$  end of the ERDF: both distributions are steep and objects are scattered into higher  $M_{\text{BH}}$  and  $\lambda_{\text{E}}$  bins as dispersions are increased (left to right in Figures D1 and D2). The figures show that our method allows us to recover the initial input functions for  $\sigma_{\log M_{\text{BH}}}$  and  $\sigma_{\log \lambda_{\text{E}}}$  between 0 and 0.5. In Figure D3, we use a luminosity-dependent bolometric correction from Duras et al. (2020), and assume a scatter in the bolometric correction of  $\sigma_{\log L, \text{scatt}} = 0.37$ . Therefore, the scatter on  $\log \lambda_{\text{E}}$  is  $\sigma_{\log \lambda_{\text{E}}} = \sqrt{\sigma_{\log M_{\text{BH}}}^2 + \sigma_{\log L, \text{scatt}}^2} \simeq 0.37 - 0.62$  in that case. This high value of  $\sigma_{\log L, \text{scatt}}$  (and the resulting  $\sigma_{\log \lambda_{\text{E}}}$ ) is somewhat extreme, but serves to demonstrate the effect of having a large uncertainty in luminosity due to measurement uncertainty and bolometric correction. The  $1/V_{\text{max}}$  values of the XLF are consistent with what we expect from the convolution. For the BHMF and the ERDF, the  $1/V_{\text{max}}$  values are consistent with the assumed input functions at high masses and Eddington ratios. At low- and high- $M_{\text{BH}}$  and  $\lambda_{\text{E}}$  values, the effect of sample truncation is evident. The bias-corrected intrinsic function (shown with the red and blue solid lines) is better at recovering the true underlying function than the  $1/V_{\text{max}}$  data points, and fits at this end as well.

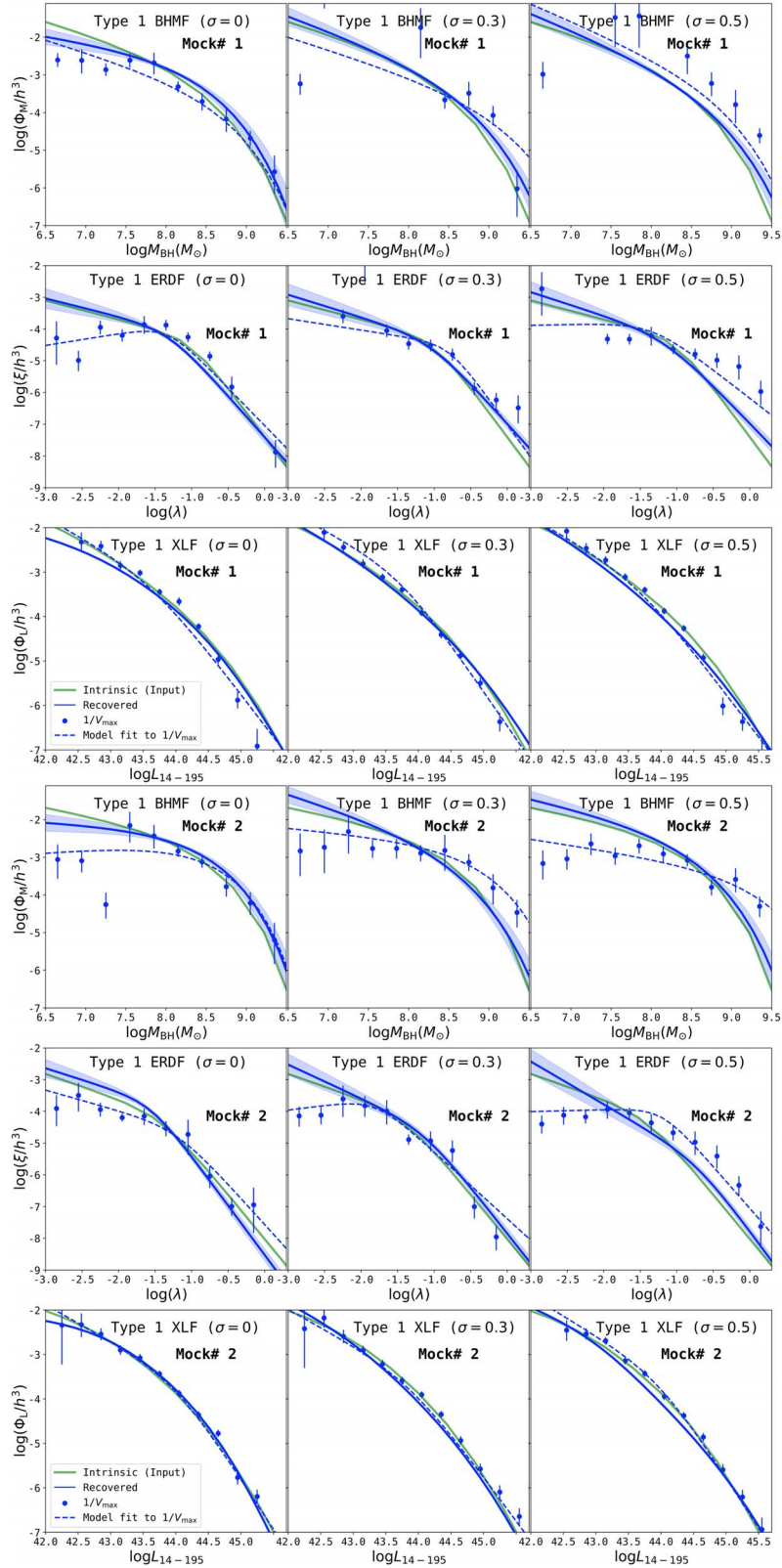


**Figure D1.** Results for Type 1 AGNs for two mock catalogs. For the top three panels (Mock #1), the parameters are fixed at  $\log(\Phi^*/h^3 \text{ Mpc}^{-3}) = -3.16$ ,  $\log(M_{\text{BH}}^*/M_{\odot}) = 8$ ,  $\alpha = -1.6$ ,  $\beta = 0.6$ ,  $\log(\xi^*/h^3 \text{ Mpc}^{-3}) = -4.8$ ,  $\log \lambda_{\text{E}}^* = -1$ ,  $\delta_1 = 0.6$ , and  $\epsilon_{\lambda_{\text{E}}} = 2.5$ . For the bottom three panels (Mock #2), the parameters are fixed at  $\log(\Phi^*/h^3 \text{ Mpc}^{-3}) = -3.16$ ,  $\log(M_{\text{BH}}^*/M_{\odot}) = 8.2$ ,  $\alpha = -1.4$ ,  $\beta = 0.7$ ,  $\log \xi = -4.8$ ,  $\log \lambda_{\text{E}}^* = -1.4$ ,  $\Delta_1 = 0.8$ , and  $\epsilon_{\lambda_{\text{E}}} = 2.0$ . Each column represents a different dispersion in BH mass and Eddington ratio. From left to right,  $\sigma_{\log M_{\text{BH}}}$  and  $\sigma_{\log \lambda_{\text{E}}}$  are increased from 0 to 0.3 to 0.5. For each plot, the green lines show the intrinsic function assumed for the mock catalog, the blue data points show the results from  $1/V_{\text{max}}$ , the blue dashed lines show the MCMC fits to these data points, and the blue solid lines show our attempts to recover the underlying distributions according to the method outlined in Section 3.4. The bias-corrected intrinsic distributions are a much better match to the mock input catalog than the  $1/V_{\text{max}}$  results.



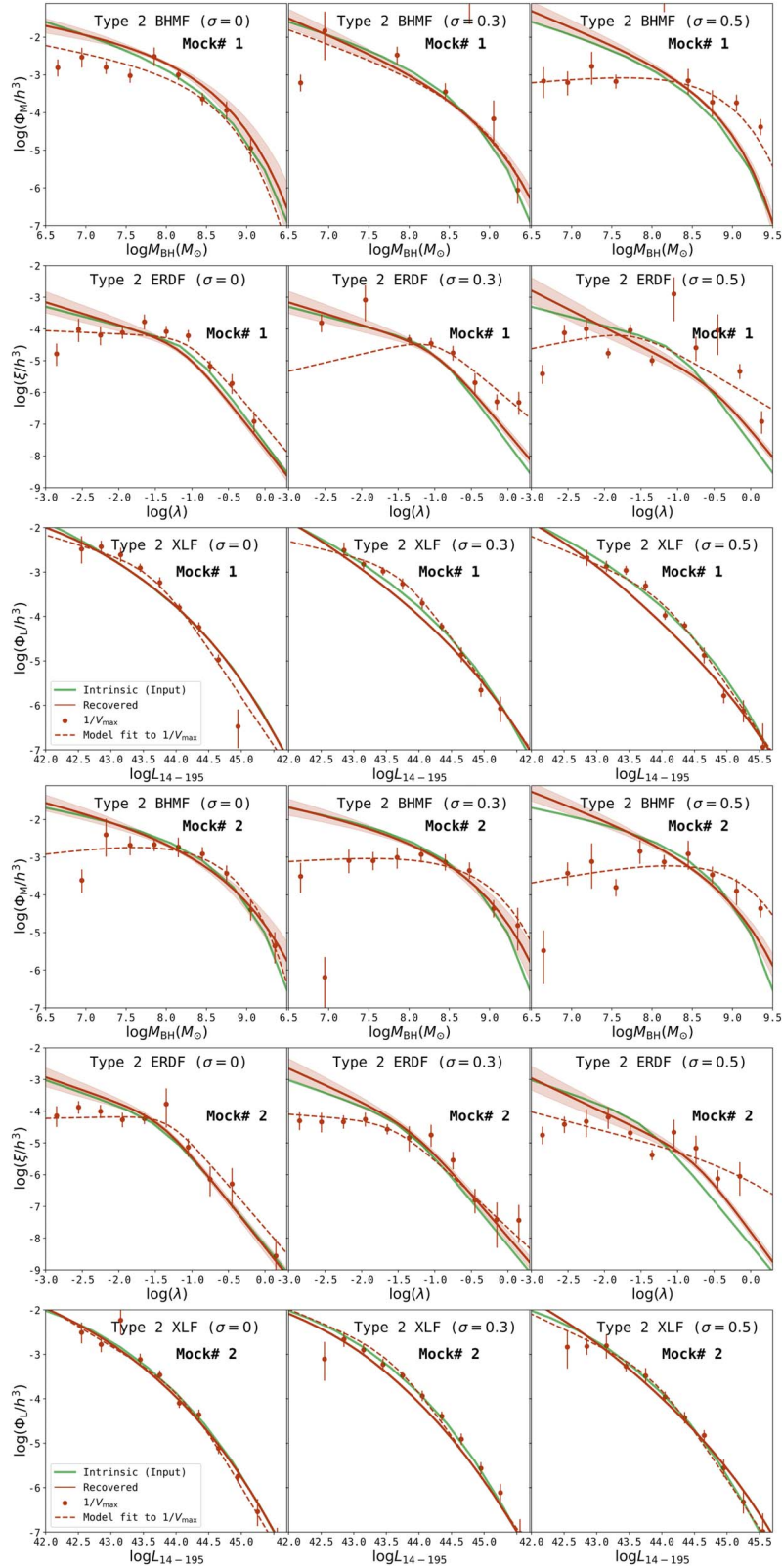


**Figure D2.** Results for Type 2 AGNs for two mock catalogs. For the top three panels (Mock #1), the parameters are fixed at  $\log(\Phi^*/h^3 \text{ Mpc}^{-3}) = -3.16$ ,  $\log(M_{\text{BH}}^*/M_{\odot}) = 8$ ,  $\alpha = -1.6$ ,  $\beta = 0.6$ ,  $\log(\xi^*/h^3 \text{ Mpc}^{-3}) = -4.8$ ,  $\log \lambda_{\text{E}}^* = -1$ ,  $\delta_1 = 0.6$ , and  $\epsilon_{\lambda_{\text{E}}} = 2.5$ . For the bottom three panels (Mock #2), the parameters are fixed at  $\log(\Phi^*/h^3 \text{ Mpc}^{-3}) = -3.16$ ,  $\log(M_{\text{BH}}^*/M_{\odot}) = 8.2$ ,  $\alpha = -1.4$ ,  $\beta = 0.7$ ,  $\log(\xi^*/h^3 \text{ Mpc}^{-3}) = -4.8$ ,  $\log \lambda_{\text{E}}^* = -1.4$ ,  $\delta_1 = 0.8$ , and  $\epsilon_{\lambda_{\text{E}}} = 2$ . Each column represents a different dispersion in BH mass and Eddington ratio. From left to right,  $\sigma_{\log M_{\text{BH}}}$  and  $\sigma_{\log \lambda_{\text{E}}}$  are increased from 0 to 0.3 to 0.5. For each plot, the green lines show the intrinsic function assumed for the mock catalog, the red data points show the results from  $1/V_{\text{max}}$ , the red dashed lines show MCMC fits to these data points, and the red solid lines show our attempts to recover the underlying distributions according to the method outlined in Section 3.4. As in the previous figure, the bias-corrected intrinsic distributions are a much better match to the mock input catalog than the  $1/V_{\text{max}}$  results.

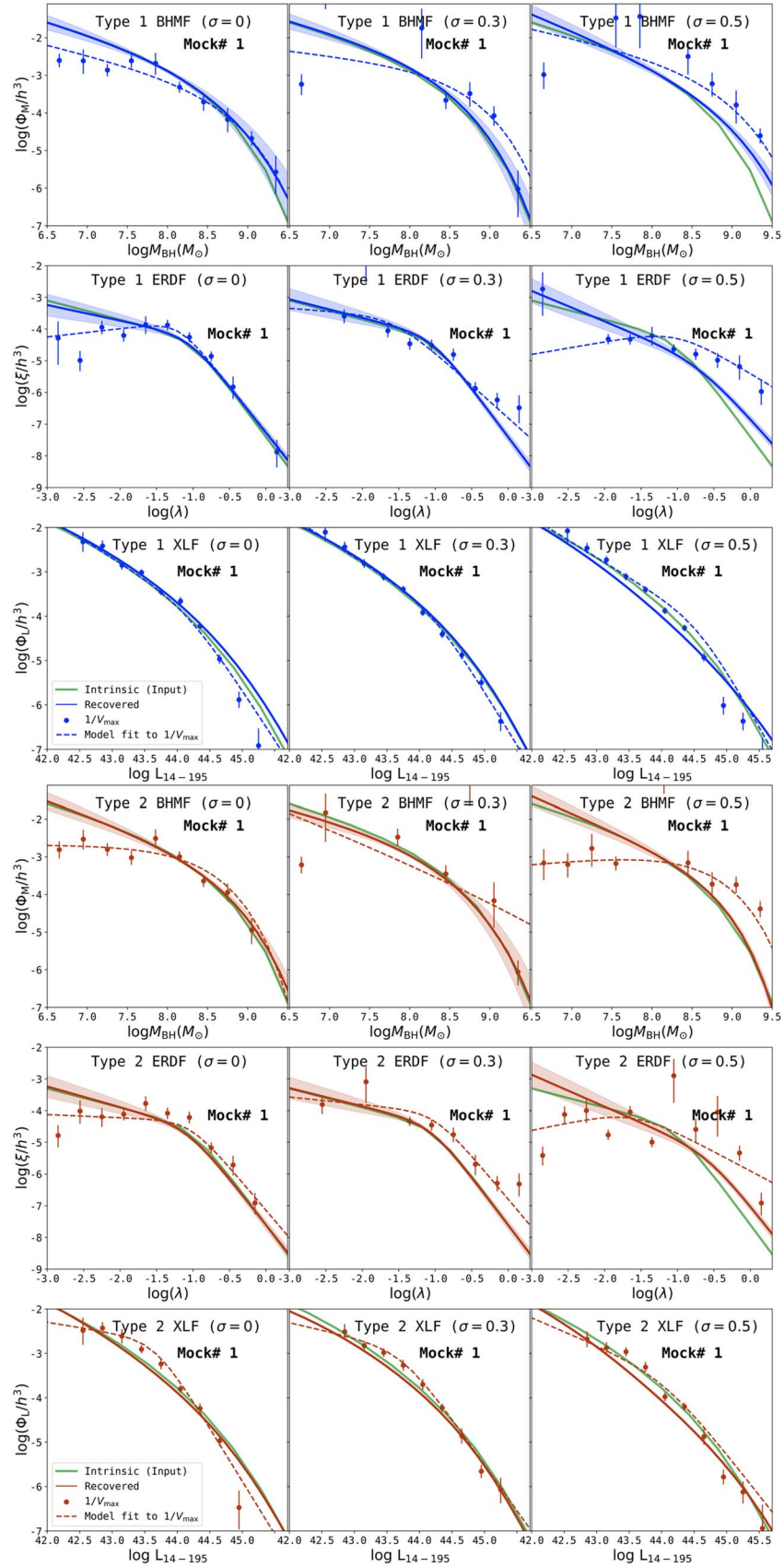


**Figure D3.** Results for Type 1 (top three rows) and Type 2 (bottom three rows) AGNs for mock catalog 1 with luminosity-dependent bolometric correction (Duras et al. 2020). The intrinsic distributions are as described in Figures D1 and D2 for Mock #1. In this case, we also assume that the scattered intrinsic luminosity is scattered by  $\sigma = 0.37$ , and therefore the scatter on  $\lambda_E$  is  $\sigma_{\log \lambda_E} = \sqrt{\sigma_{\log M_{\text{BH}}}^2 + \sigma_{\log L, \text{scatt}}^2}$ . Each panel reports the assumed  $\sigma = \sigma_{\log M_{\text{BH}}} = 0, 0.3, \text{ or } 0.5$ . Even with these assumptions, the bias-corrected intrinsic distributions are a much better match to the mock input catalog than the  $1/V_{\text{max}}$  results.

## Appendix E

### Luminosity-dependent Bolometric Correction

In the main part of the paper, we use Equation (2) to straightforwardly convert between X-ray and bolometric luminosities (and vice versa) during the forward modeling. We also use this conversion to calculate the Eddington ratios of our AGNs from their BH masses and X-ray luminosities. Here, we explore the effects of using, instead, a luminosity-dependent bolometric correction, as supported by several studies (e.g., Marconi et al. 2004; Hopkins et al. 2007; Lusso et al. 2012; Duras et al. 2020, and references therein). Specifically, we choose to use the recently published prescriptions of Duras et al. (2020), which are based on a large sample of AGNs covering a broad range in redshift and luminosity (including the Swift/BAT AGNs at low redshifts).

To convert  $\log L_{\text{bol}}$  to  $\log L_{2-10\text{keV}}$ , we apply a bolometric correction  $\log \kappa_{2-10\text{keV}} \equiv L_{\text{bol}}/L_{2-10\text{keV}}$ , which, following Duras et al. (2020), is derived using the functional form:

$$\kappa_{2-10\text{keV}}(L_{\text{bol}}) = a \left[ 1 + \left( \frac{\log(L_{\text{bol}}/L_{\odot})}{b} \right)^c \right]. \quad (34)$$

Similarly, to convert from  $\log L_{2-10\text{keV}}$  to  $\log L_{\text{bol}}$  (i.e., to calculate  $\lambda_{\text{E}}$ ), we use the functional form:

$$\kappa_{2-10\text{keV}}(L_X) = a \left[ 1 + \left( \frac{\log(L_X/L_{\odot})}{b} \right)^c \right]. \quad (35)$$

For both forms of conversion, the parameters  $a$ ,  $b$ , and  $c$  are taken from Table 1 of Duras et al. (2020). In Equation (34), we use the prescribed variables for each AGN type (i.e., Type 1 and Type 2). As our main analysis relies on the *ultrahard* X-ray luminosities relevant for the BAT survey, we use the conversion from  $\log L_{2-10\text{keV}}$  to  $\log L_{14-195\text{keV}}$ :

$$\log L_{14-195\text{keV}} = \log L_{2-10\text{keV}} + 0.39. \quad (36)$$

This conversion factor is the median difference between the intrinsic 2–10 keV and 14–195 keV luminosities of the BAT

sources within our main sample. A model-dependent approach would consider the distribution of X-ray spectral shapes and/or the measured 2–10 keV luminosities of BASS/DR2 AGNs (Ricci et al. 2017a; see also Ananna et al. 2020a). However, exploring a more complex conversion in this step is beyond the scope of this work, and would make a comparison to our main analysis, which uses a constant bolometric correction, rather ambiguous.

We next demonstrate the key results of our analysis using this luminosity-dependent bolometric correction. We present one set of results assuming  $\sigma_{\log L, \text{scatt}} = 0$ , for comparison with our main results, and additional results assuming a scatter in luminosity of 0.37 dex—which reflects the scatter in  $\kappa_{2-10\text{keV}}$  found by Duras et al. (2020; see their Table 1). As this systematic uncertainty in luminosity is rather high, we consider it as the total uncertainty in luminosity (i.e., the measurement uncertainty is assumed to be negligible). As noted in Appendix D above, this scatter in luminosity adds in quadrature to the uncertainty in BH masses, and translates into a higher total uncertainty on  $\lambda_{\text{E}}$  (due to the direct dependence on  $L_{\text{bol}}$ ):

$$\sigma_{\log \lambda_{\text{E}}} (= \sqrt{\sigma_{\log M_{\text{BH}}}^2 + \sigma_{\log L, \text{scatt}}^2}) = 0.48\text{--}0.62.$$

In Tables E1 and E2, we tabulate the results derived using the Duras et al. (2020) luminosity-dependent bolometric correction. In Figures E1 and E2, we plot the results, along with the  $\sigma_{\log M_{\text{BH}}} = \sigma_{\log \lambda_{\text{E}}} = 0.3$  results from the main analysis, for comparison. These figures show that the Duras et al. (2020) bolometric correction prescription produces significantly different ERDF shapes compared to those derived using a constant bolometric correction (shown using the orange solid line in these plots), especially at high- $\lambda_{\text{E}}$  values. However, we stress that our key conclusion concerning the difference in the characteristic break in the Eddington ratio ( $\lambda_{\text{E}}^*$ ) between Type 1 and Type 2 AGNs still holds for this bolometric correction prescription. Specifically, with the Duras et al. (2020) bolometric corrections, we obtain  $\log \lambda_{\text{E}}^* = -1.153^{+0.109}_{-0.066}$  and  $-1.68 \pm 0.11$  for Type 1 and Type 2 AGNs, respectively. The latter value is, again, remarkably consistent with what is expected from the radiation-driven unification scenario, as

**Table E1**  
Sample Truncation-corrected BHMFS<sup>a</sup> and Fits to  $1/V_{\text{max}}$  Values for the BHMFS for Type 1 AGNs, Type 2 AGNs, and Both Samples Together

	$\log(M_{\text{BH}}^*/M_{\odot})$	$\log(\Psi^*/h^3 \text{Mpc}^{-3})$	$\alpha$	$\beta$
<b>All</b>				
Intrinsic (Variable $\kappa_{\text{bol}}$ ; $\sigma = 0.3$ , $\sigma_{L, \text{scatt}} = 0$ )	$7.96^{+0.25}_{-0.21}$	−3.91	$-1.481^{+0.122}_{-0.079}$	$0.572^{+0.068}_{-0.075}$
Intrinsic (Variable $\kappa_{\text{bol}}$ ; $\sigma = 0.3$ , $\sigma_{L, \text{scatt}} = 0.37$ )	$8.00^{+0.14}_{-0.27}$	−3.97	$-1.401^{+0.109}_{-0.085}$	$0.598^{+0.061}_{-0.075}$
Intrinsic (Variable $\kappa_{\text{bol}}$ ; $\sigma = 0.5$ , $\sigma_{L, \text{scatt}} = 0.37$ )	$7.98^{+0.15}_{-0.29}$	−3.96	$-1.32^{+0.14}_{-0.10}$	$0.597^{+0.095}_{-0.063}$
<b>Type 1</b>				
Intrinsic (Variable $\kappa_{\text{bol}}$ ; $\sigma = 0.3$ , $\sigma_{L, \text{scatt}} = 0$ )	$8.25^{+0.21}_{-0.28}$	−4.7	$-1.693^{+0.115}_{-0.073}$	$0.592^{+0.056}_{-0.107}$
Intrinsic (Variable $\kappa_{\text{bol}}$ ; $\sigma = 0.3$ , $\sigma_{L, \text{scatt}} = 0.37$ )	$8.13^{+0.22}_{-0.23}$	−4.57	$-1.589^{+0.077}_{-0.113}$	$0.564^{+0.076}_{-0.070}$
Intrinsic (Variable $\kappa_{\text{bol}}$ ; $\sigma = 0.5$ , $\sigma_{L, \text{scatt}} = 0.37$ )	$8.22^{+0.20}_{-0.30}$	−4.77	$-1.61^{+0.10}_{-0.12}$	$0.575^{+0.090}_{-0.081}$
$1/V_{\text{max}}$	$8.73^{+0.26}_{-0.31}$	$-5.10^{+0.26}_{-0.50}$	$-1.35^{+0.18}_{-0.23}$	$0.681^{+0.087}_{-0.114}$
<b>Type 2</b>				
Intrinsic (Variable $\kappa_{\text{bol}}$ ; $\sigma = 0.3$ , $\sigma_{L, \text{scatt}} = 0$ )	$7.89^{+0.15}_{-0.28}$	−3.95	$-1.13^{+0.16}_{-0.17}$	$0.630^{+0.082}_{-0.071}$
Intrinsic (Variable $\kappa_{\text{bol}}$ ; $\sigma = 0.3$ , $\sigma_{L, \text{scatt}} = 0.37$ )	$7.85^{+0.17}_{-0.22}$	−4.07	$-1.11^{+0.16}_{-0.13}$	$0.650^{+0.066}_{-0.082}$
Intrinsic (Variable $\kappa_{\text{bol}}$ ; $\sigma = 0.5$ , $\sigma_{L, \text{scatt}} = 0.37$ )	$7.81^{+0.18}_{-0.20}$	−4.05	$-0.99^{+0.25}_{-0.15}$	$0.708^{+0.054}_{-0.096}$
$1/V_{\text{max}}$	$8.102^{+0.172}_{-0.095}$	$-4.33^{+0.19}_{-0.23}$	$-1.04^{+0.30}_{-0.29}$	$0.732^{+0.074}_{-0.050}$

**Notes.** All results were calculated assuming the Duras et al. (2020) bolometric correction.

<sup>a</sup> We assume a modified Schechter function (see Equation (10)) for the BHMFS.

**Table E2**  
Sample Truncation-corrected ERDFs<sup>a</sup> and Fits to  $1/V_{\max}$  Values for the ERDFs for Type 1 AGNs, Type 2 AGNs, and the Full AGN Sample

	$\log \lambda_E^*$	$\log(\zeta^*/h^3 \text{ Mpc}^{-3})$	$\delta_1$	$\epsilon_\lambda$
<b>All</b>				
Intrinsic (Variable $\kappa_{\text{bol}}; \sigma = 0.3, \sigma_{\text{Lscatt}} = 0$ )	$-1.346_{-0.086}^{+0.098}$	-3.55	$0.20_{-0.12}^{+0.11}$	$1.908_{-0.074}^{+0.086}$
Intrinsic (Variable $\kappa_{\text{bol}}; \sigma = 0.3, \sigma_{\text{Lscatt}} = 0.37$ )	$-1.35_{-0.10}^{+0.11}$	-3.64	$0.18_{-0.10}^{+0.17}$	$1.908_{-0.096}^{+0.093}$
Intrinsic (Variable $\kappa_{\text{bol}}; \sigma = 0.5, \sigma_{\text{Lscatt}} = 0.37$ )	$-1.380_{-0.097}^{+0.104}$	-3.65	$0.11_{-0.18}^{+0.15}$	$2.05_{-0.14}^{+0.11}$
$1/V_{\max}$	$-1.19_{-0.21}^{+0.23}$	$-3.76_{-0.30}^{+0.18}$	$-0.02_{-0.39}^{+0.29}$	$2.06_{-0.27}^{+0.30}$
<b>Type 1</b>				
Intrinsic (Variable $\kappa_{\text{bol}}; \sigma = 0.3, \sigma_{\text{Lscatt}} = 0$ )	$-1.153_{-0.066}^{+0.109}$	-3.94	$0.04_{-0.13}^{+0.15}$	$2.20_{-0.12}^{+0.10}$
Intrinsic (Variable $\kappa_{\text{bol}}; \sigma = 0.3, \sigma_{\text{Lscatt}} = 0.37$ )	$-1.145_{-0.109}^{+0.067}$	-4.03	$0.02_{-0.16}^{+0.15}$	$2.19_{-0.12}^{+0.14}$
Intrinsic (Variable $\kappa_{\text{bol}}; \sigma = 0.5, \sigma_{\text{Lscatt}} = 0.37$ )	$-1.13 \pm 0.11$	-4.03	$-0.10_{-0.15}^{+0.23}$	$2.43_{-0.17}^{+0.18}$
$1/V_{\max}$	$-1.06_{-0.25}^{+0.28}$	$-4.02_{-0.32}^{+0.22}$	$-0.51_{-0.41}^{+0.53}$	$2.57_{-0.45}^{+0.33}$
<b>Type 2</b>				
Intrinsic (Variable $\kappa_{\text{bol}}; \sigma = 0.3, \sigma_{\text{Lscatt}} = 0$ )	$-1.68 \pm 0.11$	-3.98	$0.14_{-0.17}^{+0.21}$	$2.16_{-0.17}^{+0.16}$
Intrinsic (Variable $\kappa_{\text{bol}}; \sigma = 0.3, \sigma_{\text{Lscatt}} = 0.37$ )	$-1.73 \pm 0.12$	-3.87	$0.25_{-0.23}^{+0.20}$	$2.03_{-0.16}^{+0.18}$
Intrinsic (Variable $\kappa_{\text{bol}}; \sigma = 0.5, \sigma_{\text{Lscatt}} = 0.37$ )	$-1.72_{-0.15}^{+0.12}$	-3.91	$0.19 \pm 0.24$	$1.99_{-0.11}^{+0.24}$
$1/V_{\max}$	$-1.87_{-0.40}^{+0.38}$	$-3.74_{-0.43}^{+0.35}$	$-0.50_{-0.56}^{+1.08}$	$2.30_{-0.69}^{+0.81}$

**Notes.** All results were calculated assuming the Duras et al. (2020) bolometric correction.

<sup>a</sup> We assume a double-power-law shape for the ERDF (see Equation (11)).

discussed in Section 5.1 (see Fabian et al. 2009; Ricci et al. 2017b). On the other hand, when experimenting with luminosity-dependent bolometric corrections, we note that varying  $\sigma_{\log M_{\text{BH}}}$  and  $\sigma_{\log L_{\text{scatt}}}$  does not significantly change the results.

Given the wide range of bolometric corrections investigated in the literature, and the complexity of applying such

prescriptions when deriving the *intrinsic* distributions of key AGN properties, we prefer not to recommend one set of bolometric corrections in this work. Instead, we present the constant bolometric correction results in the main part of the text, due to its simplicity, and leave it to the discretion of the reader to choose to use either those results, or those based on the Duras et al. (2020) prescription, presented in this Appendix.

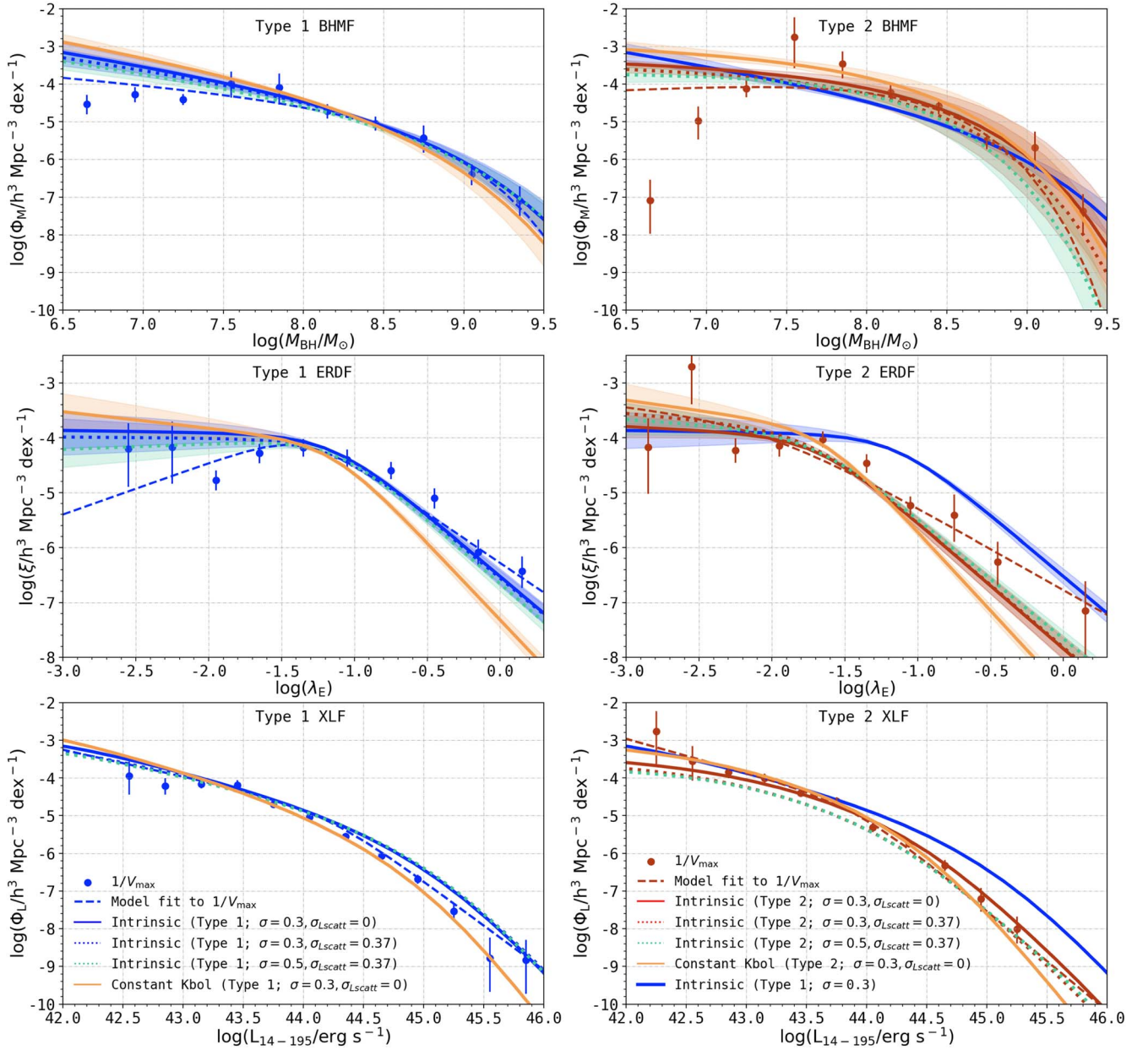


**Figure E1.** The BHMf, ERDFs, and reconstructed XLFs of the BASS/DR2 AGNs, derived using a luminosity-dependent bolometric correction. The distributions of BH mass, Eddington ratio, and luminosity are shown in the top, middle, and bottom panels, respectively, for both the Type 1 and Type 2 AGNs in BASS/DR2 (the left and right panels). These are calculated using the luminosity-dependent bolometric corrections of Duras et al. (2020). For each type of AGN, combining the BHMf (top row) and the ERDF (middle row) reproduces the observed XLF (bottom row). The data points come from the  $1/V_{\max}$  analysis, and the dashed lines represent the fits to these data points. The solid lines and shaded areas show the final, bias-corrected intrinsic distribution functions, derived assuming uncertainties of  $\sigma_{\log M_{\text{BH}}} = \sigma_{\lambda_E} = 0.3$  and  $\sigma_{\log M_{\text{BH}}} = 0.3$ ,  $\sigma_{\log L_{\text{scatt}}} = 0.37$  (i.e.,  $\sigma_{\log \lambda_E} = 0.47$  dex) for Type 1 AGNs, respectively (and the red solid and dotted lines for Type 2 AGNs, respectively). The green dotted lines in the left (right) panels are calculated assuming  $\sigma_{\log M_{\text{BH}}} = 0.5$ ,  $\sigma_{\log L_{\text{scatt}}} = 0.37$  (i.e.,  $\sigma_{\log \lambda_E} = 0.62$  dex) for Type 1 (Type 2) AGNs. The best-fit distributions of Type 1 AGNs (for the  $\sigma_{\log M_{\text{BH}}} = \sigma_{\log \lambda_E} = 0.3$  case) are shown also in the right panels, to highlight the differences between Type 1 and Type 2 AGNs. Both panels are also overplotted with constant bolometric correction results (the orange solid line) from the main part of the text (the  $\sigma_{\log M_{\text{BH}}} = \sigma_{\log \lambda_E} = 0.3$  case) for comparison. The  $1/V_{\max}$  values (split by AGN type) are reported in Tables F2–F4.

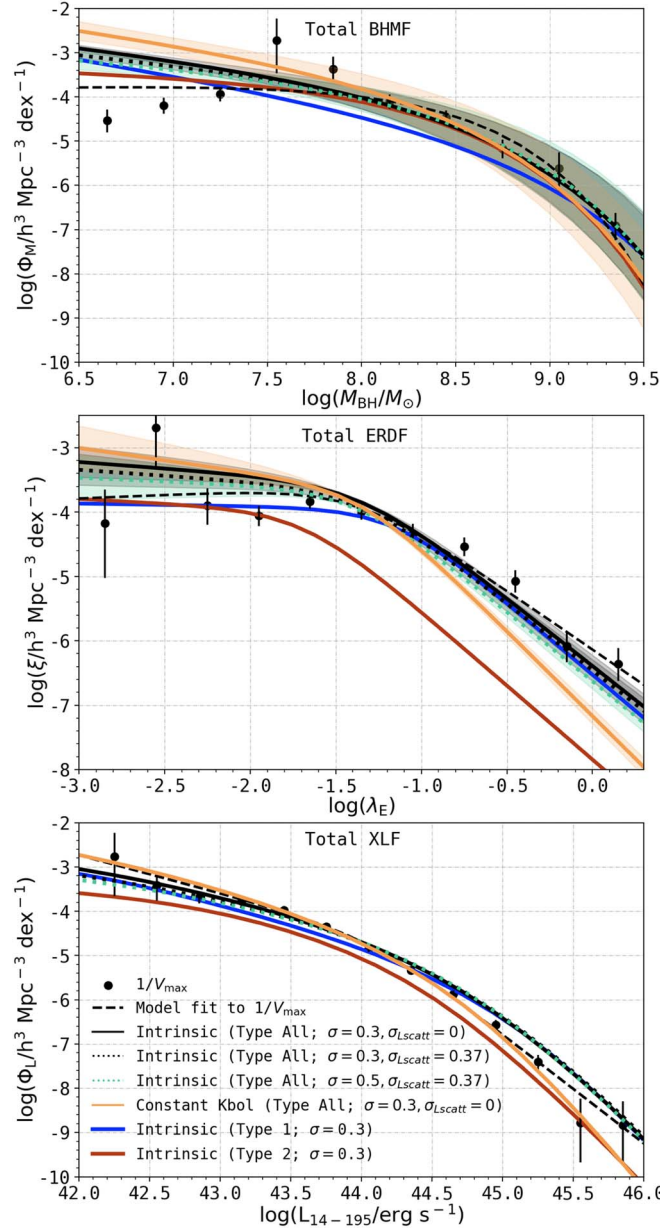


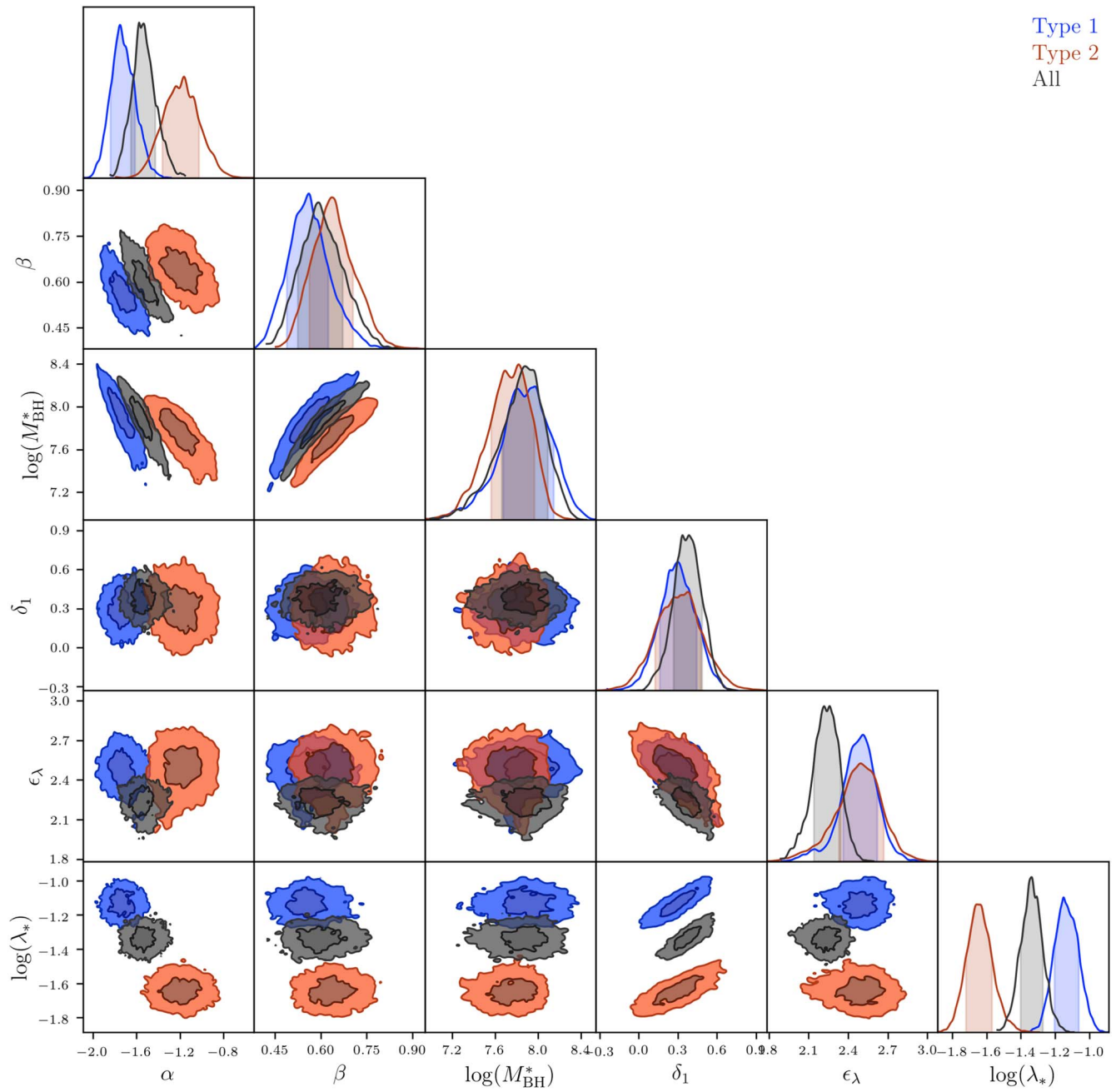
**Figure E2.** As in Figure E1, the BHMf, ERDF, and reconstructed XLFs are shown in the top, middle, and bottom panels, respectively, for both the Type 1 and Type 2 AGNs in BASS/DR2 (the left and right panels). These functions are calculated assuming a luminosity-dependent bolometric correction (Duras et al. 2020). We show the intrinsic distributions derived for all AGNs, assuming uncertainties of either  $\sigma_{\log M_{\text{BH}}} = 0.3$  and  $\sigma_{\log \lambda_E} = 0.47$  dex or  $\sigma_{\log M_{\text{BH}}} = 0.5$  and  $\sigma_{\log \lambda_E} = 0.62$  dex, in the black and green lines, respectively. The black data points in the bottom panel show the direct  $1/V_{\text{max}}$  XLF estimates, and the black dashed line is the fit to those points. The solid black lines show the final, bias-corrected intrinsic distribution functions for the complete AGN sample.

## Appendix F Figures and Tables of Key Results

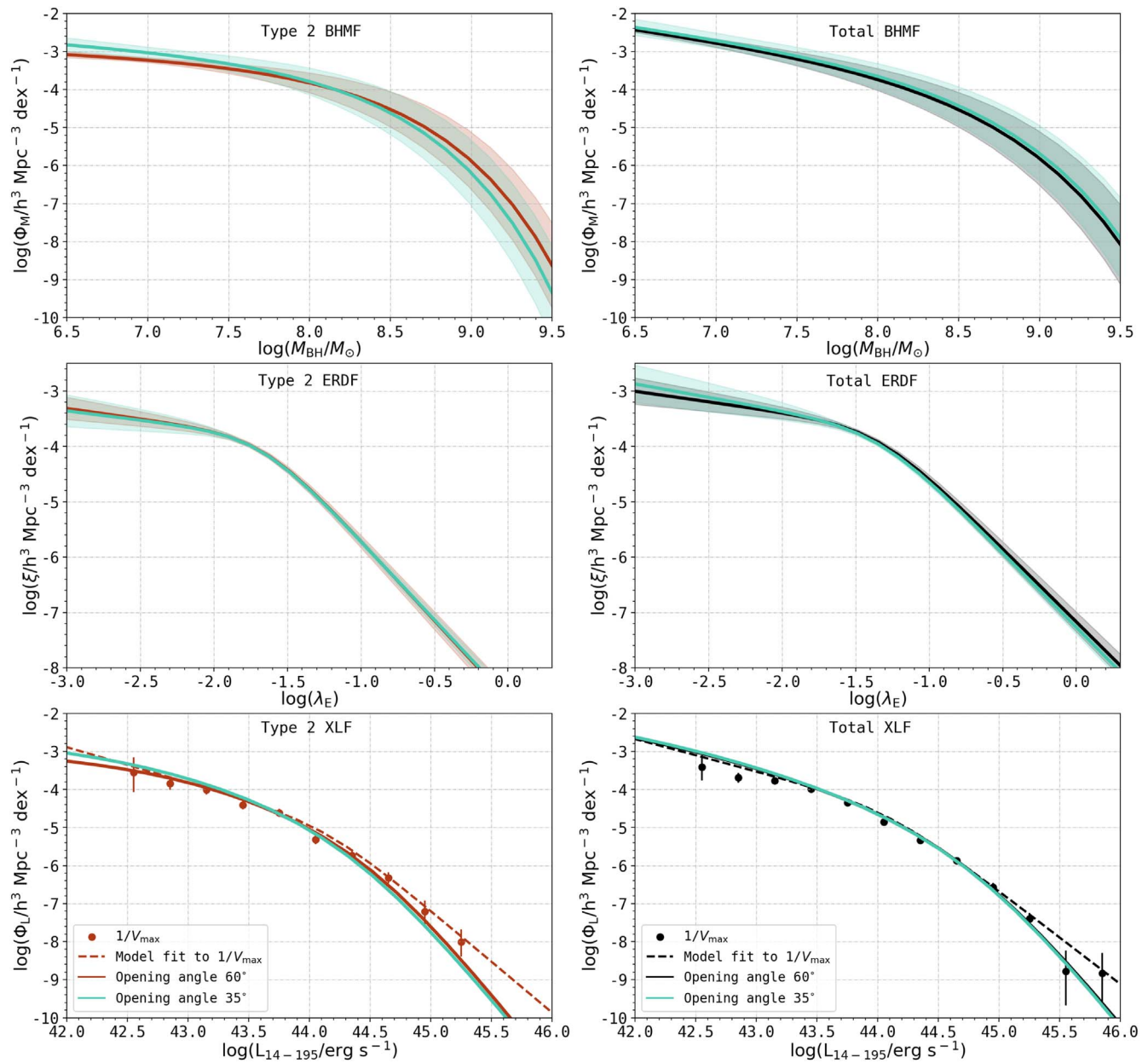
We present the MCMC probability chains of the six parameters defining BHMf and ERDF for Type 1, Type 2 and all AGNs in Figure F1. The BHMf, ERDF, and XLF for Type 2 and all AGNs are shown in Figure F2 for two opening angles of the obscuring torus:  $60^\circ$  and  $35^\circ$ . In Figure F3, we show the effect of including the lowest luminosity object on the  $1/V_{\text{max}}$  values for the for Type 2 AGNs. While the effect on  $1/V_{\text{max}}$  values is dramatic, our bias correction method is not significantly effected by this object, as shown by red (includes outlier) and green (excludes outlier) solid lines.

Table F1 reports the intrinsic ERDFs of the low- and high-mass bins for both Type 1 and Type 2 AGNs, shown in Figure 12. Tables F2–F4 report the  $1/V_{\text{max}}$  values of the XLFs, BHMf, and ERDFs, respectively, for Type 1, Type 2, and all AGNs. These functions are shown in Figures 8 and 9. Table F5 reports the  $1/V_{\text{max}}$  datapoints for the XLF of all AGNs within the redshift ranges  $z \leq 0.3$  and  $0.01 \leq z \leq 0.3$ ; for the latter range, space densities are provided with and without obscuration correction. These data points are shown in Figure 6. Table F6 provides the  $1/V_{\text{max}}$  values for the BAT sample in three  $\log N_{\text{H}}$  bins:  $\log N_{\text{H}} < 22$ ,  $22 \leq \log N_{\text{H}} \leq 24$ , and  $\log N_{\text{H}} \geq 24$ , and these results are shown in Figure 7.

Type 1  
Type 2  
All



**Figure F1.** The three probability chains (Type 1 in blue, Type 2 in red, and overall in black) plotted together.



**Figure F2.** Number densities of BASS Type 2 AGNs (left panels; red points/lines) and all AGNs (right panels; black points/lines), assuming an absorption function and attenuation curve for a template spectra with torus opening angle of  $60^\circ$ . The overplotted green lines show the results for a template spectra with torus opening angle of  $35^\circ$ .



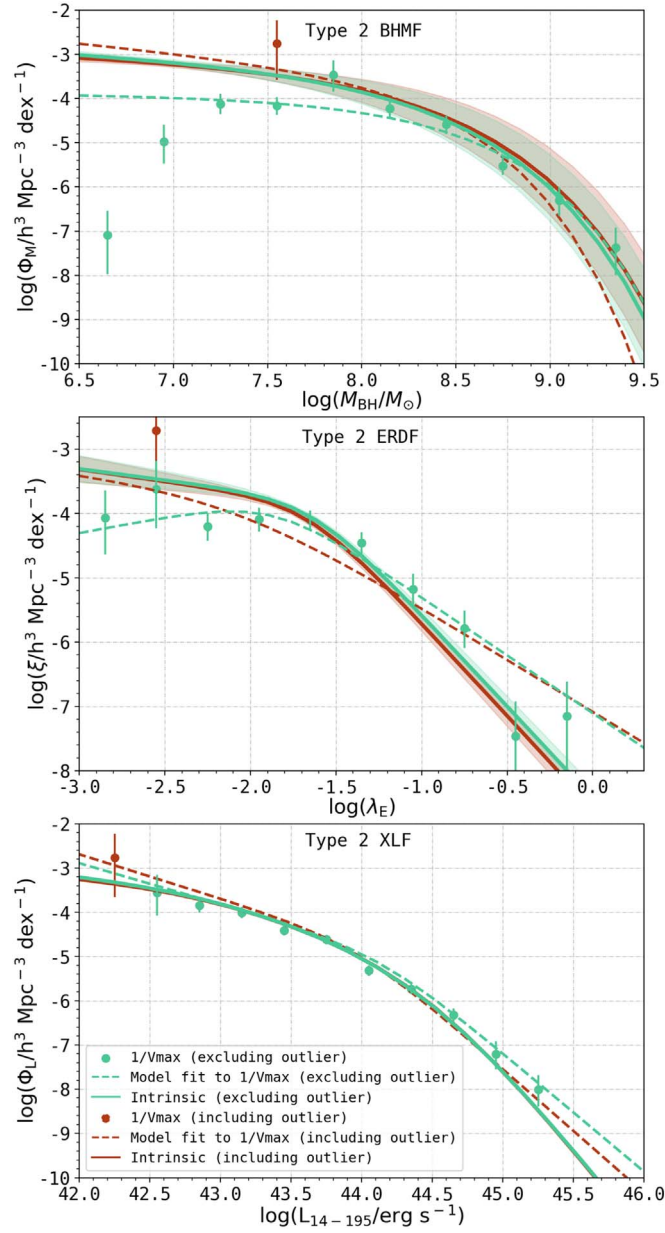


**Figure F3.** The impact on our analysis due to the lowest-luminosity and lowest-redshift object within our redshift-restricted sample (NGC 5283, or BAT ID 684). The green points show the  $1/V_{\max}$  measurements excluding this single source, as is the case throughout our main analysis, while the red point shows how these change when the source is included in the sample (affecting only one bin in luminosity,  $M_{\text{BH}}$ , and  $\lambda_E$ ). This object falls at the flux threshold of the overall survey (according to the curve shown in Figure 4), but given the variation in the sky sensitivity (i.e., flux–area relation) across the surveyed area, the corresponding  $1/V_{\max}$  value is likely to be inaccurate. The different lines demonstrate that—unlike some of the fits to  $1/V_{\max}$  measurements—the *intrinsic* distribution functions are robust to the choice of including or excluding this single source; for all three distribution functions, the solid lines of the two cases (almost) completely overlap, while the dashed lines do not. We provide all  $1/V_{\max}$  measurements, both with and without this single source, in Tables F2–F4.

**Table F1**  
Sample Truncation-corrected ERDFs for Type 1 AGNs and Type 2 AGNs in Low-mass ( $\log M_{\text{BH}} \leq 7.8$ ) and High-mass ( $\log M_{\text{BH}} \geq 8.2$ ) Bins

	$\log \lambda_E^*$	$\log(\xi^*/h^3 \text{Mpc}^{-3})$	$\delta_1$	$\epsilon_\lambda$
Type 1				
Low Mass	$-0.898^{+0.100}_{-0.094}$	-4.15	$0.36^{+0.19}_{-0.15}$	$2.67^{+0.17}_{-0.23}$
High Mass	$-1.313^{+0.101}_{-0.087}$	-5.29	$0.32^{+0.19}_{-0.14}$	$2.46^{+0.22}_{-0.21}$
Type 2				
Low Mass	$-1.59^{+0.15}_{-0.19}$	-3.82	$0.64^{+0.26}_{-0.28}$	$2.05^{+0.16}_{-0.26}$
High Mass	$-1.69^{+0.11}_{-0.13}$	-5.18	$0.37^{+0.17}_{-0.26}$	$2.43^{+0.18}_{-0.20}$

**Table F2**  
 $1/V_{\max}$  Values of the XLFs for all AGNs Selected by the Cuts Described in Table 1

All					Type 1				Type 2			
$\log(L_X/\text{erg s}^{-1})$	$N$	$\log(\Phi_L)$	$\sigma_{\text{up}}$	$\sigma_{\text{low}}$	$N$	$\log(\Phi_L)$	$\sigma_{\text{up}}$	$\sigma_{\text{low}}$	$N$	$\log(\Phi_L)$	$\sigma_{\text{up}}$	$\sigma_{\text{low}}$
42.25	1	-2.77	0.52	-0.87					1	-2.77	0.52	-0.87
42.55	5	-3.41	0.29	-0.34	2	-3.95	0.37	-0.47	3	-3.55	0.38	-0.5
42.85	22	-3.69	0.11	-0.11	8	-4.22	0.19	-0.2	14	-3.85	0.14	-0.14
43.15	59	-3.78	0.07	-0.07	28	-4.16	0.1	-0.1	31	-4.01	0.1	-0.1
43.45	89	-3.99	0.08	-0.08	53	-4.2	0.12	-0.12	36	-4.41	0.09	-0.09
43.75	111	-4.35	0.05	-0.05	62	-4.7	0.06	-0.06	49	-4.61	0.08	-0.08
44.05	104	-4.86	0.05	-0.05	75	-5.04	0.06	-0.06	29	-5.32	0.09	-0.09
44.35	86	-5.34	0.05	-0.05	56	-5.56	0.06	-0.06	30	-5.74	0.09	-0.09
44.65	63	-5.87	0.07	-0.07	45	-6.07	0.08	-0.08	18	-6.32	0.13	-0.13
44.95	32	-6.57	0.1	-0.1	26	-6.69	0.1	-0.1	6	-7.21	0.27	-0.31
45.25	12	-7.41	0.14	-0.15	9	-7.53	0.17	-0.18	3	-8.01	0.31	-0.36
45.55	1	-8.78	0.52	-0.87	1	-8.78	0.52	-0.87				
45.85	1	-8.84	0.52	-0.87	1	-8.84	0.52	-0.87				
586					366				220			

**Note.** Here, we also present the  $1/V_{\max}$  values for the Type 1 and Type 2 samples separately, which together constitute the overall sample. Note that to plot these data points, the bin size  $d \log L_X = 0.3$  dex has to be subtracted from the  $\log \Phi_L$  values.

**Table F3**  
 $1/V_{\max}$  Values for the BHMFs of all Table 1–selected AGNs, Type 1 AGNs, and Type 2 AGNs (Uncorrected for Sample Truncation)

All					Type 1				Type 2			
$\log(M_{\text{BH}}/M_{\odot})$	$N$	$\log(\Psi)$	$\sigma_{\text{up}}$	$\sigma_{\text{low}}$	$N$	$\log(\Psi)$	$\sigma_{\text{up}}$	$\sigma_{\text{low}}$	$N$	$\log(\Psi)$	$\sigma_{\text{up}}$	$\sigma_{\text{low}}$
6.65	16	-4.53	0.22	-0.25	15	-4.53	0.22	-0.25	1	-7.08	0.52	-0.87
6.95	27	-4.2	0.16	-0.17	23	-4.28	0.18	-0.19	4	-4.98	0.37	-0.47
7.25	56	-3.94	0.13	-0.14	42	-4.41	0.12	-0.13	14	-4.12	0.2	-0.22
7.55	76 (75)	-2.73 (-3.76)	0.47 (0.19)	-0.72 (-0.2)	48	-3.99	0.3	-0.35	28 (27)	-2.75 (-4.16)	0.5 (0.17)	-0.8 (-0.18)
7.85	112	-3.37	0.25	-0.29	65	-4.09	0.35	-0.43	47	-3.46	0.31	-0.36
8.15	116	-4.1	0.14	-0.14	68	-4.72	0.17	-0.17	48	-4.22	0.18	-0.19
8.45	99	-4.46	0.14	-0.14	56	-5.05	0.16	-0.17	43	-4.59	0.18	-0.19
8.75	52	-5.17	0.18	-0.19	28	-5.43	0.31	-0.37	24	-5.52	0.17	-0.18
9.05	23	-6.05	0.18	-0.2	15	-6.4	0.24	-0.27	8	-6.31	0.28	-0.33
9.35	8	-6.91	0.27	-0.31	5	-7.1	0.36	-0.45	3	-7.37	0.43	-0.6
586					366				220			

**Note.** The quantities in brackets show the  $1/V_{\max}$  values after excluding one object that lies at the low-flux threshold of the attenuation curve (discussed in Section 3.2).

**Table F4**  
 $1/V_{\max}$  Values for the ERDFs of all Table 1–selected AGNs, Type 1 AGNs, and Type 2 AGNs (Uncorrected for Sample Truncation)

All					Type 1				Type 2			
$\log \lambda_E$	$N$	$\log(\xi)$	$\sigma_{\text{up}}$	$\sigma_{\text{low}}$	$N$	$\log(\xi)$	$\sigma_{\text{up}}$	$\sigma_{\text{low}}$	$N$	$\log(\xi)$	$\sigma_{\text{up}}$	$\sigma_{\text{low}}$
-2.85	3	-4.07	0.41	-0.55					3	-4.07	0.41	-0.55
-2.55	13 (12)	-2.7 (-3.52)	0.45 (0.35)	-0.64 (-0.43)	4	-4.19	0.45	-0.64	9 (8)	-2.71 (-3.62)	0.46 (0.43)	-0.68 (-0.59)
-2.25	29	-3.89	0.25	-0.28	9	-4.18	0.46	-0.67	20	-4.2	0.19	-0.2
-1.95	71	-4.0	0.13	-0.14	26	-4.74	0.15	-0.16	45	-4.09	0.16	-0.17
-1.65	118	-3.89	0.1	-0.1	57	-4.29	0.16	-0.17	61	-4.11	0.13	-0.14
-1.35	133	-3.97	0.1	-0.1	89	-4.14	0.13	-0.14	44	-4.46	0.15	-0.16
-1.05	105	-4.32	0.14	-0.15	79	-4.39	0.16	-0.17	26	-5.18	0.22	-0.24
-0.75	62	-4.74	0.11	-0.11	53	-4.78	0.12	-0.12	9	-5.78	0.26	-0.29
-0.45	34	-5.1	0.16	-0.17	33	-5.1	0.17	-0.17	1	-7.46	0.52	-0.87
-0.15	11	-6.23	0.23	-0.25	10	-6.29	0.25	-0.28	1	-7.15	0.52	-0.87
0.15	6	-6.53	0.28	-0.32	6	-6.53	0.28	-0.32				
0.45	1	-7.08	0.52	-0.87					1	-7.08	0.52	-0.87
586					366				220			

**Note.** The quantities in brackets show the  $1/V_{\max}$  values after excluding one object that lies at the low-flux threshold of the attenuation curve (discussed in Section 3.2).

**Table F5**  
 $1/V_{\max}$  Values for the XLFs Shown in Figure 6

All BASS AGN				No Obs Corr					With Obs Corr			
$\log(L_X/\text{erg s}^{-1})$	$N$	$\log(\Phi_L/h^3 \text{ Mpc}^{-3})$	$\sigma_{\text{up}}$	$\sigma_{\text{low}}$	$N$	$\log(\Phi_L/h^3 \text{ Mpc}^{-3})$	$\sigma_{\text{up}}$	$\sigma_{\text{low}}$	$N$	$\log(\Phi_L/h^3 \text{ Mpc}^{-3})$	$\sigma_{\text{up}}$	$\sigma_{\text{low}}$
40.75	1	-2.21	0.52	-0.87	0				0			
41.05	1	-2.62	0.52	-0.87	0				0			
41.35	1	-3.16	0.52	-0.87	0				0			
41.65	3	-2.82	0.3	-0.36	0				0			
41.95	8	-2.94	0.18	-0.19	0				0			
42.25	9	-3.43	0.17	-0.19	1	-3.12	0.52	-0.87	1	-2.77	0.52	-0.87
42.55	16	-3.52	0.12	-0.13	6	-3.56	0.22	-0.24	6	-3.37	0.27	-0.3
42.85	33	-3.68	0.09	-0.09	28	-3.67	0.1	-0.1	28	-3.6	0.1	-0.1
43.15	68	-3.84	0.06	-0.06	61	-3.85	0.06	-0.06	61	-3.77	0.07	-0.07
43.45	95	-4.09	0.05	-0.05	90	-4.11	0.05	-0.05	90	-3.98	0.08	-0.08
43.75	115	-4.43	0.04	-0.04	113	-4.43	0.04	-0.04	113	-4.34	0.05	-0.05
44.05	106	-4.9	0.05	-0.05	106	-4.89	0.05	-0.05	106	-4.85	0.05	-0.05
44.35	90	-5.35	0.05	-0.05	89	-5.36	0.05	-0.05	89	-5.33	0.05	-0.05
44.65	70	-5.9	0.06	-0.06	70	-5.9	0.06	-0.06	70	-5.84	0.06	-0.06
44.95	39	-6.53	0.08	-0.08	39	-6.53	0.08	-0.08	39	-6.47	0.08	-0.09
45.25	13	-7.39	0.14	-0.14	13	-7.39	0.14	-0.14	13	-7.37	0.14	-0.14
45.55	2	-8.5	0.37	-0.47	2	-8.5	0.37	-0.47	2	-8.49	0.37	-0.47
45.85	1	-8.84	0.52	-0.87	1	-8.84	0.52	-0.87	1	-8.84	0.52	-0.87
671 <sup>a</sup>				619					619			

**Notes.** The ‘‘All BASS AGN’’ sample falls within the  $z \leq 0.3$  range, and the other two samples fall within the  $0.01 \leq z \leq 0.3$  range.











<sup>a</sup> The lowest-luminosity object has a luminosity of  $\log L_{14-195} = 38.56$ , and a  $V_{\max}$  very close to zero (i.e.,  $1/V_{\max} = -\infty$ ). Including that object will bring the total to 672.











**Table F6**  
 $1/V_{\max}$  Values of the XLFs in Different Obscuration Bins, as Shown in Figure 7

$\log N_{\text{H}} \leq 22$				$22 \leq \log N_{\text{H}} \leq 24$					$\log N_{\text{H}} \geq 24$			
$\log(L_X/\text{erg s}^{-1})$	$N$	$\log(\Phi_L/h^3 \text{ Mpc}^{-3})$	$\sigma_{\text{up}}$	$\sigma_{\text{low}}$	$N$	$\log(\Phi_L/h^3 \text{ Mpc}^{-3})$	$\sigma_{\text{up}}$	$\sigma_{\text{low}}$	$N$	$\log(\Phi_L/h^3 \text{ Mpc}^{-3})$	$\sigma_{\text{up}}$	$\sigma_{\text{low}}$
42.25					1	-2.77	0.52	-0.87				
42.55	1	-4.45	0.52	-0.87	5	-3.41	0.29	-0.34				
42.85	12	-4.06	0.15	-0.15	14	-3.87	0.14	-0.15	2	-4.57	0.37	-0.47
43.15	24	-4.25	0.1	-0.1	34	-4.04	0.09	-0.09	3	-4.63	0.31	-0.38
43.45	39	-4.46	0.08	-0.08	42	-4.41	0.08	-0.08	9	-4.52	0.25	-0.28
43.75	48	-4.83	0.07	-0.07	54	-4.68	0.07	-0.07	11	-5.02	0.16	-0.17
44.05	67	-5.1	0.06	-0.06	32	-5.33	0.09	-0.09	7	-5.77	0.19	-0.21
44.35	44	-5.66	0.07	-0.07	44	-5.62	0.07	-0.07	1	-7.05	0.52	-0.87
44.65	42	-6.14	0.07	-0.08	25	-6.26	0.1	-0.1	3	-6.74	0.31	-0.37
44.95	28	-6.69	0.09	-0.09	8	-7.16	0.18	-0.19	3	-7.19	0.31	-0.37
45.25	9	-7.53	0.17	-0.18	3	-8.02	0.3	-0.36	1	-8.38	0.52	-0.87
45.55	1	-8.78	0.52	-0.87	1	-8.81	0.52	-0.87				
45.85	1	-8.84	0.52	-0.87								
316				263					40			

**Note.** All samples fall within the  $0.01 \leq z \leq 0.3$  range.

### ORCID iDs

Tonima Tasnim Ananna  <https://orcid.org/0000-0001-8211-3807>  
 Anna K. Weigel  <https://orcid.org/0000-0002-5489-4316>  
 Benny Trakhtenbrot  <https://orcid.org/0000-0002-3683-7297>  
 Michael J. Koss  <https://orcid.org/0000-0002-7998-9581>  
 C. Megan Urry  <https://orcid.org/0000-0002-0745-9792>  
 Claudio Ricci  <https://orcid.org/0000-0001-5231-2645>  
 Ryan C. Hickox  <https://orcid.org/0000-0003-1468-9526>  
 Ezequiel Treister  <https://orcid.org/0000-0001-7568-6412>  
 Franz E. Bauer  <https://orcid.org/0000-0002-8686-8737>  
 Yoshihiro Ueda  <https://orcid.org/0000-0001-7821-6715>

Richard Mushotzky  <https://orcid.org/0000-0002-7962-5446>  
 Federica Ricci  <https://orcid.org/0000-0001-5742-5980>  
 Kyuseok Oh  <https://orcid.org/0000-0002-5037-951X>  
 Julian E. Mejía-Restrepo  <https://orcid.org/0000-0001-8450-7463>  
 Jakob Den Brok  <https://orcid.org/0000-0002-8760-6157>  
 Daniel Stern  <https://orcid.org/0000-0003-2686-9241>  
 Meredith C. Powell  <https://orcid.org/0000-0003-2284-8603>  
 Turgay Caglar  <https://orcid.org/0000-0002-9144-2255>  
 Kohei Ichikawa  <https://orcid.org/0000-0002-4377-903X>  
 O. Ivy Wong  <https://orcid.org/0000-0003-4264-3509>  
 Kevin Schawinski  <https://orcid.org/0000-0001-5464-0888>

## References

- Aird, J., Coil, A. L., & Georgakakis, A. 2018, *MNRAS*, 474, 1225
- Aird, J., Coil, A. L., Georgakakis, A., et al. 2015, *MNRAS*, 451, 1892
- Ajello, M., Alexander, D. M., Greiner, J., et al. 2012, *ApJ*, 749, 21
- Akylas, A., & Georgantopoulos, I. 2008, *A&A*, 479, 735
- Akylas, A., Georgantopoulos, I., Ranalli, P., et al. 2016, *A&A*, 594, A73
- Aller, M. C., & Richstone, D. 2002, *AJ*, 124, 3035
- Ananna, T. T., Treister, E., Urry, C. M., et al. 2020a, *ApJ*, 889, 17
- Ananna, T. T., Treister, E., Urry, C. M., et al. 2019, *ApJ*, 871, 240
- Ananna, T. T., Urry, C. M., Treister, E., et al. 2020b, *ApJ*, 903, 85
- Angles-Alcazar, D., Quataert, E., Hopkins, P., et al. 2021, *ApJ*, 917, 53
- Antonucci, R. 1993, *ARA&A*, 31, 473
- Arnaud, K. A. 1996, in ASP Conf. Ser., 101, *Astronomical Data Analysis Software and Systems V*, ed. G. H. Jacoby & J. Barnes (San Francisco, CA: ASP), 17
- Astropy Collaboration, Robitaille, T. P., Tollerud, E. J., et al. 2013, *A&A*, 558, A33
- Avni, Y., Soltan, A., Tananbaum, H., & Zamorani, G. 1980, *ApJ*, 238, 800
- Baldry, I. K., Driver, S. P., Loveday, J., et al. 2012, *MNRAS*, 421, 621
- Baloković, M., Brightman, M., Harrison, F. A., et al. 2018, *ApJ*, 854, 42
- Banerji, M., Alaghband-Zadeh, S., Hewett, P. C., & McMahon, R. G. 2015, *MNRAS*, 447, 3368
- Banerji, M., Jones, G. C., Carniani, S., DeGraf, C., & Wagg, J. 2021, *MNRAS*, 503, 5583
- Bär, R. E., Trakhtenbrot, B., Oh, K., et al. 2019, *MNRAS*, 489, 3073
- Barger, A. J., Cowie, L. L., Bautz, M. W., et al. 2001, *AJ*, 122, 2177
- Barger, A. J., Cowie, L. L., Mushotzky, R. F., et al. 2005, *AJ*, 129, 578
- Barthel, P. D. 1989, *ApJ*, 336, 606
- Baumgartner, W. H., Tueller, J., Markwardt, C. B., et al. 2013, *ApJS*, 207, 19
- Bell, E. F., Monachesi, A., Harmsen, B., et al. 2017, *ApJL*, 837, L8
- Bernardi, M., Hyde, J. B., Sheth, R. K., Miller, C. J., & Nichol, R. C. 2007, *AJ*, 133, 1741
- Blecha, L., Snyder, G. F., Satyapal, S., & Ellison, S. L. 2018, *MNRAS*, 478, 3056
- Brandt, W. N., & Alexander, D. M. 2015, *A&ARv*, 23, 1
- Brightman, M., Baloković, M., Ballantyne, D. R., et al. 2017, *ApJ*, 844, 10
- Brightman, M., & Nandra, K. 2011, *MNRAS*, 414, 3084
- Brusa, M., Civano, F., Comastri, A., et al. 2010, *ApJ*, 716, 348
- Buchner, J., Georgakakis, A., Nandra, K., et al. 2015, *ApJ*, 802, 89
- Burlon, D., Ajello, M., Greiner, J., et al. 2011, *ApJ*, 728, 58
- Caplar, N., Lilly, S. J., & Trakhtenbrot, B. 2015, *ApJ*, 811, 148
- Caplar, N., Lilly, S. J., & Trakhtenbrot, B. 2018, *ApJ*, 867, 148
- Carroll, C. M., Hickox, R. C., Masini, A., et al. 2021, *ApJ*, 908, 185
- Cavaliere, A., & Padovani, P. 1989, *ApJL*, 340, L5
- Choloniewski, J. 1987, *MNRAS*, 226, 273
- Croom, S. M., Richards, G. T., Shanks, T., et al. 2009, *MNRAS*, 399, 1755
- Cusumano, G., La Parola, V., Segreto, A., et al. 2010, *A&A*, 510, A48
- Davidzon, I., Ilbert, O., Laigle, C., et al. 2017, *A&A*, 605, A70
- De Rosa, G., Venemans, B. P., Decarli, R., et al. 2014, *ApJ*, 790, 145
- Duras, F., Bongiorno, A., Ricci, F., et al. 2020, *A&A*, 636, A73
- Eddington, A. S. 1913, *MNRAS*, 73, 359
- Efron, B., & Petrosian, V. 1992, *ApJ*, 399, 345
- Fabian, A. C., Celotti, A., & Erlund, M. C. 2006, *MNRAS*, 373, L16
- Fabian, A. C., Vasudevan, R. V., & Gandhi, P. 2008, *MNRAS*, 385, L43
- Fabian, A. C., Vasudevan, R. V., Mushotzky, R. F., Winter, L. M., & Reynolds, C. S. 2009, *MNRAS*, 394, L89
- Foreman-Mackey, D., Hogg, D. W., Lang, D., & Goodman, J. 2013, *PASP*, 125, 306
- Gavignaud, I., Wisotzki, L., Bongiorno, A., et al. 2008, *A&A*, 492, 637
- Gehrels, N. 1986, *ApJ*, 303, 336
- Georgakakis, A., Aird, J., Schulze, A., et al. 2017, *MNRAS*, 471, 1976
- Giallongo, E., Grazian, A., Fiore, F., et al. 2015, *A&A*, 578, A83
- Gilbank, D. G., Baldry, I. K., Balogh, M. L., Glazebrook, K., & Bower, R. G. 2010, *MNRAS*, 405, 2594
- Gilli, R., Comastri, A., & Hasinger, G. 2007, *A&A*, 463, 79
- Glikman, E., Lacy, M., LaMassa, S., et al. 2018, *ApJ*, 861, 37
- Glikman, E., Simmons, B., Maily, M., et al. 2015, *ApJ*, 806, 218
- Glikman, E., Urrutia, T., Lacy, M., et al. 2012, *ApJ*, 757, 51
- Goulding, A. D., Alexander, D. M., Lehmer, B. D., & Mullaney, J. R. 2010, *MNRAS*, 406, 597
- Graham, A. W., Onken, C. A., Athanassoula, E., & Combes, F. 2011, *MNRAS*, 412, 2211
- Greene, J. E., & Ho, L. C. 2005, *ApJ*, 630, 122
- Greene, J. E., & Ho, L. C. 2007, *ApJ*, 667, 131
- Greene, J. E., & Ho, L. C. 2009, *ApJ*, 704, 1743
- Gültekin, K., Richstone, D. O., Gebhardt, K., et al. 2009, *ApJ*, 698, 198
- Haiman, Z., & Hui, L. 2001, *ApJ*, 547, 27
- Häring, N., & Rix, H.-W. 2004, *ApJL*, 604, L89
- Harrison, F. A., Aird, J., Civano, F., et al. 2016, *ApJ*, 831, 185
- Hasinger, G., Miyaji, T., & Schmidt, M. 2005, *A&A*, 441, 417
- Herbel, J., Kacprzak, T., Amara, A., et al. 2017, *JCAP*, 2017, 035
- Hickox, R. C., & Alexander, D. M. 2018, *ARA&A*, 56, 625
- Hinton, S. R. 2016, *JOSS*, 1, 00045
- Hiroi, K., Ueda, Y., Akiyama, M., & Watson, M. G. 2012, *ApJ*, 758, 49
- Hogg, D. W. 1999, arXiv:astro-ph/9905116
- Hönig, S. F., & Beckert, T. 2007, *MNRAS*, 380, 1172
- Hopkins, P. F., Hernquist, L., Cox, T. J., et al. 2006a, *ApJS*, 163, 1
- Hopkins, P. F., Richards, G. T., & Hernquist, L. 2007, *ApJ*, 654, 731
- Hopkins, P. F., Somerville, R. S., Hernquist, L., et al. 2006b, *ApJ*, 652, 864
- Hunter, J. D. 2007, *CSE*, 9, 90
- Jin, C., Ward, M., & Done, C. 2012, *MNRAS*, 425, 907
- Jun, H. D., Assef, R. J., Carroll, C. M., et al. 2021, *ApJ*, 906, 21
- Kashikawa, N., Ishizaki, Y., Willott, C. J., et al. 2015, *ApJ*, 798, 28
- Kelly, B. C., Fan, X., & Vestergaard, M. 2008, *ApJ*, 682, 874
- Kelly, B. C., & Shen, Y. 2013, *ApJ*, 764, 45
- Kelly, B. C., Vestergaard, M., & Fan, X. 2009, *ApJ*, 692, 1388
- Kormendy, J., & Ho, L. C. 2013, *ARA&A*, 51, 511
- Koss, M., Mushotzky, R., Treister, E., et al. 2012, *ApJL*, 746, L22
- Koss, M. J., Assef, R., Baloković, M., et al. 2016a, *ApJ*, 825, 85
- Koss, M. J., Blecha, L., Bernhard, P., et al. 2018, *Natur*, 563, 214
- Koss, M. J., Glidden, A., Baloković, M., et al. 2016b, *ApJL*, 824, L4
- Koss, M. J., Ricci, C., Trakhtenbrot, B., et al. 2022b, *ApJS*, 261, 2
- Koss, M., Trakhtenbrot, B., Ricci, C., et al. 2017, *ApJ*, 850, 74
- Koss, M. J., Trakhtenbrot, B., Ricci, C., et al. 2022a, *ApJS*, 261, 1
- Koss, M. J., Trakhtenbrot, B., Ricci, C., et al. 2022c, *ApJS*, 261, 6
- Krivoson, R., Tsygankov, S., Revnivtsev, M., et al. 2010, *A&A*, 523, A61
- La Franca, F., Fiore, F., Comastri, A., et al. 2005, *ApJ*, 635, 864
- Lanzuisi, G., Civano, F., Marchesi, S., et al. 2013, *ApJ*, 778, 62
- Lawrence, A. 1991, *MNRAS*, 252, 586
- Lawrence, A., & Elvis, M. 1982, *ApJ*, 256, 410
- Lilly, S. J., Le Brun, V., Maier, C., et al. 2009, *ApJS*, 184, 218
- Lilly, S. J., Le Fevre, O., Hammer, F., & Crampton, D. 1996, *ApJL*, 460, L1
- Loredo, T. J. 2004, in AIP Conf. Proc., 735, *Bayesian Inference and Maximum Entropy Methods in Science and Engineering*, ed. R. Fischer, R. Preuss, & U. V. Toussaint (Melville, NY: AIP), 195
- Lusso, E., Comastri, A., Simmons, B. D., et al. 2012, *MNRAS*, 425, 623
- Lynden-Bell, D. 1971, *MNRAS*, 155, 95
- MacLeod, C. L., Ivezić, Ž., Kochanek, C. S., et al. 2010, *ApJ*, 721, 1014
- Madau, P., & Dickinson, M. 2014, *ARA&A*, 52, 415
- Madau, P., Pozzetti, L., & Dickinson, M. 1998, *ApJ*, 498, 106
- Maiolino, R., Shemmer, O., Imanishi, M., et al. 2007, *A&A*, 468, 979
- Marchesini, D., van Dokkum, P. G., Förster Schreiber, N. M., et al. 2009, *ApJ*, 701, 1765
- Marconi, A., & Hunt, L. K. 2003, *ApJL*, 589, L21
- Marconi, A., Risaliti, G., Gilli, R., et al. 2004, *MNRAS*, 351, 169
- Marleau, F. R., Clancy, D., & Bianconi, M. 2013, *MNRAS*, 435, 3085
- Martini, P., & Weinberg, D. H. 2001, *ApJ*, 547, 12
- Mateos, S., Carrera, F. J., Barcons, X., et al. 2017, *ApJL*, 841, L18
- Matsuoka, Y., Strauss, M. A., Kashikawa, N., et al. 2018, *ApJ*, 869, 150
- McConnell, N. J., & Ma, C.-P. 2013, *ApJ*, 764, 184
- McLure, R. J., & Dunlop, J. S. 2002, *MNRAS*, 331, 795
- McLure, R. J., & Dunlop, J. S. 2004, *MNRAS*, 352, 1390
- Mejía-Restrepo, J., Koss, M. J., Trakhtenbrot, B., et al. 2022, *ApJS*, 261, 5
- Merloni, A., Bongiorno, A., Brusa, M., et al. 2014, *MNRAS*, 437, 3550
- Miyaji, T., Hasinger, G., Salvato, M., et al. 2015, *ApJ*, 804, 104
- Moffett, A. J., Lange, R., Driver, S. P., et al. 2016, *MNRAS*, 462, 4336
- Netzer, H. 2019, *MNRAS*, 488, 5185
- Netzer, H., & Trakhtenbrot, B. 2007, *ApJ*, 654, 754
- Nobuta, K., Akiyama, M., Ueda, Y., et al. 2012, *ApJ*, 761, 143
- Novak, G. S., Ostriker, J. P., & Ciotti, L. 2011, *ApJ*, 737, 26
- Oh, K., Koss, M. J., Ueda, Y., et al. 2022, *ApJS*, 261, 4
- Onken, C. A., Ferrarese, L., Merritt, D., et al. 2004, *ApJ*, 615, 645
- Paiano, S., Falomo, R., Treves, A., & Scarpa, R. 2020, *MNRAS*, 497, 94
- Paliya, V. S., Koss, M., Trakhtenbrot, B., et al. 2019, *ApJ*, 881, 154
- Parsa, S., Dunlop, J. S., & McLure, R. J. 2018, *MNRAS*, 474, 2904
- Peng, Y.-J., Lilly, S. J., Kovač, K., et al. 2010, *ApJ*, 721, 193
- Peterson, B. M. 2014, *SSRv*, 183, 253
- Powell, M. C., Cappelluti, N., Urry, C. M., et al. 2018, *ApJ*, 858, 110
- Pozzetti, L., Bolzonella, M., Zucca, E., et al. 2010, *A&A*, 523, A13
- Price-Whelan, A. M., Sipőcz, B. M., Günther, H. M., et al. 2018, *AJ*, 156, 123
- Puccetti, S., Comastri, A., Bauer, F. E., et al. 2016, *A&A*, 585, A157

- Reines, A. E., & Volonteri, M. 2015, *ApJ*, **813**, 82
- Ricci, C., Bauer, F. E., Treister, E., et al. 2017c, *MNRAS*, **468**, 1273
- Ricci, C., Trakhtenbrot, B., Koss, M. J., et al. 2017a, *ApJS*, **233**, 17
- Ricci, C., Trakhtenbrot, B., Koss, M. J., et al. 2017b, *Natur*, **549**, 488
- Ricci, C., Ueda, Y., Koss, M. J., et al. 2015, *ApJL*, **815**, L13
- Ricci, F., Marchesi, S., Shankar, F., La Franca, F., & Civano, F. 2017d, *MNRAS*, **465**, 1915
- Sani, E., Marconi, A., Hunt, L. K., & Risaliti, G. 2011, *MNRAS*, **413**, 1479
- Sazonov, S., Revnivtsev, M., Krivonos, R., Churazov, E., & Sunyaev, R. 2007, *A&A*, **462**, 57
- Schmidt, M. 1968, *ApJ*, **151**, 393
- Schneider, D. P., Richards, G. T., Hall, P. B., et al. 2010, *AJ*, **139**, 2360
- Schulze, A., Bongiorno, A., Gavignaud, I., et al. 2015, *MNRAS*, **447**, 2085
- Schulze, A., & Wisotzki, L. 2010, *A&A*, **516**, A87
- Shankar, F., Allevato, V., Bernardi, M., et al. 2020, *NatAs*, **4**, 282
- Shankar, F., Bernardi, M., Richardson, K., et al. 2019, *MNRAS*, **485**, 1278
- Shankar, F., Croce, M., Miralda-Escudé, J., Fosalba, P., & Weinberg, D. H. 2010a, *ApJ*, **718**, 231
- Shankar, F., Sonnenfeld, A., Mamon, G. A., et al. 2017, *ApJ*, **840**, 34
- Shankar, F., Weinberg, D. H., & Miralda-Escudé, J. 2009, *ApJ*, **690**, 20
- Shankar, F., Weinberg, D. H., & Miralda-Escudé, J. 2013, *MNRAS*, **428**, 421
- Shankar, F., Weinberg, D. H., & Shen, Y. 2010b, *MNRAS*, **406**, 1959
- Shen, X., Hopkins, P. F., Faucher-Giguère, C.-A., et al. 2020, *MNRAS*, **495**, 3252
- Shen, Y. 2013, *BASI*, **41**, 61
- Shen, Y., Mulchaey, J. S., Raychaudhury, S., Rasmussen, J., & Ponman, T. J. 2007, *ApJL*, **654**, L115
- Shen, Y., Strauss, M. A., Ross, N. P., et al. 2009, *ApJ*, **697**, 1656
- Simpson, C. 2005, *MNRAS*, **360**, 565
- Soltan, A. 1982, *MNRAS*, **200**, 115
- Steffen, A. T., Barger, A. J., Cowie, L. L., Mushotzky, R. F., & Yang, Y. 2003, *ApJL*, **596**, L23
- Taylor, E. N., Hopkins, A. M., Baldry, I. K., et al. 2015, *MNRAS*, **446**, 2144
- Taylor, M. B. 2005, in ASP Conf. Ser., 347, *Astronomical Data Analysis Software and Systems XIV*, ed. P. Shopbell, M. Britton, & R. Ebert (San Francisco, CA: ASP), 29
- Trakhtenbrot, B., Netzer, H., Lira, P., & Shemmer, O. 2011, *ApJ*, **730**, 7
- Treister, E., Krolik, J. H., & Dullemond, C. 2008, *ApJ*, **679**, 140
- Treister, E., Schawinski, K., Urry, C. M., & Simmons, B. D. 2012, *ApJL*, **758**, L39
- Treister, E., & Urry, C. M. 2006, *ApJL*, **652**, L79
- Treister, E., Urry, C. M., Schawinski, K., Cardamone, C. N., & Sanders, D. B. 2010, *ApJL*, **722**, L238
- Tueller, J., Mushotzky, R. F., Barthelmy, S., et al. 2008, *ApJ*, **681**, 113
- Tundo, E., Bernardi, M., Hyde, J. B., Sheth, R. K., & Pizzella, A. 2007, *ApJ*, **663**, 53
- Ueda, Y., Akiyama, M., Hasinger, G., Miyaji, T., & Watson, M. G. 2014, *ApJ*, **786**, 104
- Ueda, Y., Akiyama, M., Ohta, K., & Miyaji, T. 2003, *ApJ*, **598**, 886
- Urry, C. M., & Padovani, P. 1995, *PASP*, **107**, 803
- van der Walt, S., Colbert, S. C., & Varoquaux, G. 2011, *CSE*, **13**, 22
- Vasudevan, R. V., & Fabian, A. C. 2007, *MNRAS*, **381**, 1235
- Vasudevan, R. V., & Fabian, A. C. 2009, *MNRAS*, **392**, 1124
- Vasudevan, R. V., Mushotzky, R. F., Winter, L. M., & Fabian, A. C. 2009, *MNRAS*, **399**, 1553
- Vestergaard, M., Fan, X., Tremonti, C. A., Osmer, P. S., & Richards, G. T. 2008, *ApJL*, **674**, L1
- Vestergaard, M., & Osmer, P. S. 2009, *ApJ*, **699**, 800
- Vito, F., Brandt, W. N., Stern, D., et al. 2018, *MNRAS*, **474**, 4528
- Wallis, K. F. 2014, arXiv:1405.4995
- Wang, M.-C. 1989, *J. Am. Stat. Assoc.*, **84**, 742
- Weigel, A. K., Schawinski, K., & Bruderer, C. 2016, *MNRAS*, **459**, 2150
- Weigel, A. K., Schawinski, K., Caplar, N., et al. 2017, *ApJ*, **845**, 134
- White, M., Martini, P., & Cohn, J. D. 2008, *MNRAS*, **390**, 1179
- Willott, C. J., Albert, L., Arzoumanian, D., et al. 2010b, *AJ*, **140**, 546
- Willott, C. J., Delorme, P., Reylé, C., et al. 2010a, *AJ*, **139**, 906
- Wilson, E. B. 1927, *J. Am. Stat. Assoc.*, **22**, 209
- Wisotzki, L., Christlieb, N., Bade, N., et al. 2000, *A&A*, **358**, 77
- Woo, J.-H., Schulze, A., Park, D., et al. 2013, *ApJ*, **772**, 49
- Woodroffe, M. 1985, *AnSta*, **13**, 163
- Yan, W., Hickox, R. C., Hainline, K. N., et al. 2019, *ApJ*, **870**, 33
- Zheng, X. Z., Bell, E. F., Somerville, R. S., et al. 2009, *ApJ*, **707**, 1566
- Zhu, G., Moustakas, J., & Blanton, M. R. 2009, *ApJ*, **701**, 86